INTERNATIONAL ATOMIC ENERGY AGENCY
UNITED NATIONS EDUCATIONAL, SCIENTIFIC AND CULTURAL ORGANIZATION
INTERNATIONAL CENTRE FOR THEORETICAL PHYSICS
I.C.T.P., P.O. BOX 586, 34100 TRIESTE, ITALY, CABLE: CENTRATOM TRIESTE

UNITED NATIONS INDUSTRIAL DEVELOPMENT ORGANIZATION

INTERNATIONAL CENTRE FOR SCIENCE AND HIGH TECHNOLOGY

c/o INTERNATIONAL CENTRE FOR THEORETICAL PHYSICS 34100 TRIESTE (ITALY) VIA GRIGNANO, 9 (ADRIATICO PALACE) P.O. BOX 586 TELEPHONE 040-224572 TELEFAX 040-224575 TELEX 460449 APH I

SECOND SCHOOL ON THE USE OF SYNCHROTRON RADIATION IN SCIENCE AND TECHNOLOGY: "JOHN FUGGLE MEMORIAL"

25 October - 19 November 1993

Miramare · Trieste, Italy

The Study of Surface Structures by Photoelectron Diffraction and Auger Electron Diffraction

Charles S. Fadley
Lawrence Berkeley Laboratory
Berkeley, USA

Charles S. Fadley

ABBREVIATIONS AND ACRONYMS

AED	Auger electron diffraction
APD	azimuthal photoelectron diffraction
ARPEFS	angle-resolved photoemission fine structure (acronym for scanned-energy photoelectron diffraction)
CMA	cylindrical mirror analyzer
DL	double-layer model
EELS	electron energy loss spectroscopy
ESDIAD	electron stimulated desorption ion angular distributions
EXAFS	extended X-ray absorption fine structure
FT	Fourier transform
FWHM	full width at half maximum intensity
GIXS	grazing incidence X-ray scattering
HT	high temperature limit (in SPPD experiment)
LEED	low energy electron diffraction
LT	lower temperature of measurement (in SPPD experiment)
ML	monolayer
MEIS	medium-energy ion scattering
MQNE	magnetic quantum number expansion
MS	multiple scattering
MSC	multiple scattering cluster
MTL	missing-top-layer model
NEXAFS	near edge X-ray absorption fine structure = XANES

Charles S. Fadley • Department of Chemistry, University of Hawaii, Honolulu, Hawaii 96822.
Present address: Department of Physics, University of California–Davis, Davis, California 95616, and
Materials Science Division, Lawrence Berkeley Laboratory, Berkeley, California 94720.

NPD	scanned-energy photoelectron diffraction with normal emission
ODAC	one-dimensional alkali-chain model
OPD	scanned-energy photoelectron diffraction with off-normal emission
PD, PhD	photoelectron diffraction
PLD	path-length difference
PPD	polar photoelectron diffraction
PW	plane-wave scattering
RBS	Rutherford back scattering
SEXAFS	surface extended X-ray absorption fine structure
SMSI	strong metal support interaction
SPAED	spin polarized Auger electron diffraction
SPPD	spin polarized photoelectron diffraction
SRMO	short-range magnetic order
SS	single scattering
SSC	single scattering cluster
STM	scanning tunneling microscopy
SW	spherical-wave scattering
XANES	X-ray absorption near-edge structure = NEXAFS
XPD	X-ray photoelectron diffraction, typically at energies of 500–1400 eV
XPS	X-ray photoelectron spectroscopy

1. INTRODUCTION

A knowledge of the atomic identities, positions, and bonding mechanisms within the first 3–5 layers of a surface is essential to any quantitative microscopic understanding of surface phenomena. This implies knowing bond directions, bond distances, site symmetries, coordination numbers, and the degree of both short-range and long-range order present in this selvedge region. A number of surface-structure probes have thus been developed in recent years in an attempt to provide this information.[1] Each of these methods has certain unique advantages and disadvantages, and they are often complementary to one another.
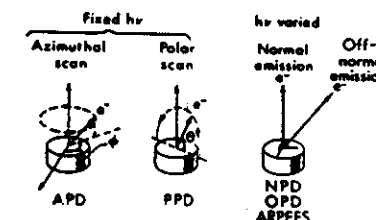
We will here concentrate on the basic experimental and theoretical aspects of photoelectron diffraction (PD or PhD) and its close relative, Auger electron diffraction (AED). Although the first observations of strong diffraction effects in X-ray photoelectron emission from single-crystal substrates by Siegbahn et al.[2] and by Fadley and Bergstrom[3] took place almost 20 years ago, and the use of such effects at lower energies to determine surface structures was proposed by Liebsch[4] 15 years ago, it was not until about 10 years ago that quantitative experimental surface-structure studies were initiated by Kono et al.,[5] Woodruff et al.,[6] and Kevan et al.[7] By now both photoelectron diffraction and Auger electron diffraction are becoming more widely used to study surface atomic geometries.[8-13] We will thus consider here both the present status and future prospects of these methods, and then return at the conclusion of this chapter to make a critical comparison of them with several other surface-structure probes such as LEED, grazing incidence X-ray scattering (GIXS), and scanning tunneling microscopy (STM).

The basic experiment in PD or AED involves exciting a core photoelectron or a relatively simple core-like Auger transition from an atom in a single-crystal environment and then observing modulations in the resulting peak intensities that are due to final-state scattering from atoms neighboring the emitter. For a general Auger peak of the type XYZ, it is thus important that the upper levels Y and Z involved are not so strongly influenced by chemical bonding as to induce an anisotropy in emission that is more associated with initial-state electronic structure. The directly emitted photoelectron- or Auger electron–wave exhibits interference with various scattered waves, and this interference pattern is analyzed to derive structural information. Peak intensities can be monitored as a function either of the emission direction or, in the case of photoelectron diffraction, of the exciting photon energy. In AED, excitation can also derive from anything producing core holes: an electron beam, VUV/soft-X-ray radiation, or even an ion beam.

The three basic types of measurement possible are as shown in Fig. 1: an azimuthal or ϕ scan, a polar or θ scan, and, for photoelectron diffraction, a scan of energy in a normal or off-normal geometry. Several abbreviations and acronyms have arisen in connection with such measurements. With soft X-ray excitation at about 1.2–1.5 keV at the typical X-ray photoelectron spectroscopy (XPS) limit, scanned-angle measurements have been termed X-ray photoelectron diffraction (XPD).[5,9] Scanned-energy photoelectron measurements spanning the VUV-to-soft-X-ray regime have also been called normal photoelectron diffraction (NPD),[7,8,14] off-normal photoelectron diffraction (OPD),[15] or angle-resolved photoemission fine structure (ARPEFS)[8] to emphasize their similarity to the more familiar surface extended X-ray absorption fine structure (SEXAFS).[16] Both standard X-ray sources and synchrotron radiation can be used for excitation, with photon energies being as low as 60 eV[6,17,18] and as high as a few keV.[7,8,19] Synchrotron radiation adds the capability of varying the photon energy continuously and of studying the dependence of the diffraction on polarization.

The degree of modulation of intensity observed in PD or AED experiments can be very large, with overall values of anisotropy as high as $(I_{max}-I_{min})/I_{max} = \Delta I/I_{max} = 0.5–0.7$. Thus, it is not uncommon to observe 30–50% changes in the peak intensity as a function of direction or energy, and such effects are relatively easy to measure. This is by contrast with the related surface-structure technique

FIGURE 1. The three basic types of photoelectron or Auger electron diffraction measurement: an azimuthal (ϕ) scan at constant polar angle, sometimes referred to as azimuthal photoelectron diffraction or APD; a polar (θ) scan at constant azimuthal angle, referred to as polar photoelectron diffraction or PPD; and a scan of $h\nu$ in fixed geometry that can be done only in photoelectron diffraction and for emission either normal or off-normal to the surface (denoted NPD or OPD, respectively). The scanned-energy type has also been referred to as angle-resolved photoemission fine structure or ARPEFS. Note that θ is measured with respect to the surface.

Fixed $h\nu$ — Azimuthal scan — Polar scan
$h\nu$ varied — Normal emission — Off-normal emission

APD   PPD   NPD OPD ARPEFS

of SEXAFS,[16] in which typical modulations are about one tenth as large. This difference arises from the fact that SEXAFS effectively measures an angle-integrated photoelectron diffraction pattern as a function of energy, and it is not surprising that this integration averages over various phases and leads to considerably lower relative effects.

We shall consider both scanned-angle photoelectron and Auger results and scanned-energy photoelectron results here. To date, scanned-angle studies are much more numerous; this is due to their greater simplicity, since scanned-energy work has several requirements in addition: the sweeping of photon energy with a work has several requirements in addition: the sweeping of photon energy with a synchrotron radiation source, the correct normalization of photon fluxes and electron-analyzer transmissions as a function of energy, and the possibility of allowing for interference between Auger peaks and photoelectron peaks in certain kinetic-energy ranges. Finally, it requires more-complex theoretical calculations in that scattering phase shifts and other nonstructural parameters have to be generated for all of the energies in a scan.[8,19-22] However, an advantage in scanned-energy work is that Fourier transform (FT) methods can be used to estimate the path-length differences for various strong scatterers.[8,20-22]

A key element in either photoelectron or Auger electron diffraction is the energy dependence of the relevant elastic-scattering factors. Figure 2 illustrates this for the case of atomic Ni with curves of the plane-wave scattering amplitude $|f_{Ni}|$ as a function of both the scattering angle θ_{Ni} and the electron energy. For low energies of 50–200 eV, it is clear that there is a high amplitude for scattering into all angles. For the intermediate range of about 200–500 eV, it is a reasonable approximation to think of only forward scattering ($\theta_{Ni} = 0°$) and backscattering ($\theta_{Ni} = 180°$) as being important. However, at energies above 500 eV, we see that the scattering amplitude is significant only in the forward direction, in which it is strongly peaked. The degree of forward peaking increases as the energy is increased. The utility of such forward scattering at higher energies in surface-structural studies was noted in very early XPD investigations,[5,23] and it has more recently been termed a "searchlight effect"[11] or "forward focusing"[24] in connection with XPD analyses of epitaxial overlayers. This effect turns out to be one of the most useful and simply interpretable aspects of higher-energy photoelectron or Auger electron diffraction, and we will make reference to it in several of the examples considered in following sections. These qualitative observations con-
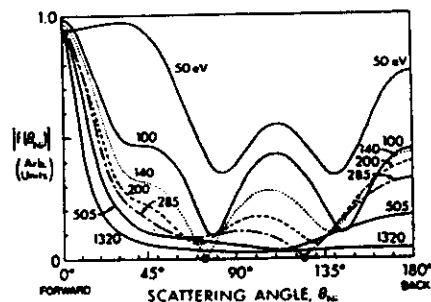

FIGURE 2. Nickel plane-wave scattering factor amplitudes $|f_{Ni}|$ as a function of both the scattering angle θ_{Ni} and the photoelectron kinetic energy. Note the zeroes occurring for both 140 eV and 285 eV, which have been termed a generalized Ramsauer–Townsend effect. (From Ref. 21.)

cerning the energy dependence of the scattering factor will later also assist in explaining which multiple scattering effects may be the most significant. A special aspect of such scattering factors is that they may exhibit zeroes for certain angles and energies; this has been termed a generalized Ramsauer–Townsend effect, and its influence on the analysis of ARPEFS data is considered elsewhere.[21,25]

A final important aspect of either photoelectron or Auger electron diffraction is that both are *atom-specific* probes of *short-range order*. Thus, each type of atom in a sample can in principle be studied, and each will have a unique diffraction signature associated with the neighbors around it. Previous work shows that the principal features of diffraction curves are due to the geometry of the first 3–5 spheres of scatterers around a given emitter, although data may exhibit useful fine structure that is associated with scatterers as far as 20 Å away.[20,26] This short-range sensitivity is thus shared with SEXAFS. We will later point out the potential uses of PD and AED in studying the degree of order present in the near neighbors of the emitter.

The remainder of this chapter begins by briefly reviewing the experimental requirements of these methods and considering both the simplest single-scattering model and other more accurate models that have been used to analyze both PD and AED data. The bulk of the text discusses several illustrative cases to which these techniques have been applied. This is not intended to be an exhaustive listing of all such studies to date, but the examples have been chosen to demonstrate certain basic phenomena, to illustrate the range of structural information that can be obtained, and to provide some idea of the different classes of systems that can be fruitfully studied. In certain cases, the limitations of the analysis or the need for future improvements are pointed out. Finally, some particularly interesting new directions for the future are discussed, and comparisons to other currently used structural probes are also made.

The studies discussed represent a mixture of work utilizing both standard X-ray or electron excitation sources and synchrotron radiation, with the number of investigations using standard sources certainly being greater to date. Thus, the methods discussed here are not limited to synchrotron radiation, by contrast with several others discussed in this volume.[27,28] However, both PD and AED will benefit greatly by the use of the higher-intensity facilities in the vacuum ultraviolet/soft X-ray range that are now becoming more available, and we return to this point toward the end of the chapter.

2. EXPERIMENTAL CONSIDERATIONS

The basic experimental requirements for carrying out photoelectron or Auger electron diffraction measurements are relatively simple. A minimal experiment can consist of the excitation source, a specimen holder with only one axis of angular motion (usually the polar angle as defined in Fig. 1), and an electron energy analyzer with an angular resolution of at least approximately ±5°. Thus, most of the commercially available hemispherical analyzers are suitable, and even a cylindrical mirror analyzer (CMA) with some sort of baffle at its entry slit can be used. Peak intensities can be measured very simply as the difference in

height between some point at the maximum and a point in the high-energy background. Measurements at this level are thus quite easy to take, and interesting surface-structural information has been obtained from them.[11]

Going beyond this minimal experiment to be able to tap all of the information available in the diffraction pattern involves several possible elaborations:

• The specimen holder should have both polar and azimuthal axes of rotation (cf. Fig. 1) so that the electron emission direction can be oriented arbitrarily with respect to the surface. The optimal scanning capabilities in this case are to be able to vary θ from grazing excitation incidence to grazing electron exit and to vary ϕ over a full 360° or more. The latter is very useful for establishing the symmetry of the surface and for verifying the reproducibility of features from one symmetry-equivalent azimuthal direction to another. Scanning ϕ over its full range is the most difficult to achieve in practice if there are electrical or mechanical connections to the sample for heating, cooling, or measuring temperature, but designs of this type have been in use for some time.[9] The reproducibility and accuracy of both of these motions should be at least ±0.5°, with even smaller values on the order of ±0.1° being required for very high angular resolution work.

• Automated scanning of spectra, determining of peak intensities by more accurate area-integration and/or peak-fitting procedures, and stepping of angles under computer control are also essential for efficiently obtaining the most reliable data. Systems for doing this are discussed elsewhere.[9,29]

• It also may be desirable to rotate both the specimen and the analyzer (or excitation source) on two axes so as to be able to orient the excitation source at various positions with respect to the electron emission direction. In photoelectron diffraction, this permits making use of the radiation polarization to preferentially excite the direct wave toward different scatterers while at the same time observing the electron intensity along a special direction.[8,19] This is particularly important in studies utilizing synchrotron radiation. In Auger electron diffraction, it can also be useful for assessing the degree to which the penetration of the exciting flux along different incidence directions influences the outgoing diffraction pattern, even though results to date indicate that such effects are minor.[30] (Similar anisotropic penetration might also be expected with X-rays due to Bragg reflections,[2,3] but such effects have so far not been found to be significant in photoelectron diffraction patterns.)

• Improving the angular resolution of the analyzer to the order of ±1.0° has also been found to yield data at higher energies with considerably more fine structure.[10,26] Achieving this may involve specially designed entrance optics,[31,32] or more simply the use of movable tube-array baffles at the entry to a more standard analyzer.[33] High-resolution results of this kind will be discussed in more detail in sections 4.2.1, 4.2.2, and 5.1.

• Improving the energy resolution of the system to on the order of 0.1 eV is also desirable, because it permits resolving small chemical shifts or surface shifts of core levels and studying the diffraction patterns of these species separately.[18]

• Scanning angle or energy obviously involves an added cost in time for any

study, and so it is desirable to have the highest overall count rates. This can be achieved by using a more-intense excitation source (as, for example, from insertion-device-generated synchrotron radiation) and/or the most efficient and highest-speed electron analyzer and detection system. Making the latter as effective as possible is important, since there are always potentially deleterious effects of radiation damage as the excitation intensity is increased. Analyzer improvements include the use of multichannel energy-detection systems involving several single-channel electron multipliers or a microchannel plate[32,34] and the use of special spectrometer geometries in which spectra at several angles can be recorded at the same time.[35-37] However, a potential disadvantage of systems recording several angles at once is that the angular resolution may be limited, particularly if it is desired to scan kinetic energies to several hundred eV. A final method for increasing data acquisition rates with a pulsed synchrotron radiation source is to use a time-of-flight analysis system;[38] a logistical problem with such systems however, is that they may require running the storage ring in a less frequently used "timing" mode with fewer electron bunches. Leckey[39] has recently reviewed many of the more novel proposals for analyzers with high energy resolution, high angular resolution, and/or high data acquisition rates.

• Finally, if scanned-energy photoelectron diffraction is to be performed, it is essential to use a reasonably stable synchrotron radiation source and to have an analyzer system whose transmission properties as a function of energy are well understood. This is because photon energies must be scanned in small steps over a total period on the order of hours in present experiments, and the influences of both the decay of photon flux with time and the change of the analyzer's sensitivity with kinetic energy must be corrected out of the final intensity data so as to yield something that is truly proportional to the energy-dependent photoelectric cross section in a given emission direction. Methods for making these corrections are discussed elsewhere.[8,20]

3. THEORETICAL MODELING

3.1. Single-Scattering Theory

3.1.1. Overview of Model

Since the first theoretical paper on low-energy photoelectron diffraction by Liebsch,[4] several detailed discussions of the modeling of photoelectron and Auger electron diffraction have appeared in the literature.[9,15,21,24,25,40-45] Thus, we will begin here by presenting only the essential ingredients of the simplest approach, the single-scattering cluster (SSC) model, and then comment toward the end of this section on several improvements that can be made to it, as well as on some effects expected due to multiple scattering (MS) events.

The basic elements of this single-scattering cluster model are shown schematically in Fig. 3(a). The fundamental assumptions are essentially identical to those used in describing extended X-ray absorption fine structure (EXAFS),[41] and a similar model has also been applied some time ago to angle-resolved Auger emission at very low energies of ≤100 eV.[40] We consider photoelectron emission first and then discuss the modifications required to describe Auger emission.
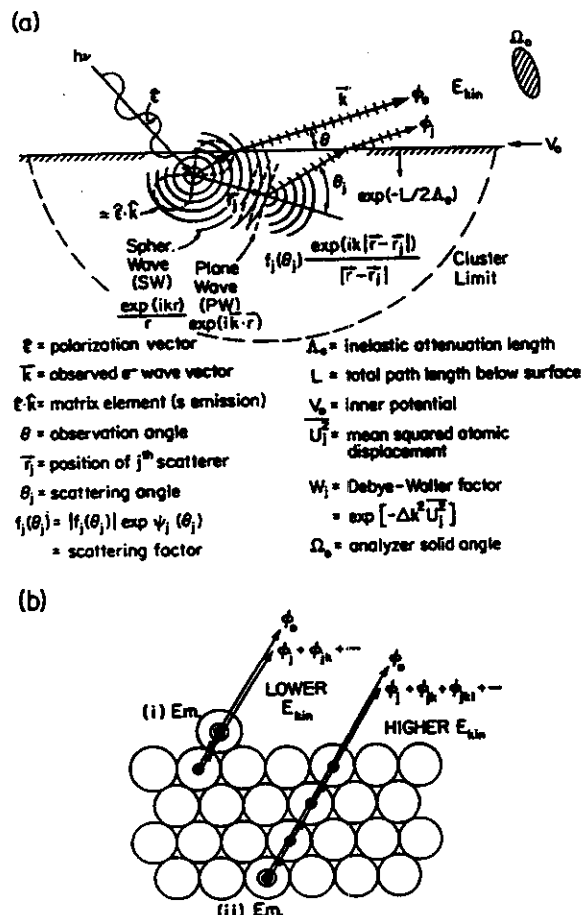
(a)

ê = polarization vector

$\overline{\text{k}}$ = observed e⁻ wave vector

ê·$\hat{k}$= matrix element (s emission)

θ = observation angle

$\overline{r}_j$= position of jth scatterer

θ$_j$ = scattering angle

f$_j$(θ$_j$)= |f$_j$(θ$_j$)| exp ψ$_j$ (θ$_j$)

= scattering factor

Λ$_e$= inelastic attenuation length

L = total path length below surface

V$_o$ = inner potential

$\overline{U_j^2}$ = mean squared atomic displacement

W$_j$ = Debye-Waller factor

= exp[-Δk²$\overline{U_j^2}$]

Ω$_o$ = analyzer solid angle

(b)

FIGURE 3. (a) Illustration of the assumptions used in the single-scattering cluster (SSC) model, with various important quantities indicated. (b) Two types of multiple-scattering corrections to the SSC model that may be significant for certain energies and geometries: (i) at lower energies of <200 eV, model that may be significant for certain energies and geometries: (i) at lower energies of <200 eV, backscattering from a nearest-neighbor atom behind the emitter and then forward scattering by the emitter (from Ref. 25); (ii) multiple forward scattering along lines of closely spaced atoms that leads to a reduction of the expected intensity enhancement, particularly at higher energies of >500 eV (from Refs. 24 and 73).

Radiation with polarization ê is incident on some atom in a cluster, from which it ejects a core-level photoelectron. (In Fig. 3a, the emitting atom is shown near the surface, but it could as well be any atom in the substrate.) If the initial core-electron wave function is denoted by ψ$_c$(r) and the final photoelectron wave function corresponding to emission with wave vector k by ψ(r, k), then the

observed intensity will be given in the dipole approximation by

$$I(\text{k}) \propto |\langle \psi(\text{r}, \text{k})| \, \hat{\text{e}} \cdot \text{r} \, |\psi_c(\text{r})\rangle|^2. \tag{1}$$

The final-state wave function in single scattering is further described as being the superposition of a direct wave ϕ_0(r, k) and all singly scattered waves ϕ_j(r, r$_j$ → k) that result from initial ϕ_0 emission toward a scatterer j at r$_j$ and then subsequent scattering so as to emerge from the surface in the direction of k. Thus, the overall wave function can be written as[21,41]

$$\psi(\text{r}, \text{k}) = \phi_0(\text{r}, \text{k}) + \sum_j \phi_j(\text{r}, \text{r}_j \to \text{k}). \tag{2}$$

Because the detector is situated at essentially infinity along k, all of the waves in Eq. (2) can finally be taken to have the limiting spherical forms $\phi_0 \propto \exp(ikr)/r$ or $\phi_j \propto \exp(ik|\text{r} - \text{r}_j|)/|\text{r} - \text{r}_j|$, although the effective amplitudes and phases of each type in a given direction will be modulated by the photoexcitation matrix element and, for each ϕ_j, also $\exp(ikr_j)/r_j$ and the scattering factor. Flux conservation also dictates that the portion of ϕ_0 which passes to the scatterer j to produce ϕ_j decays in amplitude as a spherical wave, or as $1/r_j$. This decay is a principal reason why PD and AED are short-range probes, although the effects of inelastic scattering contribute additionally to this. If the scattering angle is θ_j, the overall path length difference (PLD) between ϕ_0 and any ϕ_j is $r_j(1 - \cos\theta_j)$, and it is these PLDs that provide most of the bond-length information in photoelectron or Auger electron diffraction.

3.1.2. Matrix Elements and Final-State Interference

When this model has been applied to photoelectron emission, the dipole matrix element has usually been treated as involving a p-wave final state (that is, the case that is appropriate for emission from an s subshell). This yields a matrix-element modulation of the form ê · $\hat{k}$ for an arbitrary direction of emission $\hat{k}$.[21,41] For emission from other subshells with l not equal to zero, more complex expressions including both of the interfering l + 1 and l − 1 channels are involved,[43,45-47] and we return below to consider how important these effects can be. However, at higher energies, the assumption of a p-wave final state has been found to be reasonably adequate in several prior studies of non-s emission.[9,10,48-50]

Since the differential photoelectric cross section $d\sigma_{nl}(\hat{\text{e}}, \text{k})/d\Omega$ is proportional to intensity rather than amplitude, another possible approximation might be to use a ϕ_0 modulation of $[d\sigma_{nl}(\hat{\text{e}}, \text{k})/d\Omega]^{1/2}$.[51] Although this is not strictly correct and it also does not account for possible sign changes in the matrix element with direction due to the photoelectron parity,[15,52] it may be a reasonably adequate approximation for higher-energy XPD in which the forward-dominated electron-scattering process selects out r$_j$ choices very nearly parallel to k. That is, for the range of r$_j$ directions near the k direction that produce significant scattering, the matrix element varies little, so that a very precise description of it is not required. In fact, predicted XPD patterns have not been found to be very sensitive to the

exact way in which the matrix-element modulation is included. At lower energies, such simplifications are not generally possible, however, and Treglia[53] has, for example, recently shown that not using the correct final-state angular momenta can have a strong effect on predicted azimuthal diffraction patterns at energies of about 30 eV.

Such final-state momentum and interference effects have been studied in more detail recently by Friedman and Fadley,[47] who have made use of a newly developed Green's function matrix approach due to Rehr and Albers.[54] Representative results as a function of electron kinetic energy are presented in Fig. 4. Here, a Cu emitter is 3.5 Å away from a single Cu scatterer, and three different electron kinetic energies of 100, 300, and 1000 eV are considered. Scattering is in all cases full spherical wave. The intensity fluctuations as a function of scattering angle are normalized to the unscattered intensity I_0 as $\chi = [I - I_0]/I_0$. In order to illustrate in these calculations only the effects of changing the final-state angular momenta that are involved, emission from a Cu 2p orbital was taken as a reference. For this p-emission case, the correct final-state interference involves s
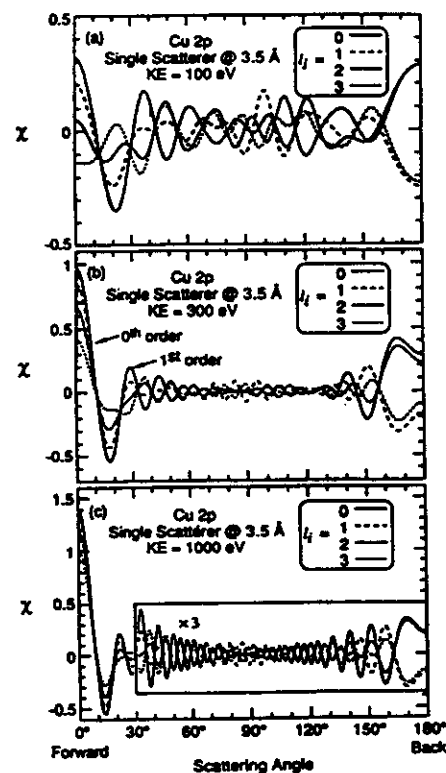

FIGURE 4. Theoretical calculations of electron scattering from a single Cu atom at a distance of 3.5 Å from the emitter and for energies of (a) 100 eV, (b) 300 eV, and (c) 1000 eV. Intensity is shown as the normalized function $\chi = (I - I_0)/I_0$. Full spherical-wave (SW) scattering is used, and different final-state assumptions are compared: $l_f =$ 0 (s to a single p channel), $l_f = 1$ (p to interfering s + d channels), $l_f = 2$ (d to p + f), and $l_f = 3$ (f to d + g). The radiation is taken to be unpolarized, with the plane of polarization lying in the plane of r_{Cu} and k. Note the sign reversals due to photoelectron parity in the backscattering direction. (From Ref. 47.)

and d waves, and includes the radial matrix elements R_s and R_d and the phase shifts δ_s and δ_d. These have been calculated using an atomic cross-section program due to Manson.[55] The ratio R_d/R_s changes relatively little, from 4.62 to 3.91, as we go from 100 eV to 1000 eV. The curves shown for $l_f = 0$ are the simple limit, discussed previously, of an s initial state and single p final state with no interference. The results for $l_f = 1$ are the correct description of Cu 2p emission. For the other two cases of $l_f = 2$ and $l_f = 3$ shown, emission into final waves at $l_f = 1$ and 3 and $l_f = 2$ and 4, respectively, is allowed, and the same radial matrix elements R_s and R_d and phase shifts δ_s and δ_d were used for the $l_f = l_i + 1$ and $l_f = l_i - 1$ channels in both cases. These sets of four curves thus permit systematically observing only the effect of the different final-state character and interference associated with the dipole matrix element.

Several general conclusions can be drawn from the curves of Fig. 4:

• Increasing the angular momenta in the final state from 1 to 0 + 2 to 1 + 3 to 2 + 4 is found to decrease systematically the amplitude of forward scattering, thus constituting a reason for which calculations using the p final state may overpredict the degree of anisotropy for emission from subshells with $l_i \geq 1$.

• In the backscattering direction, the parity of the photoelectron waves is evident, since the odd waves from $l_f = 0$ and 2 exhibit the same sign of χ, and the opposite sign is seen for the even waves from $l_f = 1$ and 3. The previously discussed approximation of using the square root of the differential cross section neglects these sign differences. It implicitly assumes photoelectron waves of even character unless an ad hoc sign change is introduced as appropriate for emission angles greater than 90° with respect to the polarization vector.[15]

• The smallest differences between different final-state angular momenta are for the highest energy, where, in the dominant forward direction, the main effect is a reduction of amplitudes in the forward scattering direction, but little change occurs in the shapes of the '0th-order' peak at a scattering angle of 0° and, for $l_f < 3$, also in the 1st-order peak at about 22°. However, as energy is decreased to 100 eV, the differences between the curves become increasingly more significant, and they begin also to involve phase changes in the regions of both of these peaks nearest forward scattering.

• At the highest energy typical of the XPS limit, one thus expects the general shape of the 0th order or forward scattering peak to be the same regardless of final-state angular momenta, and to see a general suppression of the relative importance of the higher-order features.

Overall, these results indicate that the use of the correct final-state angular momenta with interference will probably be important for energies below about 500 eV. For higher energies of 1000 eV or move, forward scattering should be reasonably well treated by the simple p final state (as has been verified in prior XPS studies), although both overall anisotropies and the relative intensities of higher-order features may be overestimated. Similar conclusions concerning the suppression of higher-order diffraction features have been reached by both Parry[46] and Sagurton[56] using more approximate calculations based upon plane-wave scattering and/or plane-wave final states.

Keeping in mind the discussion of the last paragraphs, we shall for simplicity and heuristic reasons in what follows still use the p final state and its factor $\hat{\epsilon} \cdot \hat{k}$ in describing photoelectron emission.

3.1.3. Electron—Atom Scattering

The electron—atom scattering that produces ϕ_j is most simply described by a complex plane-wave (PW) scattering factor

$$f_j(\theta_j) = |f_j(\theta_j)| \exp\left[i\psi_j(\theta_j)\right].\tag{3}$$

where $\psi_j(\theta_j)$ is the phase shift associated with the scattering. The scattering factor is in turn calculated from partial-wave phase shifts δ_l according to the usual expression:

$$f(\theta) = (2ik)^{-1}\sum_{l=0}^{\infty} (2l + 1)[\exp(2i\delta_l) - 1]P_l(\cos\theta),\tag{3'}$$

where the P_l are Legendre polynomials. For large r, the scattered wave ϕ_j is thus proportional to $f_j(\theta_j) \exp(ik|\mathbf{r} - \mathbf{r}_j|)/|\mathbf{r} - \mathbf{r}_j|$, with an overall phase shift relative to ϕ_0 of $kr_j(1 - \cos\theta_j) + \psi_j(\theta_j)$ that is due to both path-length difference and scattering. The use of this form for ϕ_j implicitly assumes that the portion of ϕ_0 incident on the jth scatter has sufficiently low curvature compared to the scattering potential dimensions to be treated as a plane wave. This is the so-called small-atom approximation,[57] and its limitations in comparison to the more accurate spherical-wave (SW) scattering[21,25,58,59] of Fig. 4 are discussed below.

The PW scattering factor $f_j(\theta_j)$ is thus determined by applying the partial-wave method to a suitable spherically symmetric scattering potential for each atomic type in the cluster. The number of partial-wave phase shifts needed for convergence goes up with energy, and for a typical scattering potential of effective radius 1.5 Å would be ≥ 8 for $E_{kin} = 500\,eV$ and ≥ 24 for 1500 eV. Tabulations of free-atom scattering factors at energies going up to the XPS regime also exist.[60] Alternatively, scattering potentials more appropriate to a cluster of atoms with overlapping charge densities and potentials can be constructed via the muffin-tin model employed, for example, in LEED theory.[61] The free-atom f_j is generally larger in magnitude in the forward direction than its muffin-tin counterparts due to the neglect of charge and potential overlap.[42] Both types of f_j have been employed in higher-energy PD and AED calculations, and they usually do not yield markedly different $I(\mathbf{k})$ curves, although the use of the free-atom f_j is expected to predict slightly higher peak intensities due to its larger amplitudes in the forward direction. The PW scattering factor amplitudes in Fig. 2 were calculated using the more accurate muffin-tin procedure. Whatever procedure is used to calculate these scattering factors, there are two useful generalizations concerning their behavior as atomic number is varied:

• The forward scattering amplitude $|f_j|$ at higher energy is found to be primarily sensitive to the radius of the atom (or muffin tin) involved. It is for this

reason that free-atom forward scattering amplitudes are always larger than those for a muffin tin in which the potential is effectively truncated at the tin radius. This behavior can be rationalized by a classsical argument in which it is noted that forward scattering trajectories graze the outer reaches of the scattering potential and so are only deflected slightly; these trajectories are thus primarily sensitive to the outer regions of the potential.

• The backscattering amplitude at higher energy is by contrast found to increase monotonically with atomic number. This also is expected from a classical argument in which backscattering involves strongly deflected trajectories that pass close to the nucleus.

3.1.4. Inelastic Scattering

The effects of *inelastic* scattering on wave amplitudes during propagation below the surface must also be included. If intensity falls off as $\exp(-L/\Lambda_e)$, where L is an arbitrary path length below the surface and Λ_e is the inelastic attenuation length, then *amplitude* is expected phenomenologically to fall off as the square root of this or $\exp(-L/2\Lambda_e) = \exp(-\gamma L)$. Each wave ϕ_0 or ϕ_j is multiplied by such an exponential factor involving an L value which includes the total path length below some surface cutoff point (cf. Fig. 3a). This surface cutoff is often chosen to be the substrate surface as defined by hard-sphere atoms,[42] although this choice should not influence the diffraction patterns unless some atoms are positioned above the cutoff. Thus, the attenuation coefficient $\gamma = 1/2\Lambda_e$, although γ values up to 1.3–2 times this have been suggested in prior EXAFS,[41,62] AED,[12] and PD[42,48,63] analyses. That is, the effective inelastic attenuation length Λ_e in these diffraction experiments is suggested to be about 0.50–0.75 times literature values based upon intensity-attenuation measurements or theoretical calculations.[64] In fact, some inelastic attenuation lengths derived from EXAFS measurements do not appear to take account of the difference between amplitude and intensity mentioned above.[62]

These reduced values of Λ_e are not surprising in view of several factors: Uncertainties of at least ±20% are common in measurements of attenuation lengths,[64,65] and some recent measurements in fact yield values that are significantly lower than others in the literature.[65] The effects of elastic scattering and diffraction on intensities can introduce additional uncertainties of this order,[66,67] and it is, for example, now well recognized that the actual mean free path between inelastic scattering events is about 1.4 times the attenuation length discussed above. Finally, the effective attenuation length in a diffraction measurement should be shorter than in a simple intensity-attenuation experiment, because quasielastic scattering events of small energy (e.g., from phonons) that leave the electron kinetic energy within the peak being measured[68] can still introduce direction changes and phase shifts that effectively remove such electrons from the coherent intensity for diffraction. In addition, multiple elastic-scattering events similarly cause a reduction of the effective coherent intensity in a single-scattering theory. Thus, one overall expects effective attenuation lengths related as $\Lambda_e(\text{intensity}) > \Lambda_e(\text{multiple-scattering diffraction}) > \Lambda_e(\text{single-scattering diffraction}).$

Fortunately, electron diffraction features for most cases are not strongly affected by varying Λ_e over its plausible range, and so its choice is in general not crucial to final structural conclusions. Nonetheless, it is desirable to verify this insensitivity by varying Λ_e in model calculations.[42,48,63]

3.1.5. Vibrational Effects

Vibrational attenuation of interference effects is furthermore potentially important and can be included in the simplest way by multiplying each ϕ_j by its associated temperature-dependent Debye–Waller factor:

$$W_j(T) = \exp\left[-\Delta k_j^2 \overline{U_j^2}(T)\right] = \exp\left[-2k^2(1 - \cos\theta_j)\overline{U_j^2}(T)\right], \qquad (4)$$

where Δk_j is the magnitude of the change in wave vector produced by the scattering, and $\overline{U_j^2}(T)$ is the temperature-dependent one-dimensional mean-squared vibrational displacement of atom j. At this level of approximation, $\overline{U_j^2}$ is assumed to be isotropic in space, and any correlations in the movements of near-neighbor atoms are neglected. (The importance of *correlated* vibrational motion in certain types of lower-energy diffraction experiments is considered below.) Suitable bulk and surface $\overline{U_j^2}$ values or Debye temperatures can be obtained from the literature. At high energy, the electron scattering is significant only when θ_j is rather close to zero, and this acts through the $(1 - \cos\theta_j)$ factor in the argument of Eq. (4) to yield W_j very close to unity for all important scattered waves. So vibrational effects are to first order not very significant in forward-scattering-dominated XPD or AED, although they can be very important in LEED, EXAFS, and lower-energy PD and AED, where backscattering is the dominant diffraction mode and thus $1 - \cos\theta_j$ is a maximum.

An alternate method for allowing for vibrational effects is to assume some probability distribution of atomic positions due to vibration (as, for example, a harmonic-oscillator envelope) and then to numerically sum separate weighted diffraction intensities for all possible combinations of atomic positions. This is cumbersome, but it has been used to quantitatively look at the effects of specific types of wagging molecular vibrations at surface.[23,69]

3.1.6. Single-Scattering Cluster Model

With these assumptions, the simplest SSC–PW expression for photoelectron intensity $I(k)$ can now be written down from Eqs. (1–3) as

$$I(\mathbf{k}) \propto \int \left| \boldsymbol{\ell} \cdot \hat{\mathbf{k}} e^{-\gamma L} + \sum_j \frac{\boldsymbol{\ell} \cdot \hat{\mathbf{r}}_j}{r_j} |f_j(\theta_j)| \, W_j e^{-\gamma L_j} \{\exp i[kr_j(1 - \cos\theta_j) + \psi_j(\theta_j)]\} \right|^2 d\boldsymbol{\ell}$$

$$+ \sum_j \int (\boldsymbol{\ell} \cdot \hat{\mathbf{r}}_j)^2 \frac{|f_j(\theta_j)|^2}{r_j^2}(1 - W_j^2)e^{-2\gamma L_j} \, d\boldsymbol{\ell}. \qquad (5)$$

Here, $\boldsymbol{\ell} \cdot \hat{\mathbf{k}}$ and $\boldsymbol{\ell} \cdot \hat{\mathbf{r}}_j$ represent p-wave photoemission matrix-element modulations along the unit vectors $\hat{\mathbf{k}}$ and $\hat{\mathbf{r}}_j$, respectively, and $\exp(-\gamma L)$ and $\exp(-\gamma L_j)$ are

appropriate inelastic attenuation factors. Thus, $(\boldsymbol{\ell} \cdot \hat{\mathbf{k}}) \exp(-\gamma L)$ is the amplitude of the direct wave $\phi_0(\mathbf{r}, \mathbf{k})$ and $(\boldsymbol{\ell} \cdot \hat{\mathbf{r}}_j)|f_j(\theta_j)| \, W_j \exp(-\gamma L_j)/r_j$ is the effective amplitude of $\phi_j(\mathbf{r}, \mathbf{r}_j \rightarrow \mathbf{k})$ after allowance for both inelastic scattering and vibrational attenuation of interference. The complex exponential allows for the total final phase difference between ϕ_0 and each ϕ_j.

The integrals on $\boldsymbol{\ell}$ simply sum over the different polarizations perpendicular to the radiation progagation direction, as appropriate to the particular case at hand. Closed-form expressions for a totally unpolarized source that are applicable to high-energy work are given elsewhere;[42] however, the simplest way to carry out this integration for a general case is just to sum the intensities for two perpendicular polarizations of convenient orientation.

The second $\sum_j$ corrects the first absolute value squared for the incorrect inclusion of Debye–Waller attenuations in terms involving a product of a scattered wave with itself. That is, in expanding the absolute value squared, only products involving unlike waves like $\phi_0\phi_j^*$ or $\phi_j\phi_l(j \neq l)$ should include Debye–Waller products of W_j or W_jW_l, respectively. The $(1 - W_j^2)$ factor in the second summation is thus necessary to yield overall correct products of the form $\phi_j\phi_j^*$ without any W_j^2 factor. The second sum has been called thermal diffuse scattering,[46] and it is often quite small with respect to the overall modulations. Equation (5) is thus the basic starting point of the single-scattering cluster model.

In modifying this model to describe Auger emission, the usual assumption is that the much freer mixing of angular momenta in the final state overall leads to an outgoing wave with s character.[12,40,70-73] Although selection rules do limit the allowed final angular momentum states in Auger emission,[72] for certain cases, the $l = 0$ channel is dominant. Also, if filled subshells are involved in both the initial and final levels of the transition, the implicit sums over all initial and final m_l values would be expected to produce an overall distribution of emitted primary intensity that could be approximated as an s wave. Although it is possible for higher-l components to be present in the final state that could affect the scattering,[72,73] these are often found at higher energies to be minor effects.[12,70,71] For Auger emission into such an assumed s final state, we thus simply remove all factors involving $\boldsymbol{\ell} \cdot \hat{\mathbf{k}}$ and $\boldsymbol{\ell} \cdot \hat{\mathbf{r}}_j$ in Eq. (5). Non-s character in Auger final states deserves further study however.

It is also worth noting here that the cluster sum on j in Eq. (5) makes no explicit use of the 2- or 3-dimensional translational periodicities that may be present, even though the atomic coordinates $\mathbf{r}_j$ used as inputs may incorporate such periodicities. Thus, neither surface- nor bulk-reciprocal lattice vectors $\mathbf{g}$ are explicitly involved, and it is not appropriate at this level of description to speak of diffraction "beams" associated with certain $\mathbf{g}$ vectors as in LEED. However, in section 5.1 we will consider the relationship of this model to an alternative Kikuchi-band picture that does involve $\mathbf{g}$ vectors and the idea of Bragg reflections from sets of planes.

The last parameter of importance in actually using Eq. (5) is the range of j or the choice of a suitable cluster of atoms. This is done empirically so as to include all significant scatterers by verifying that the predicted diffraction patterns do not change in any significant way with the addition of further atoms at the periphery of the cluster. Clusters can range from a few atoms for near-normal high-energy emission from a vertically oriented diatomic molecule on a surface[23] to as many as

several hundred atoms for substrate emission in which both the emission and the scattering must be summed over several layers into the bulk.[42] In the latter case, each structurally unique type of atom emits incoherently with respect to the other, so that intensities from each must be added layer by layer. However, even for the largest clusters so far considered, the inherent simplicity of Eq. (5) still yields calculations which do not consume excessive amounts of computer time, especially by comparison with those necessary for such procedures as multiple-scattering LEED simulations.

A further physical effect of importance in making comparisons to experiment is the possibility of electron refraction at the surface in crossing the surface barrier or inner potential of height V_0. Even at the relatively high energies of XPS, for emission angles near grazing, refraction effects of a few degrees can be produced (cf. Fig. 14 in Ref. 9). Thus, for lower takeoff angles relative to the surface and/or lower kinetic energies, a proper allowance for refraction is necessary. This is accomplished most simply by using a suitable inner potential V_0 derived from experiment and/or theory to predict the internal angle of emission θ' for a given external propagation direction θ.[9] The resulting expression for an electron energy of $E'_{kin} = E_{kin} + V_0$ inside the surface is

$$\theta' = \cos^{-1}\left\{ \left[\frac{E_{kin}}{E_{kin} + V_0} \right]^{1/2} \cos\theta \right\}, \qquad (6)$$

where, as before, θ and θ' are measured with respect to the surface. In the presence of an adsorbate, the exact form of the surface potential barrier thus becomes important, as it may not then be possible to assume an abrupt rise to the vacuum level at the substrate surface. Also, the presence of adsorbate atoms may alter V_0 through changes in the work function, and these atoms also may occupy positions above the surface in which only a fraction of V_0 is appropriate. In some photoelectron diffraction studies, V_0 has also been treated as an adjustable parameter.[20,25,63] Although prior studies indicate that structural conclusions are not particularly sensitive to the choice of V_0,[25,42] it is important to realize that not allowing for it properly may shift theoretical diffraction patterns by as much as a few degrees with respect to the actual θ values at which they will be observed. The precise method of allowing for inner potential and related image–force effects has also been considered in more detail theoretically.[25]

We stress also at this point that any uncertainties in final structures associated with the choices of nonstructural parameters such as the scattering phase shifts, the attenuation length for inelastic scattering, vibrational attenuation, and the inner potential are equally well shared with the techniques of LEED, EXAFS, and SEXAFS, although in EXAFS/SEXAFS, empirical phase shifts from known structures can sometimes be used.

A final step in any realistic calculation based upon this model is to integrate the direction of emission k over the solid angle Ω_0 accepted into the electron analyzer. For most of the calculations reported here, this has been over a cone of ± 3.0–$3.5°$ half angle, although for certain high-resolution cases a smaller cone of ± 1.0–$1.5°$ has been used.

3.1.7. Improvements to the Model

We now consider some possible improvements to this simple SSC–PW model:

• A first possible correction is to choose a *more correct form for the primary wave as it leaves the emitter*. The SSC–PW result of Eq. (5) assumes a simple outgoing plane wave from the emitter which then scatters to produce an outgoing spherical wave from each scatterer. In fact, the correct primary wave should be of the type used in free-atom photoelectric cross sections and should consist of an ingoing spherical wave plus the outgoing plane wave.[21,41,45,74] Such a primary wave experiences the emitter potential and represents the correct solution to the Schrödinger equation inside of a muffin-tin-like region centered on the emitter. If this form of the primary wave is used, the equivalent of Eq. (5) with neglect of effects due to vibrations is:[21,41]

$$I(\mathbf{k}) \propto \int \left| \hat{\boldsymbol{\varepsilon}} \cdot \hat{\mathbf{k}} e^{-\gamma L} + \sum_j \frac{\hat{\boldsymbol{\varepsilon}} \cdot \hat{\mathbf{r}}_j}{r_j} |f_j(\theta_j)| e^{-\gamma L_j} \{\exp i[kr_j(1 - \cos\theta_j) + \psi_j(\theta_j)]\} \right.$$
$$\left. + \sum_j \frac{\hat{\boldsymbol{\varepsilon}} \cdot \hat{\mathbf{r}}_j}{r_j^2} f_j(\pi) f_{em}(\pi - \theta_j) e^{-\gamma(L + 2r_j)} \{\exp i[2kr_j]\} \right|^2 d\hat{\boldsymbol{\varepsilon}}. \quad (7)$$

This result, although still single scattering in assumption, now contains, through the scattering of the incoming wave, a second sum of terms that are the classic double scattering events of the type emitter → scatterer → emitter → detector discussed in EXAFS theory.[41] Because these added terms are in effect double scattering and also exhibit stronger attenuation due to both $1/r_j^2$ and $e_j^{-2\gamma r}$, this sum is expected for many cases to be a small correction to Eq. (5). This should be especially true for higher energies where backscattering is negligible. In fact, the inclusion of this sum can be shown to lead to the central-atom (emitter) phase shift that is always present in EXAFS theory, and we comment further on this later in this section.

• A next important correction is the use of *spherical-wave (SW) scattering* instead of the asymptotic and much simpler plane-wave (PW) scattering. The nature of such SW corrections in reducing forward scattering amplitudes in XPD was first pointed out some time ago,[23] but more recent studies have presented detailed comparisons of PW and SW results for different systems.[58,59] For example, Fig. 5 compares PW and SW scattering at energies from 50 eV to 950 eV,[58] with the results being displayed in a format identical to that of Fig. 4. Emission from an s level ($l_i = 0$, $l_f = 1$) to a single Ni scatterer 2.49 Å away is considered. For larger scattering angles ($\geq 40°$) and higher energies (≥ 200 eV), the PW and SW results are essentially identical. However, for lower energies and in the forward scattering direction, there are significant differences. In particular, for energies ≥ 100 eV, the forward scattering peak is significantly reduced in amplitude by a factor that can be as low as 0.5. As expected, the differences between PW and SW curves also decrease as the scatterer is moved away from the emitter,[58] because in the limit of a scatterer at infinity, the incident wave is
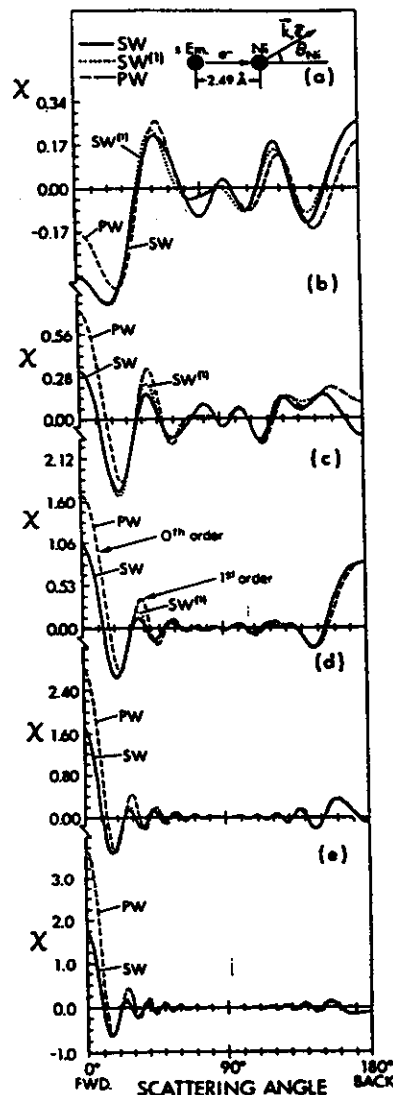
FIGURE 5. As in Fig. 4, but comparing plane-wave (PW) and spherical-wave (SW) scattering from a single Ni scatterer at a distance of 2.5 Å from the emitter with energies of (a) 50 eV, (b) 100 eV, (c) 200 eV, (d) 500 eV, and (e) 950 eV. Here, PW results are compared to SW results for the case of $l = 0$ (s emission to a single p channel). Polarization is parallel to the emission direction. The curves labeled SW[1] represent a first-order approximation to the full SW scattering. (From Refs. 21 and 58.)

planar. One general conclusion from these results is thus that, at higher energies, the primary effect of including curvature in ϕ_0 is to reduce the amplitudes of the forward-scattering peaks in $I(k)$ for near-neighbor atoms as compared to those predicted from Eq. (3).

Fortunately, such SW corrections can now be very simply and accurately

incorporated into the SSC framework via effective SW scattering factors developed by Barton and Shirley using a Taylor-series magnetic quantum number expansion (MQNE)[25] and by Rehr et al. using separable Green's function approaches.[45,54] For example, Rehr et al.[45] derive an equation identical to Eq. (7) in form, but in which the plane-wave scattering factors $f_j(\theta)$ are replaced by three effective spherical-wave scattering factors $f^{(1)}_{j,\text{eff}}(\theta, r_j)$, $f^{(2)}_{j,\text{eff}}(\pi, r_j)$, and $f^{(3)}_{j,\text{eff}}(\pi - \theta, r_j)$ that are used to describe the three types of scattering events present. These effective scattering factors depend on r_j, as they must converge to the PW result as r_j goes to infinity. They are also very simply calculable, involving expressions closely related to that in Eq. (3').

However, particularly at higher energies, the much simpler PW approximation is still found to yield results very similar in form to those with SW scattering, and it has been found possible to draw useful structural conclusions with it. Sometimes, PW scattering at high energy has been used together with an empirical reduction factor of forward scattering amplitudes by a factor of 0.4–0.5[42] that can be largely justified as being due to SW effects (cf. Fig. 5).

• An additional important correction for some cases is the use of correlated vibrational motion in which atoms that are near neighbors of the emitter have lower vibrational amplitudes relative to the emitter, and thus Debye–Waller factors for diffraction that are nearer unity. This correction is more important in special geometries and at lower energies for which large-angle or, particularly, backscattering events become more important, as first pointed out in connection with the interpretation of scanned-energy data by Sagurton et al.[21] and also discussed by Barton and Shirley.[25] This more correct form for vibrational attenuation involves a factor W^{corr}_j of the form:[21]

$$W^{\text{corr}}_j(T) = \exp\left[\frac{-\Delta k_j^2 \sigma_j^2(T)}{2}\right] = \exp\left[-k^2(1 - \cos\theta_j)\sigma_j^2(T)\right]. \quad (8)$$

where $\sigma_j^2(T) = \langle(\Delta\hat{k}_j \cdot u_j)^2\rangle$ is a thermal average of the projection of the atomic displacement u_j as measured with respect to the emitter onto the direction of the change in wave vector produced by the scattering $\Delta\hat{k}_j$. Thus, each scatterer in a photoelectron diffraction experiment is sensitive to a different type of vibrational displacement, varying from no effects for forward scattering, to small effects for small-angle scattering associated with components of u_j perpendicular to the emitter–scatterer axis, to maximum effects for backscattering associated with components of u_j along this axis. By contrast, in SEXAFS, it is only the along-axis components that contribute. Correlation effects are also expected to be largest for atoms that are backscatterers, because along-axis vibrations will be reduced more than those perpendicular to this axis. Ultimately, this might make it possible to measure anisotropies in vibration in a more precise way with temperature-dependent photoelectron diffraction, for example, by looking at the variation of different peaks in Fourier transforms of scanned-energy data. A first attempt at this has recently been made by Wang et al.[75] Also, even forward scattering features at high energy contain vibrational information because of peak broadening by motion perpendicular to a bond,[23,69] and this has permitted

Wesner et al.[76] to determine the vibrational amplitude anisotropy for an adsorbed molecule, as discussed further in section 4.1.3.

• A final aspect of the model which might be improved but which has only been discussed in a limited way to date is *more accurate allowance for both surface refraction and attenuation due to inelastic scattering*. Refraction has been treated differently from the phenomenological approach indicated here both by Lee[41] and by Tong and Poon,[77] who have considered the proper matching of the attenuated photoelectron wave inside the surface to the free electron wave outside the surface. However, the latter have found that, if refraction is allowed for in the way described here in calculating the path length for inelastic scattering in approaching the surface, the net result is very little different from the correct treatment of the wave matching. Another more complex problem is choosing the proper value for the inelastic attenuation length: As we have noted above, these lengths in electron-diffraction problems appear empirically to be only about 0.5–0.75 times the typical literature values based upon intensity attenuation. It would be desirable to understand these attenuation lengths more quantitatively, including both elastic and inelastic effects, for example, within the framework of more accurate methods of measuring peak intensities developed by Tougaard.[78] Finally, it might be useful to consider the possibility of *nonuniform or anisotropic inelastic scattering*. Such effects have been considered in both LEED[79a] and EXAFS,[79b] where the use of complex scattering phase shifts is proposed; but the influence of such effects on predicted diffraction patterns in PD or AED has not been assessed. More recently, Treglia et al.[80a] have used SSC–SW calculations to describe very low energy photoelectron diffraction at about 30 eV from different surfaces of W. They see evidence for a significantly different inelastic attenuation length in emission from W (001) and W (110). This could well be possible, but at this low energy, it would also be useful to carry out full MS calculations to eliminate such effects as another cause of effective anisotropic attenuation. In another recent paper, Frank et al.[80b] have discussed Auger electron diffraction data from Pt(111) with various adsorbates and for energies varying from about 65 eV to 420 eV. They have analyzed these results in terms of a classical model of anisotropic inelastic attenuation which totally neglects all wave inteferences and diffraction phenomena. Unfortunately, there is no basis in prior experiment or theory for this extreme model, even though it seems to fortuitously fit some of the features in the experimental data. Thus, this classical analysis by Frank et al. provides neither a useful method for analyzing AED data, nor any new information concerning the possibility of anisotropic inelastic attenuation. Such attenuation is in any case expected to produce only small corrections to the strong anisotropies associated with diffraction effects.

3.1.8. Relationship to EXAFS/SEXAFS Theory

As a further aspect of the SSC model, we note that it can be directly reduced to an expression very close to that used in EXAFS/SEXAFS analyses if it is assumed that all scattered waves ϕ_j are small in magnitude in comparison to ϕ_0.[15] Then, if we begin at Eq. (5) (for simplicity neglecting any averaging over $\hat{\varepsilon}$), we see that all terms such as $\phi_j\phi_{j'}^*$ and $\phi_j\phi_{j'}^*$ can be neglected in expanding the absolute value squared. The thermal diffuse scattering term can also be neglected. After some

simple algebra, it can then be shown that

$$I(k) \propto (\hat{\varepsilon}\cdot\hat{k})^2 e^{-2\gamma L} + 2(\hat{\varepsilon}\cdot\hat{k})e^{-\gamma L}\sum_j \frac{\hat{\varepsilon}\cdot\hat{r}_j}{r_j}|f_j(\theta_j)|\, W_j e^{-\gamma L_j}$$
$$\times \cos[kr_j(1-\cos\theta_j)+\psi_j(\theta_j)], \quad (9)$$

and that this can be converted to a normalized function $\chi(k)$ if we take the unscattered intensity to be $I_0 = (\hat{\varepsilon}\cdot\hat{k})^2 e^{-2\gamma L}$ and finally write

$$\chi(k) = \frac{I(k) - I_0}{I_0} \propto \frac{2}{(\hat{\varepsilon}\cdot\hat{k})e^{-\gamma L}}\sum_j \frac{\hat{\varepsilon}\cdot\hat{r}_j}{r_j}|f_j(\theta_j)|\, W_j e^{-\gamma L_j}$$
$$\times \cos[kr_j(1-\cos\theta_j)+\psi_j(\theta_j)]. \quad (10)$$

This last equation thus has a form very close to the standard kinematical expression for EXAFS/SEXAFS, with the only differences being that double scattering events of the type emitter → scatterer → emitter → detector in Eq. (7) are included in the integration over direction in EXAFS to better describe the primary wave,[41] with these producing the central-atom phase shift; and the integration over direction changes the cosine function here finally to a sine function for EXAFS/SEXAFS. Equations (9) and (10) were first used in connection with the interpretation of ARPEFS data by Orders and Fadley,[15] and they have later been refined in this context by Sagurton et al.[21] Their form also suggests the possibility of using Fourier transform methods in scanned-energy PD to derive information concerning the set of path-length differences associated with a given structure, as discussed first by Hussain et al.[14] and now in active use by Shirley and co-workers[20,25] as a preliminary step of ARPEFS analysis.

As a final comment concerning this level of the diffraction theory, we consider the conservation of photoelectron flux. In the small-atom (or large r_j) limit, where PW scattering is adequate, the usual optical theorem assures that flux will be conserved if it is integrated over 4π.[81] Thus, even if high-energy scattering produces forward-scattering peaks, there will be, somewhere else, sufficient phase space with reduced intensity to exactly cancel them. However, in using the SSC–PW model for cases in which some scatterer distances require SW corrections, it is doubtful that flux will be conserved properly.[40] Nonetheless, with SW scattering correctly included, Rehr et al.[45] have shown that their SW equivalent of Eq. (7) does conserve flux and lead to a generalized optical theorem on each l channel involved.

In subsequent sections, we will consider several applications of this SSC model to the interpretation of experimental data, including especially several substrate and adsorbate systems of known geometry to test the degree of its validity.

3.2 Effects beyond Single Scattering

Finally, the possible importance of multiple scattering (MS), particularly along rows of atoms in a multilayer substrate, has been discussed qualitatively for some time,[9,42] and more recent papers have presented quantitative estimates of such effects and suggested improved methods for including MS corrections if they

are needed.[24,25,54,82-84] In general, the MS analogue of Eq. (2) can be written as

$$\psi(\mathbf{r},\mathbf{k}) = \phi_0(\mathbf{r},\mathbf{k}) + \sum_j \phi_j(\mathbf{r},\mathbf{r}_j \to \mathbf{k}) + \sum_j \sum_k \phi_{jk}(\mathbf{r},\mathbf{r}_j \to \mathbf{r}_k \to \mathbf{k})$$

$$+ \sum_j \sum_k \sum_l \phi_{jkl}(\mathbf{r},\mathbf{r}_j \to \mathbf{r}_k \to \mathbf{r}_l \to \mathbf{k})$$

$$+ \sum_j \sum_k \sum_l \sum_m \phi_{jklm}(\mathbf{r},\mathbf{r}_j \to \mathbf{r}_k \to \mathbf{r}_l \to \mathbf{r}_m \to \mathbf{k}) + \text{higher orders,}$$

$$(11)$$

where events up to fourth order are shown here and, in the multiple scattering sums, the combinations of j, k, l, and m are limited only in that they do not involve consecutive scattering by the same scatterer. Such MS calculations have been done in two basic ways: first by Tong and co-workers using LEED-type methods that require full translational symmetry along the surface,[24] and more

FIGURE 6. Calculated Auger electron diffraction patterns at 917 eV from linear chains of Cu atoms in single and multiple scattering. The geometry of the calculation with the emitter at the base of the chain is shown at the top. The primary outgoing Auger wave is treated as having s character. The multiple scattering results are shown at three levels of the matrix used to describe the scattering: (1 × 1), (3 × 3), and the most accurate, (6 × 6). The (1 × 1) and (3 × 3) cases are found to be superimposable for this case. (From Ref. 84, with similar results also appearing in Refs. 73 and 83(b).)

recently by Barton and co-workers using a cluster approach with SW scattering and the Taylor series MQNE method to simplify the calculations.[25,82,83] The cluster method is really more appropriate to the physics of such a short-range order probe, and we will term it MSC-SW. More recently, Rehr and Albers[54] have proposed a Green's-function matrix method for such MSC-SW calculations that shows promise as an alternate approach in extensive applications by Kaduwela et al.[84]

One effect of MS first discussed by Poon and Tong[24] is a defocusing of intensity occurring in multiple forward scattering at higher energies along a dense row of atoms, such that an SSC-PW or SSC-SW calculation along such a row may overestimate the intensity by a factor of two or more. This is illustrated schematically in Fig. 3b(ii). For an embedded species at some distance from the surface but again emitting along such a row, it has more recently been shown that these defocusing effects may be even more dramatic.[73,82,83]

Such defocusing effects have been very nicely illustrated in recent MSC-SW calculations by Barton, Xu, and van Hove[73,82,83] and by Kaduwela et al.[84] for emission from chains of Cu atoms of variable length. Some recent results of this type are shown in Figs. 6 and 7. In both figures, chains of 2, 3, or 5 atoms with the emitter at their base are tilted at 45° with respect to the surface of a medium of uniform density that simply serves to attenuate the emitted waves inelastically (see inset in Fig. 6). This geometry thus simulates the intensity distribution expected for emission from the 2nd, 3rd, and 5th layers along a low-index [110]
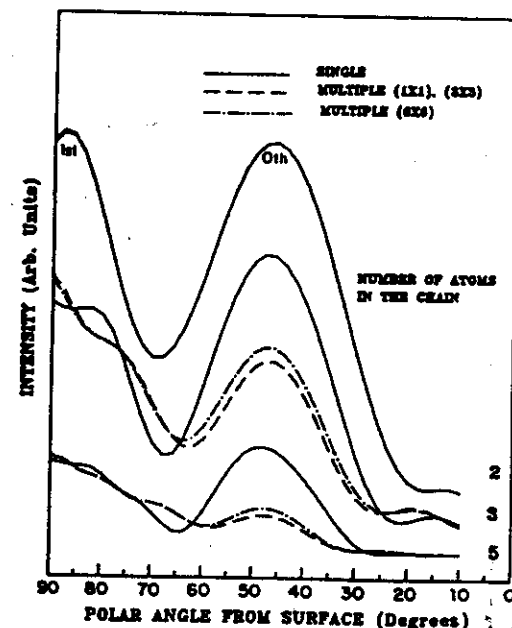

FIGURE 7. As in Fig. 6 (bottom), but for an energy of 100 eV.

row of Cu with (001) orientation, but without any diffraction effects due to scatterers adjacent to the row. Emission into a simple s-wave final state approximating Auger emission is treated. Both single-scattering and fully converged (6 × 6) multiple-scattering calculations are shown for each case.

In Fig. 6, for an emission energy of 917 eV, it is clear that the single- and multiple-scattering curves are identical for the two-atom case (as appropriate to a diatomic adsorbate, for example), but they diverge more and more as additional scatterers are added between the emitter and the detector. For the five-atom chain, the forward scattering peak is suppressed to only about 10–15% of its value for single scattering. There is also a systematic narrowing of the width of this peak as more defocussing due to multiple scattering comes into play. For scattering angles more than about ±15° from the chain axis, the differences between single and multiple scattering are much more subtle, as is to be expected since strong multiple forward scattering is no longer possible directly in the emission direction. At the much lower energy of 100 eV in Fig. 7, one expects less strongly peaked forward scattering, as shown by the wider peaks along a polar angle of 45°. Here again, the single-scattering and multiple-scattering results are identical for a two-atom chain, but one sees a suppression and narrowing of the forward scattering peak with increasing chain length that is qualitatively similar to, but less severe than, that observed at the higher energy.

Overall, these and other recently published results by Xu and van Hove[73] indicate that, for emitters in the first one or two layers of a surface and/or for which the emission direction does not involve near parallelism with a dense row of scatterers, a single scattering model should be quite accurate. For atoms further below the surface and/or for emission directions along such high-density rows, certain forward scattering features are expected to be suppressed by multiple scattering, but single-scattering calculations should nonetheless predict their positions with good accuracy.

An additional important multiple scattering effect pointed out by Barton et al.[25] is due to strong nearest-neighbor backscattering at lower energies. This they find in certain scanned-energy cases to significantly increase intensity due to events of the type emitter → neighbor → emitter → detector, as illustrated in Fig. 3b(i).

A further important point in connection with such multiple-scattering calculations is that events up to at least the fifth order have to be included to assure reasonable convergence.[25,84] In fact, it is found that including only second-order events can often lead to curves which are in much poorer agreement with experiment than the corresponding first-order calculation![84] This is similar to the experience in EXAFS theory, in which including only lower-order multiple-scattering corrections can yield worse results than those of single scattering.[57,85] A more reasonable procedure is to include events up to, say, the fifth order if the total path length $r_j + r_{jk} + r_{kl} + \cdots$ is less than some cutoff value of 10–20 Å,[20,25,57,85] although an improved cutoff criterion has been suggested by Kaduwela et al.[84]

As noted previously, there is by now a considerable body of data which indicates that useful structural information can be derived at the SSC–SW or even SSC–PW level, and we will show illustrations of this in subsequent sections. Nonetheless, MS effects such as those described above can cause discrepancies

between experiment and theory for certain classes of system, and full MS treatments of both photoelectron and Auger electron diffraction are beginning to be more often used. Several advances in the simplification of these methods, as well as rapid improvements in computer technology, should lead to a greater reliance on MS approaches in future work. In the examples which follow, a variety of theoretical models have been used, and the specific approach followed will be indicated with each set of results to permit the reader to draw his or her own conclusions.

4. ILLUSTRATIVE STUDIES OF DIFFERENT TYPES

4.1. Small-Molecule Adsorption and Orientation

We here consider primarily the case of small-molecule adsorption as studied by higher-energy XPD. The cases treated are thus of considerable interest in studies of surface chemistry and catalysis, and they provide the first simple illustrations of the utility of the forward-scattering peaks discussed in the preceding section. Auger peaks at similar energies of about 1000 eV could also in principle be used for such studies, but all of the cases to date involve photoelectron diffraction.

4.1.1. CO/Ni (001)

We begin with the first system of this type studied by Petersson et al.[23] and Orders et al.:[69] c(2 × 2) CO on Ni (001). Figure 8 compares experimental C 1s
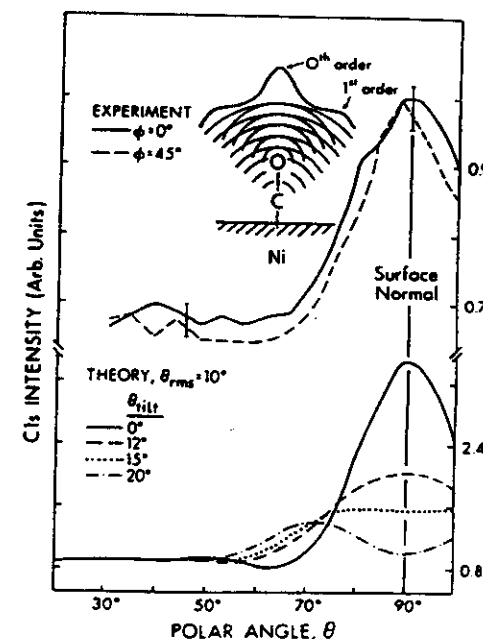

FIGURE 8. Comparison of polar-scan C 1s XPD data from c(2 × 2) CO on Ni (001) at a kinetic energy of 1202 eV with SSC-PW theory. The inset indicates the type of intramolecular forward scattering and interference involved. Note definitions of zeroth-order and first-order effects, as shown also in Figs. 4 and 5. (From Ref. 69.)

polar scans in two high-symmetry azimuths (normalized by dividing by the O 1s intensity to eliminate the θ-dependent instrument-response function) to SSC-PW calculations for varying degrees of CO tilt relative to the surface normal.[69] The theoretical model also includes a wagging or "frustrated-rotation" molecular vibration with an rms displacement of 10 Å. The experimental curves are essentially identical along both azimuths and show a strong peak along the surface normal that represents about a 35% anisotropy. Comparing experiment and theory furthermore permits concluding very conservatively that CO is within 10° of normal for this overlayer and that it has no preferential azimuthal orientation.

The inset in this figure also indicates that, in addition to the forward scattering or zeroth-order diffraction peak, one expects higher-order features such as the first-order peak indicated. (These also appear in the single-scatterer calculations of Figs. 4 and 5, where higher orders also are shown.) The first-order peak corresponds to a 2π phase difference between the direct wave and the scattered wave, or a path length difference of approximately one deBroglie wavelength. We will further consider such higher-order features in the next case and subsequent examples.

4.1.2. CO/Fe (001)

A more recent and more complex case of CO adsorption is that on Fe (001). In Figs. 9a and 9b, we show both polar and azimuthal C 1s data obtained by Saiki et al.[86] from CO adsorbed at room temperature on Fe (001) so as to form the so-called α_3 state. This rather unusual species has been the subject of prior studies by several techniques, including EELS, ESDIAD, and NEXAFS.[87] Its structure is of considerable interest because it is thought to be bound in a highly tilted geometry with a significantly weakened C-O bond and thus to be a possible intermediate state for the dissociation of the molecule. However, the best that the tilt angle could be determined from NEXAFS data was 45 ± 10°, and no information was obtained on the most likely azimuthal orientation(s) of the molecules. It is thus of interest to see what more can be learned about such a species from XPD.

The strong peak in the normalized C 1s polar-scan results for the [100] azimuth shown in Fig. 9a immediately permits a direct estimate of the tilt angle with respect to the surface normal as $\theta_{tilt} = 55 \pm 2°$ (that is, with the molecule oriented 35° from the surface). Also, the fact that this forward scattering peak is not seen in polar scans along the [1$\bar{1}$0] azimuth indicates that the preferred tilt is along $\langle 100 \rangle$ directions, or into the open sides of the fourfold-hollow sites that are the sterically most reasonable choices for the bonding location. Complementary evidence confirming this structure comes from the azimuthal data at a polar angle with respect to the surface of $\theta = 35°$ in Fig. 9b. These results again show the preferred tilt in the $\langle 100 \rangle$ azimuths via strong peaks along $\phi = 0°$ and 90°. It is thus concluded that the CO molecules are tilted along the four $\langle 100 \rangle$ axes, perhaps in separate but equally populated domains, as illustrated schematically for one fourfold-hollow site in Fig. 9c.

As a self-consistency check of these data, it is also of interest that the overall effects seen in both parts a and b of Fig. 9 are of very nearly the same magnitude.
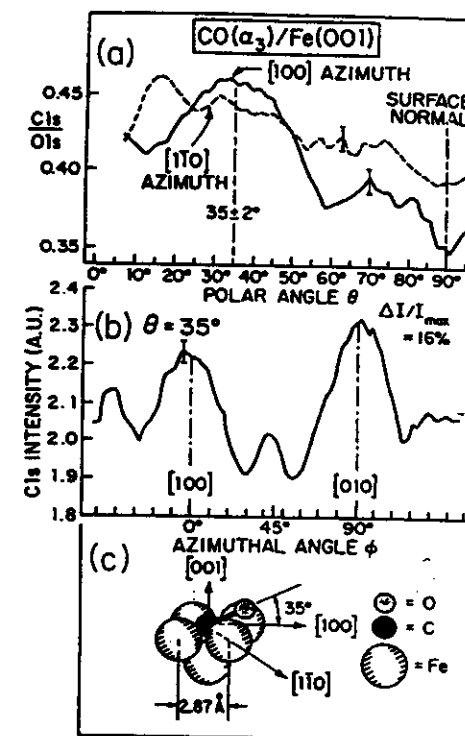
FIGURE 9. (a) Experimental polar scans of the C 1s/O 1s intensity ratio for the α_3 state of CO on Fe (100). The C 1s kinetic energy is 1202 eV. Curves are shown for two azimuths: [100] (solid curve) and [1,$\bar{1}$,0] (dashed curve). (b) Experimental azimuthal scan of C 1s intensity for the α_3 state of CO at a polar angle of 35° chosen to coincide with the peak in the [100] data of part (a). (c) The bonding geometry as deduced from these data. (From Ref. 86.)

That is, if the overall anisotropy as mentioned previously is measured as a percentage by $\Delta I/I_{max}$, we find about a 14% effect in Fig. 9a and a 16% effect in Fig. 9b. Thus, it is possible to reliably measure rather small diffraction effects with XPD, particularly in the azimuthal data, which do not need to be corrected for any systematic instrumental changes in intensity. By contrast, polar scans will always be influenced by a θ-dependent instrument-response function[9] and must somehow be corrected for this. Since the O 1s intensity is not expected to be very much affected by final-state scattering and diffraction, using the C 1s/O 1s ratio in Fig. 9a acts to normalize out any such instrumental effects.

Another useful observation from Figs. 9a and b is that the main peaks exhibit very similar full widths at half-maximum intensity (FWHM) of 30-35°. Thus, the resolutions for determining both the polar and the azimuthal senses of the tilt are about the same.

The results in Fig. 9b also exhibit much smaller but quite reproducible peaks along the $\langle 110 \rangle$ azimuths (that is, at $\phi = 45°$) that could be due to scattering from Fe atoms in the $\langle 110 \rangle$ corners of the hollow. A more detailed theoretical analysis of these azimuthal results using the SSC-SW model in fact shows that these peaks are due to constructive addition of first-order scattering from oxygen
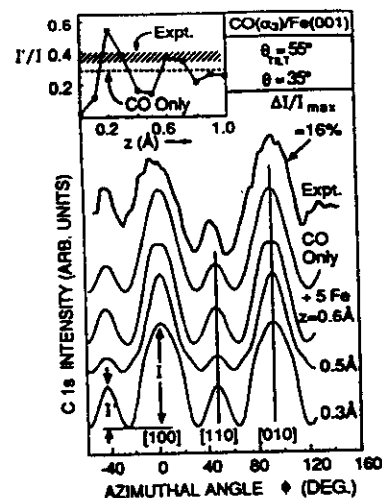
FIGURE 10. Experimental results of Fig. 9(b) are compared with theoretical SSC-SW calculations of C 1s azimuthal scans for CO on Fe (001) tilted at 35° with respect to the surface along the (100) directions and assumed to be in four equally populated domains. In the top theoretical curve, no Fe scatterers are included. In the lower theoretical curves, five Fe scatterers are added, as in Fig. 9(c). The C atom is centered in the fourfold hollow, and the distance z with respect to the Fe surface plane is varied. The inset shows the ratio of the two main peak intensities I'/I as a function of z. (From Ref. 86.)

(see inset in Fig. 8) and second- or third-order scattering from the corner Fe atoms, depending upon the distance z of the tilted CO from the Fe surface. Some results of these calculations of the azimuthal scan of Fig. 9b are compared to experiment in Fig. 10. The top theoretical curve is from a calculation in which only CO molecules are present; these are assumed to be present in four equally populated domains tilted at $\theta = 35°$. This very simple calculation correctly predicts the positions and approximate widths of the strong forward scattering peaks along $\langle 100 \rangle$ azimuths, as well as the additional weaker first-order features seen along $\langle 110 \rangle$ at $\theta = 45°$. However, if the five Fe nearest neighbors are also included as scatterers (as shown in Fig. 9c) and the C atom is further assumed to be centered in the fourfold hollow but with variable vertical distance z relative to the first Fe layer, we arrive at what should be a more realistic set of curves. These are striking in that the small peaks along $\langle 110 \rangle$ are predicted to oscillate in intensity, as shown in the figure inset. Comparing experiment and theory for the intensity, as indicated yields z values of both about 0.22 ± 0.10 Å and ratio I'/I as indicated yields z values of both about 0.22 ± 0.10 Å and 0.63 ± 0.10 Å that agree best; these z values also correspond to very reasonable C–Fe distances of 1.6–2.0 Å. Multiple-scattering calculations for this system by Kaduwela et al.[84] also quantitatively confirm the single-scattering results shown here; this is as expected in view of the high energy and high takeoff angles relative to the surface.

Figure 11 shows a further aspect of this analysis in which the experimental polar scans of Fig. 9a are compared to SSC–SW theory for the two azimuths involved and for several z distances. Polar scans are also seen to be sensitive to both azimuth and vertical distance, with in particular the results for the [110] azimuth favoring a z value nearer 0.3 Å. This study thus indicates the significant advantage of having both polar and azimuthal XPD data for such systems.

The theoretical anisotropies $\Delta I/I_{max}$ in Figs. 8, 10, and 11 are found to be about 2–3 times larger than those of experiment. This kind of discrepancy has

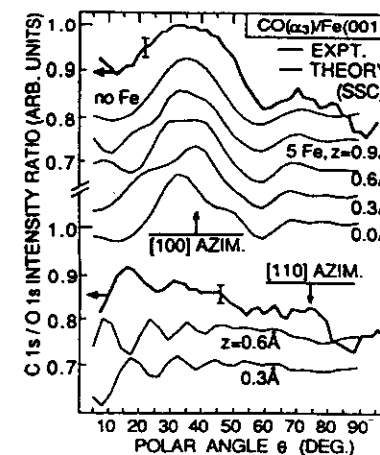FIGURE 11. Comparison of experimental C 1s polar scans for α_3 CO on Fe (001) to SSC-SW theory for two azimuths and different vertical distances z. (From Ref. 86.)

been found in most previous XPD studies of adsorbates[9,10,23,69] and can be explained by the combined effects of the following:

- Molecular vibration. This has not been included in the calculations for CO/Fe (001) shown here, but is considered in prior work for CO/Ni (001).[23,69]
- The presence of more than one type of emitter on the surface. For the present case, this could be due either to the method of formation of the α_3 state or to adsorption at defects. There could also be additional C-containing impurities beyond those associated with CO and its dissociation products on the surface. All of these act to diminish diffraction features relative to background and thus to reduce the experimental anisotropy. Such effects will tend to be present in any adsorbate system to some degree.

4.1.3. CO/Ni (110)

A final example of a molecular adsorbate system is that of CO on Ni (110), as studied with polar-scan measurements by Wesner, Coenen, and Bonzel.[76,88] For this case, Fig. 12 shows a comparison of normalized C 1s polar scans from CO adsorbed to saturation on Ni (110) at two different temperatures of 300 K and 120 K. The polar scans are markedly different, with the high-temperature results being very similar to those of CO on Ni (001) (cf. Fig. 8), and thus suggestive of a simple vertical adsorption of the CO, and the low-temperature results being widely split into a doublet along the [001] azimuth, but retaining a weaker peak along the normal for the [1$\bar{1}$0] azimuth. The low-tempeature, higher-coverage results have been explained by a structure in which the CO molecules are tilted by $\pm 21°$ along the [001] azimuth, as shown in Fig. 12d.[89] This structure is nicely confirmed in Fig. 12c, where SSC-PW calculations with an rms vibrational amplitude of 8° are found to yield excellent agreement with experiment.

Wesner et al.[88] have also considered the effect of adsorbing CO on a Ni (110)
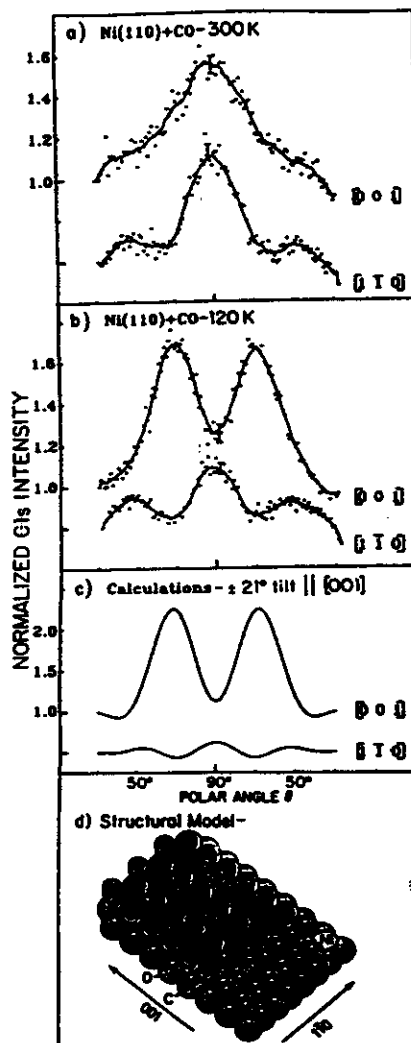
FIGURE 12. (a) Experimental polar scans in two azimuths of the C 1s intensity from CO adsorbed on Ni (110) at 300 K. The kinetic energy is 970 eV. (b) As in (a), but for adsorption at 120 K. (c) SSC-PW calculations modeling the data in (b), with an assumed tilt of ±21° along [001] and an rms vibrational amplitude of 8°. (d) The geometric model assumed for the calculations of (c). [(a)–(c) from Ref. 88, (d) from Ref. 89.]

surface pretreated with K, which is known to act as a promoter in many catalytic reactions. This system is found to have both vertical and more highly tilted CO species present. Finally, the same group has made use of the temperature dependence of the widths of peaks such as those in Fig. 12 for CO on Ni (011) to study the anisotropy of wagging vibrational amplitudes in different azimuths.[76]

4.1.4. Other Systems and Other Techniques

These simple examples thus show that XPD (or in principle also higher energy AED) is a very powerful tool for studying the orientations and bonding of small molecules on surfaces, and that it is well suited to even very highly tilted species that may exhibit enhanced reactivity and thus be important in such phenomena as catalysis. Each of the cases discussed here is also significant in that other surface structural probes have been applied to the same problem without being capable of a clean resolution of the structure. Similar XPD measurements and theoretical analyses have also recently been applied to several other systems: CO and CH$_3$O on Cu (110) by Prince et al.[90] and CO on Pt (111) treated with K as a promoter by Wesner et al.[91]

Similar forward-scattering effects have also been seen by Thompson and Fadley[92] in emission from an atomic adsorbate on stepped surfaces: oxygen on Cu (410) and Cu (211). For this case, scattering by near-neighbor atoms up the step face from the emitter is found to be particularly strong. Stepped surfaces in fact represent a particularly attractive kind of system for study by this technique, since any atomic or molecular adsorbate that bonds preferentially at the base of the step has atoms on the step face as nearest-neighbor forward scatterers in the upstep direction.

The use of intramolecular forward scattering also appears to have several advantages for determining molecular or fragment orientations on surfaces in comparison to other techniques such as high-resolution electron energy loss spectroscopy (EELS),[93] electron stimulated desorption-ion angular distributions (ESDIAD),[94] and NEXAFS[95] or SEXAFS.[16] In EELS, the presence of a titled species can be detected by which vibrational modes are excited, but estimating the magnitude of the tilt is difficult.[67a,93] In ESDIAD, the ion angular distributions for bond tilts away from normal can be significantly distorted by image forces and ion-neutralization effects,[87b,94] and tilts further away from normal than 25–30° therefore cannot in practice be measured accurately, if at all. In NEXAFS[95] and SEXAFS,[16] the experimental intensities of different features vary only relatively slowly with polarization, as sin$^2 \alpha$ or cos$^2 \alpha$, if α is the angle between the radiation polarization and the appropriate molecular symmetry axis. In forward-scattering XPD or AED, by contrast, it is the much narrower peak in the scattering amplitude $|f|$ near 0° (cf. Fig. 2 and Fig. 8) that controls the precision of orientation determinations, leading to FMWHs of 25–35° for all molecules studied to date. Comparing these values to the effective widths of sin$^2 \alpha$ or cos$^2 \alpha$ thus leads to the conclusion that forward scattering in XPD or AED should be about 3–4 times more precise in determining bond directions. An additional problem in NEXAFS is that a correct assignment of the peak(s) to be studied is necessary.

We close this section by noting that scanned-energy photoelectron diffraction or ARPEFS also has been applied recently to the study of small-molecule fragments such as formate (HCOO) and methoxy (CH$_3$O) adsorbed on Cu (100). The lower energies involved in this work imply that information on bond distances to backscattering neighbors below the adsorbate are also derivable. Such studies are described in more detail in the chapter by Haase and Bradshaw in Volume 2 of this set.

4.2. Atomic Adsorption and the Oxidation of Metals

4.2.1. Oxygen/Ni (001)

Saiki and co-workers[26] have carried out an XPD/LEED investigation of the interaction of oxygen with Ni (001) over the broad exposure range from $c(2 \times 2)$ O at 30 Langmuirs (L) to saturated oxide at 1200 L. Scanned-angle measurements were performed with Al $K\alpha$ radiation at 1486.6 eV for excitation. Although this system has been extensively studied in the past by various structural and spectroscopic probes,[96-98] several questions remain as to the exact structures formed. The combined use of XPD and LEED proves capable of answering several of these, as well as pointing out some new features of XPD that should be generally useful in surface-structure studies.

For example, in Fig. 13a, we show azimuthal scans of O $1s$ intensity at a relatively high polar angle θ of 46° with respect to the surface for four oxygen exposures from the onset of sharp $c(2 \times 2)$ LEED spots (30 L) to full oxide saturation (1200 L). The experimental curves are compared to SSC–SW calculations for a $c(2 \times 2)$ overlayer in simple fourfold sites with a vertical oxygen distance of $z = 0.85$ Å above the first Ni layer (the by now generally accepted structure), for two monolayers (ML) of NiO (001) with ideal long-range order, and for two monolayers of NiO (111) with long-range order. The dominant peaks at $\phi = 0°$ and 90° for the highest two exposures of 150 L and 1200 L are correctly predicted by theory and are due to simple forward scattering of photoelectrons emitted from oxygen atoms below the surface by oxygen atoms situated in the upper layers of the oxide, as indicated by the arrows in Fig. 13b. These peaks furthermore persist as the strongest features down to 30 L, indicating very clearly the existence of buried oxygen emitters, probably in small nuclei of NiO (001), over the full region of observation of the $c(2 \times 2)$ overlayer. The presence of such oxide nuclei in varying degrees on Ni (001) surfaces prepared in different laboratories is thus a likely cause of some of the previous controversy surrounding the vertical positions of both $c(2 \times 2)$ and $p(2 \times 2)$ oxygen on this surface,[96,77] but XPD provides a sensitive probe of the presence of any sort of buried species via such forward-scattering effects.

Comparing the 1200-L experimental curve and the theoretical curve for 2 ML of ideal Ni (001) in Fig. 13a for the region near $\phi = 45°$ shows qualitative agreement as to the existence of a region of enhanced intensity for $30° < \phi < 60°$, but disagreement as to exact fine structure, with theory showing a doublet where experiment shows a single broad peak. However, annealing this saturated oxide to approximately 250 °C for ~10 minutes to increase its degree of long-range order parallel to the surface (as well as perhaps its thickness)[77] is found to yield a significantly altered XPD curve, with a doublet centered at $\phi = 45°$ that is in very good agreement with theory for NiO (001), as shown in the higher-resolution results of Fig. 14. It is also striking that the annealed oxide overlayer shows much more fine structure and generally narrower features, even though the dominant peaks in both the unannealed and annealed data are still those for simple forward scattering along $\langle 101 \rangle$ directions (i.e., at $\phi = 0°$ and 90°). The theoretical curves for 2 ML or 3 ML of ideal NiO (001) in Fig. 14 are
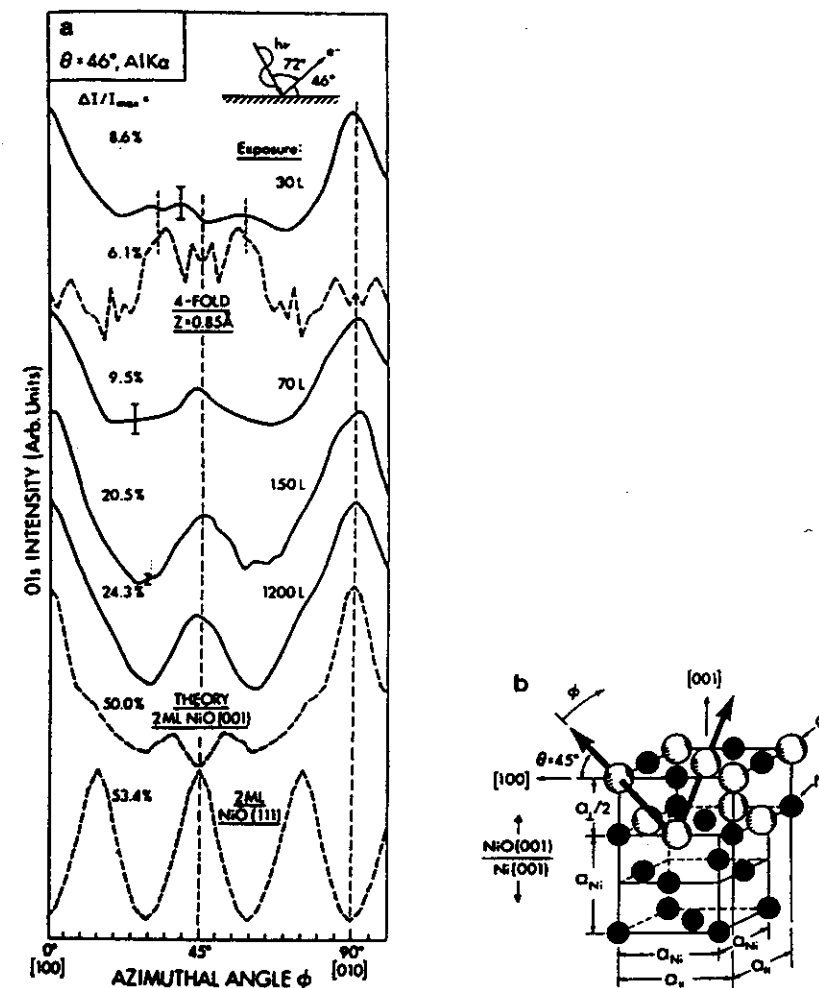
FIGURE 13. (a) O $1s$ azimuthal XPD data from oxygen on Ni (001) at four exposures from the $c(2 \times 2)$ regime (30 L) to saturated oxide (1200 L). The kinetic energy is 945 eV. The polar angle of 46° involves scanning very close to the (110) directions at $\theta = 45°$ and $\phi = 0°$ and 90°. Also shown are SSC–SW calculations for fourfold $c(2 \times 2)$ oxygen at $z = 0.85$ Å and fully ordered 2 ML overlayers of NiO with both (001) and (111) orientations. (b) An approximate representation of the structure of the dominant Ni (001) formed at high exposures, indicating the oxide lattice expansion and strain involved. Also shown as arrows are the directions of the strong forward-scattering peaks observed at $\phi = 0°$, 90° in (a). (From Ref. 26.)
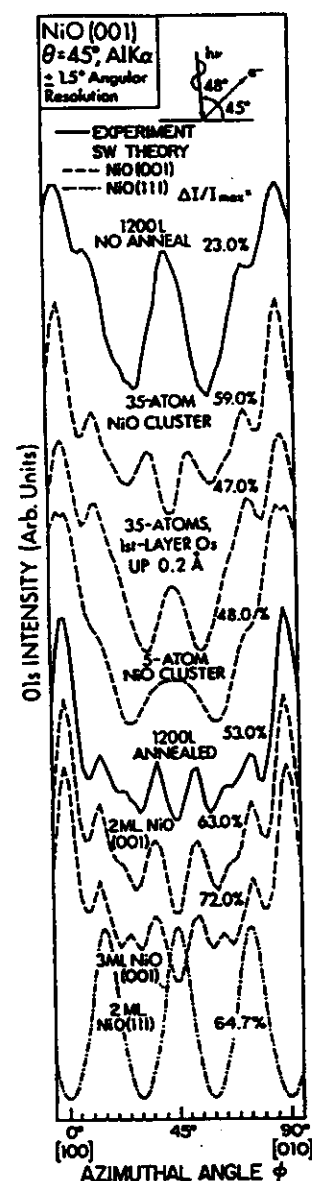
FIGURE 14. O 1s azimuthal XPD data from the saturated oxide formed at 1200 L exposure on Ni (001) obtained at a high angular resolution of ±1.5° with an emission angle of 45° with respect to the surface. Experimental curves are shown for both the ambient-temperature oxide and the same overlayer after a brief low-temperature anneal. SSC-SW calculations are also shown for several cases: smaller five-atom and 35-atom clusters to simulate loss of long-range order and strain and large fully converged clusters to simulate ideal NiO growing in either the (001) orientation (with 2 ML or 3 ML thickness) or the (111) orientation (with 2 ML thickness). (From Ref. 26.)

also in remarkably good agreement with the annealed data, verifying that annealing has produced a very highly ordered overlayer, and suggesting that the unannealed oxide exhibits diffraction effects due to strain and disorder.

The data shown in Fig. 14 are different from all results presented up to this point in being obtained at a very high angular resolution of ±1.5° or less; precise angular resolution has in this case been obtained by using interchangeable tube arrays of the proper length-to-diameter ratio, as discussed in detail by White et al.[33] Note the additional fine structure in the unannealed 1200-L curve of Fig. 14 as compared to that of Fig. 13a.

The bottom theoretical curves in Figs. 13a and 14 are for 2 ML of NiO (111), an orientation of oxide growth which is also thought from LEED to coexist with NiO (001) on this surface.[97] The total lack of agreement of the NiO (111) curve with experiment makes it clear that this is only a minority species affecting no more than 5% of the NiO present.

In order to better understand the unannealed oxide data in Figs. 13a and 14, we also show in Fig. 14 theoretical curves for smaller 35-atom and 5-atom clusters of NiO (001). The previous calculations discussed involved much larger clusters with about 100 atoms per layer to insure full convergence. The 35-atom cluster includes atoms in about the first 1½ unit cells around a given oxygen emitter; the 5-atom cluster is minimal and represents only nearest-neighbor and next-nearest-neighbor scatterers. The results for the full 2-ML cluster and the 35-atom cluster are found to be very close except for somewhat more fine structure in the full-cluster curve. This is consistent with prior XPD studies which have concluded that near-neighbor scatterers dominate in producing the observed patterns. However, much better agreement with the unannealed oxide results is seen if either the first-layer oxygen atoms (but not the nickel atoms) in the 35-atom cluster are relaxed upward by 0.2 Å or the effective cluster size is reduced to five atoms. Both of these models are consistent with a highly strained unannealed oxide overlayer of (001) orientation in which the long-range order is severely disturbed. The LEED spots for NiO (001) in fact indicate a lattice expanded by very nearly ¼ relative to the underlying Ni (001) surface, as indicated schematically in Fig. 13b. Although these results do not permit choosing between these two possibilities for stress relief in such a disordered system, they are significant in that both the experimental and theoretical XPD curves are quite sensitive to these more subtle deviations from an ideal NiO (001) overlayer with long-range order. This suggests a broad range of applications of XPD or higher-energy AED to studies of epitaxy and overlayer growth.

It is also significant in the comparisons of experimental data for annealed oxide with theory for 2-3 ML of NiO (001) in Fig. 14 that the agreement extends even to the overall degree of anisotropy, as judged again by $\Delta I/I_{max}$. The theoretical anisotropies are only about 1.2–1.3 times those of experiment. As noted previously, theory is in general expected to overestimate these anisotropies, in some previous cases by as much as factors of 2–3. One important reason for this kind of discrepancy is the lack of allowance in the calculations for atoms bound at various defect or impurity sites along or below the surface, as these are expected to produce a rather diffuse background of intensity, thus lowering the overall anisotropy. However, for the present case, the very good

agreement suggests that the annealed oxide overlayer consists of oxygen atoms that are almost completely bound in a highly ordered NiO (001) structure.

At lower exposures, XPD has also been used to determine the $c(2 \times 2)$ oxygen structure on Ni (001).[26] The high θ values of Figs. 13 and 14 minimize the effects of any forward-scattering events in emission from oxygen in the $c(2 \times 2)$ overlayer (cf. Fig. 2), so that the 30-L curves here are dominated by the
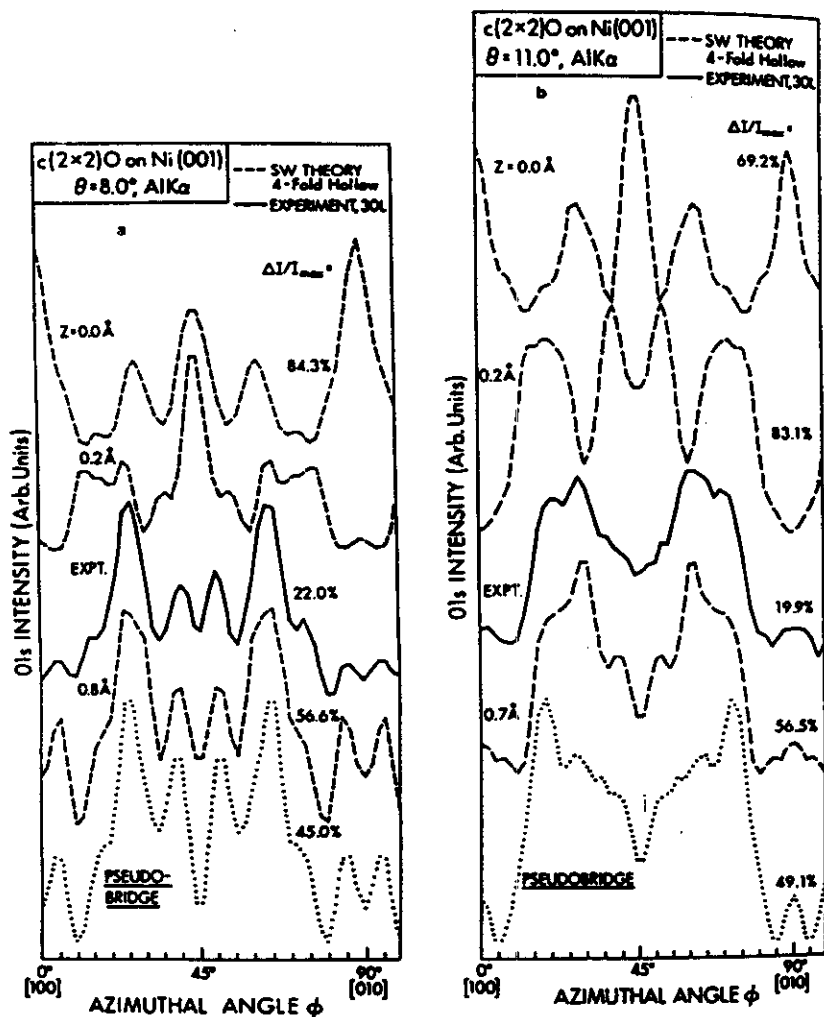
presence of a certain fraction of buried oxygen, probably in oxide nuclei. However, at very low takeoff angles with respect to the surface of approximately $8°-15°$, forward elastic scattering from adsorbed oxygen becomes much stronger, and the signal from buried oxygen is also suppressed by enhanced inelastic scattering.[9] Thus, the diffraction patterns at such low θ values are expected to be more strongly associated with overlayer effects.

Figure 15 shows such experimental and theoretical results for two representative θ values, $8°$ and $11,°$ of the four angles studied (data were also obtained for $14°$ and $17°$). Experiment is here compared with SSC–SW theoretical curves for four possible $c(2 \times 2)$ structures: in-plane fourfold bonding ($z = 0.0$ Å); slightly-above-plane fourfold bonding ($z = 0.2$ Å); the vertical distance in fourfold bonding yielding the empirical best fit to experiment at that θ value as judged both visually and by R factors;[26d] and the so-called pseudobridge geometry suggested by Demuth et al. on the basis of a LEED analysis.[98] For this last geometry, $z = 0.8$ Å and the oxygen atoms are offset horizontally by 0.3 Å in the fourfold hollow toward any of the four symmetry-equivalent $\langle 110 \rangle$ directions.

In Fig. 15a for $\theta = 8°$, it is very clear that $c(2 \times 2)$ oxygen does not occupy a position in the 0.0-to-0.2-Å range, although certain prior studies have suggested this as the most likely bonding position.[96,97] Simple fourfold bonding at $z = 0.80$ Å, by contrast, yields excellent agreement with experiment, with all observed features being present in the theoretical curve. The only points of disagreement are the relative intensity of the weak doublets centered at $\phi = 0°$ and $90°$, which is too strong in theory; and the degree of anisotropy $\Delta I / I_{max}$, which is predicted to be too high by approximately a factor of 2.6. The latter discrepancy could be due to a significant fraction of oxygen atoms occupying defect or buried sites, e.g., in the oxide nuclei mentioned previously. Also, for such a low takeoff angle that begins to be within the forward scattering cone at this kinetic energy (≈ 954 eV), there may be some defocusing and reduction of peak heights due to multiple scattering effects; in fact, $\phi = 0°$ and $90°$ are the directions of nearest-neighbor oxygen scatterers in the $c(2 \times 2)$ structure, as shown in Fig. 16a. The pseudobridge geometry does not fit experiment as well, since the relative intensity of the doublet centered at $\phi = 45°$ is too high.

In Fig. 15b, for $\theta = 11°$, the two geometries close to being in plane again do not agree at all with experiment, which is very well described by simple fourfold bonding at an optimum z of 0.70 Å. The pseudobridge geometry in this case also differs considerably from experiment as to the shape of the two main peaks. When these results are combined with those at the other two θ values studied,[26] it can overall be concluded that $c(2 \times 2)$ oxygen does not bond in either simple fourfold positions at $0.0 < z < 0.3$ Å or in the pseudobridge geometry, but does occupy simple fourfold positions at $z = 0.80 \pm 0.10$ Å. This choice of structure is also confirmed by an R-factor comparison of experiment and various theoretical curves. The z distance found here also agrees very well with several more recent structural studies of this system.[96,97]

A final point in connection with the results of Fig. 15 is that, in order for theory to adequately reflect all of the fine structure seen in experiment, the cluster used in the calculations must include all O and Ni atoms within the first few layers of the surface (adsorbate plus two layers of Ni) and out to a relatively

FIGURE 15. (a) Grazing-emission O 1s azimuthal data from $c(2 \times 2)$ O on Ni (001) at $\theta = 8°$. The experimental data are compared to SSC-SW curves for four possible fourfold-hollow $c(2 \times 2)$ structures, including the pseudobridge geometry of Ref. 98. (b) As in (a), but for $\theta = 11°$. (From Ref. 26.)

large radius of about 20 Å from the emitter. The rate of convergence with cluster size is illustrated in Fig. 16. Due to the rotational symmetry of the surface, calculations need be performed only over the 45° wedge indicated in Fig. 16a, but it is important to include sufficient atoms at the edge of this wedge. It is clear from the diffraction curves in Fig. 16b that going out to only 10 Å in radius does not yield the correct diffraction fine structure. This indicates sensitivity in forward scattering at grazing emission to well beyond the first 3–5 spheres of neighbors. The effective *diameter* of the cluster is thus about 40 Å.

Thus, these results for a prototypical surface oxidation over a broad exposure range, from ordered overlayers at partial monolayer coverage to saturated oxide, indicate several very useful types of structural information that can be derived from XPD (or by implication also by high-energy AED) in conjunction with SSC calculations.

FIGURE 16. (a) Choice of cluster. Different-sized clusters used in testing the convergence of the SSC-SW curves for $\theta = 8°$ in Fig. 15(a), labelled with the approximate radii outward from the emitter that they represent. (b) Convergence with cluster size. Calculated curves for the clusters of (a) with $z = 0.8$ Å are compared to experiment. Note that a radius of at least 20 Å is required to yield optimum agreement. (From Ref. 26.)

4.2.2. Sulfur/Ni (001)

The sulfur/Ni (001) system has been much used as a test case for surface-structure techniques because it represents a rather unique example of a system for which there is a general consensus on a structure: the $c(2 \times 2)$ sulfur overlayer is bound with atomic S in fourfold sites at a distance z of 1.3–1.4 Å above the first Ni plane.[99] Several photoelectron diffraction studies have been made of this system,[14,15,19,21,25,99] including both scanned-angle and scanned-energy measurements, and we will consider a few of these.

Higher-energy scanned-angle XPD measurements have been made for this system by Connelly *et al.* (Fig. 44 in Ref. 9), and experimental azimuthal scans of S 2*p* emission at grazing takeoff angles are found to be in good agreement with SSC-PW calculations for the known structure. However, for a structure with this high a distance above the Ni surface, the effects of forward scattering become weaker, since the scattering angle from any near-neighbor Ni atom becomes larger. For example, for the Ni nearest neighbors in the fourfold hollow, a very low emission angle of 5° with respect to the surface still corresponds to a minimum scattering angle of approximately 43° that is well outside of the forward scattering cone at high energy (cf. Fig. 2). Thus, the strongest contribution to azimuthal anisotropy is scattering from the other (coplanar) S adsorbate atoms, for which the scattering angle is simply the emission angle with respect to the surface. The sensitivity of such XPD measurements to the vertical S–Ni distance is thus expected to be lower than for more nearly in-plane or below-plane adsorption, and it has been questioned as to whether such measurements will be sensitive enough to determine structures for any adsorbate sitting well above the surface.[9] Several possibilities appear to exist for improving the positional sensitivity for such cases: working at higher angular resolutions and taking advantage of additional diffraction fine structure, using lower energies for which large-angle and backscattering are stronger, and/or using special polarization geometries to enhance certain substrate scatterers. Some of these possibilities thus involve synchrotron radiation, and we consider now their application to the S/Ni case in both the scanned-angle and scanned-energy modes.

We first look at the influence of higher angular resolution. S 2*p* azimuthal XPD data at a polar angle of 13° obtained by Saiki *et al.*[100] with a high angular resolution of about ±1.0° are shown in Fig. 17. The data were obtained in scans over 100° in ϕ and then mirror-averaged across [110] to improve statistical accuracy, but all of the features shown were reproduced in the full scan. These results exhibit considerably more fine structure than similar data obtained with a ±3.0° resolution, and the anisotropy is found to go up from 31% to a very high 40% with increased resolution. Also, when these data are compared with the SSC-SW curves shown in this figure for different z positions of S above the fourfold hollow, they exhibit a high sensitivity to position. A more quantitative analysis of these high-resolution results by Saiki *et al.*[100] using R factors for comparing experiment and theory[264] in fact yields a z value of 1.39 Å for this structure that is in excellent agreement with prior work. This analysis furthermore permits estimating the first nickel–nickel interplanar distance (d_{12}), which is found to be expanded to about 1.86 Å from the bulk value of 1.76 Å. Thus, there
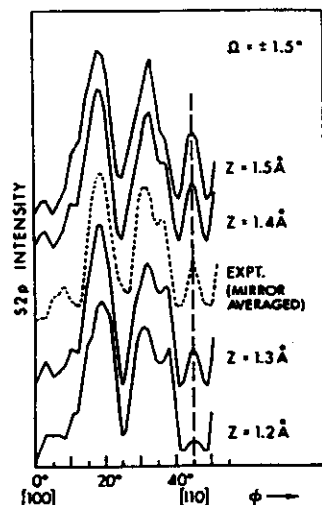
FIGURE 17. Azimuthal XPD data for S 2p emission from c(2 × 2) S on Ni (001) at a kinetic energy of 1085 eV obtained with a high angular resolution of approximately ±1.5°. The polar angle is 13° with respect to the surface. The anisotropy $\Delta I/I_{max}$ is a high 40% for these results, compared to only 31% for the same measurement with a ±3.0° angular resolution; the fine structure is also considerably enhanced with higher resolution. SSC-SW calculations are shown for various distances z of the S above the Ni surface. (From Ref. 100.)

is considerable potential in using high-energy measurements with high angular resolution, even for adsorption at large z distances above approximately 1.0Å.

Going to lower energies with synchrotron radiation in such azimuthal measurements also has potential for such studies. We show in Fig. 18 results for S 1s emission from the c(2 × 2)S overlayer on Ni (001) obtained by Orders et al.[19b] Here, the experimental geometry was chosen so that the polarization vector
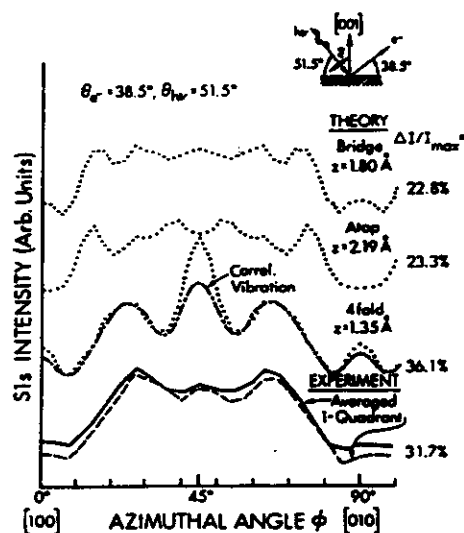

FIGURE 18. Synchrotron radiation excited S 1s intensity from c(2 × 2) S on Ni (001) at a kinetic energy of 282 eV. The geometry chosen emphasized nearest-neighbor backscattering because the polarization vector was oriented directly toward the relevant Ni nearest neighbor, as shown in the inset at upper right. SSC-PW calculations for three possible adsorption sites of bridge, atop, and fourfold are shown as dotted curves. The dashed-dotted fourfold curve involves a more correct inclusion of correlated vibrational effects. (From Refs. 19(b) and 101.)

was directed rather precisely toward nearest-neighbor Ni atoms for certain azimuthal positions in a ϕ scan. Backscattering from this type of Ni atom should also be rather strong at the photoelectron energy of 282 eV chosen (cf. Fig. 2). This energy is nonetheless high enough that a single-scattering model should still be reasonably quantitative. The experimental data is here compared with SSC-PW calculations for three different bonding sites (bridge, atop, and fourfold) with reasonable S-Ni bond distances, and the correct fourfold site is clearly in better agreement with experiment. The agreement is also significantly improved if a more accurate allowance for correlated vibrations is included in the SSC calculations, as shown by the dashed-dotted curve.[101]

However, a note of caution is in order concerning the use of different polarization orientations, since experimental and theoretical work on S/Ni by Sinkovic et al.[19a] indicates that a geometry in which the polarization is nearly perpendicular to the electron emission direction (instead of parallel, as in Fig. 18) increases the importance of multiple-scattering events and causes more significant deviations from a simple theoretical model. This is thought to occur through a weakening of that portion of the photoelectron wave emitted directly in the detection direction in comparison to the various scattered waves that can interfere with it. The intensity distribution is thus produced by the interference of direct and scattered waves that are all of the same magnitude, a situation rather like that in LEED where all contributions to intensity are those due to relatively weak backscattering; thus, MS effects might be expected to be more important. In most photoelectron and Auger experiments, the direct-wave amplitudes are stronger than those of the scattered waves, and it can be argued that this is a fundamental reason for the higher degree of applicability of a single-scattering approach.

Finally, we consider scanned-energy or ARPEFS measurements on S/Ni (001) of the type pioneered by Shirley and co-workers.[8,25] In this type of experiment, an adsorbate core intensity is measured as a function of $h\nu$ in a fixed θ, ϕ geometry, and the resulting EXAFS-like oscillations are analyzed in order to derive the adsorbate position. The data are usually analyzed as a normalized $\chi(E)$ or $\chi(k)$ function. Figure 19 shows typical experimental data of this type in a normal-emission geometry, for S 1s emission from c(2 × 2) S/Ni (001).[8] Allowance has been made here for the interference between the S Auger peak at 155-160 eV and the S 1s photoelectron peak. These results are compared to both MSC-SW calculations by Barton and Shirley[25] in Fig. 19a and SSC-SW calculations by Sagurton et al.[21] in Fig. 19b. The agreement is very good for both sets of theoretical curves, provided that the first nickel-nickel interlayer distance (d_{12}) is relaxed outward from the bulk value of 1.76 Å to 1.84 Å (cf. the two theory curves in Fig. 19b). This interlayer relaxation, as first pointed out by Barton and Shirley, thus illustrates the high sensitivity of photoelectron diffraction to subtle structural changes on the order of 0.10 Å or less.

It is also clear from this figure and other work on the S/Ni system[21,22] that both the single-scattering and multiple-scattering approaches describe the experimental results well and that they also lead to very similar structural conclusions, with only the perpendicular distance for S being different by 0.05 Å between the two analyses. Thus, although the MSC-SW approach is certainly in principle more accurate and does lead to $\chi(k)$ amplitudes in better agreement
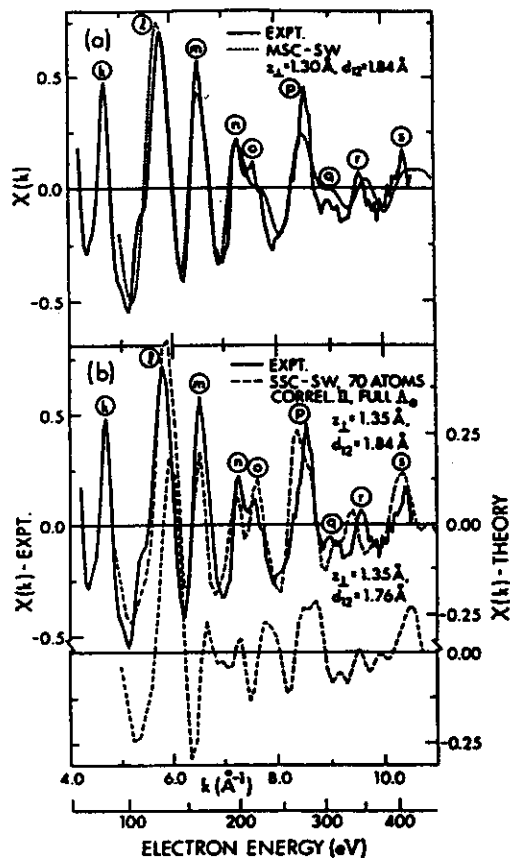
FIGURE 19. Comparison of scanned-energy S 1s data for c(2 × 2) S on Ni (001), θ_{e-} = 70°, θ_{g-} = 0° (From Ref. 8) with: (a) a multiple-scattering cluster spherical-wave (MSC-SW) calculation due to Barton and Shirley (From Ref. 25), and (b) single-scattering cluster spherical wave (SSC-SW) calculations due to Sagurton et al. (From Ref. 21). Both the sulfur vertical distance z and the first Ni–Ni interplanar distance d_{12} are specified. (Fig. from Ref. 21.)

with experiment, the SSC–SW method appears capable of a usefully quantitative description of the observed oscillations and fine structure.

Another aspect of this analysis noted by Barton and Shirley[25] is that nearest-neighbor backscattering followed by emitter forward scattering (cf. Fig. 3b–i) can be an important factor in producing the full amplitude of the ARPEFS oscillations at low energies. This may be the reason why the single-scattering curves in Fig. 19b have lower amplitudes, although a different allowance for vibrational effects also could play a role.[21]

An additional useful aspect of such ARPEFS data is in being able to Fourier transform $\chi(k)$ curves to yield peaks which are for some (but not necessarily all) of the strongest scatterers rather directly related to interatomic distances via the path-length difference and the scattering angle [cf. Eq. (10)]. The degree to which Fourier transforms can be used in this way is discussed in detail elsewhere.[21,25] However, ARPEFS Fourier transforms (FTs) need not be as simply associated with certain spheres of neighbors as are those of EXAFS and SEXAFS; the reason for this

is the potentially large number of scattering events and various possible scattering angles that can be associated with a given region in the transform.[21] Nonetheless, such FTs have been used to rule out certain structures as part of a more detailed structure determination; we consider such an example in the next section.

4.2.3. Sulfur/Cr (001)

We now turn to a recent study of c(2 × 2) S/Cr (001) by Terminello et al.[20] that serves to represent a state-of-the-art analysis of scanned-energy or ARPEFS data. In this work, S 1s intensities were scanned as a function of energy up to about 475 eV above threshold; two different emission directions were studied; [001] and [011], with polarizations oriented in general along the emission direction (35° off normal toward [011] for [001] emission and along [011] for [011] emission). Special care was taken to avoid spurious energy-dependent effects in the measuring of intensities, with normalization being needed for both the incident photon flux and the transmission function of the electron-energy analyzer. As for S/Ni (001), the interference between the S Auger peak at 155–160 eV and the S 1s photoelectron peak was allowed for by carefully subtracting out the former. Fourier transforms of the data were made, with the inner potential being treated as an adjustable parameter and the $\chi(k)$ data being multiplied by a Gaussian window function to reduce ringing effects in the final FTs. The strongest peaks in these transforms were then taken to be semiquantitatively indicative of certain near-neighbor path-length differences; this analysis thus implicitly assumes that the single-scattering Eq. (10) represents a good first-order description of the diffraction and that there are no significant interferences between the effects of different near-neighbor scatterers. The approximate geometric information from the FT peak positions was found to point to the fourfold-hollow site as the adsorption position.

The final quantitative determination of the site type and the structure was made by directly comparing the experimental $\chi(k)$ curves (Fourier filtered to remove effects due to path-length differences beyond about 20 Å) with multiple-scattering cluster calculations using spherical-wave scattering. As one example of these results, Fig. 20a compares experimental curves along the two directions with curves calculated for S adsorbed on three types of sites. It is very clear here that the fit is best for the fourfold site (cf. similar comparison for the scanned-angle S/Ni results in Fig. 18).

Pursuing the fourfold site further by means of an R-factor comparison of experiment and MSC–SW theory, the authors derive a geometry that includes a determination of S–Cr distances down to the fifth layer of the substrate. Some of the results of this R-factor analysis are shown in Fig. 21. It is interesting here that the two sets of data for emission along [001] and [011] azimuths and with polarization nearly parallel to each emission direction are complementary in their sensitivities to different structural parameters. The [001] results are much more sensitive to the Cr_7-atop position because strong single and multiple backscattering can be involved (cf. Fig. 3b–i). By contrast, the [011] data is much more sensitive to the Cr_7-open position for the same reason. The polarization orientations enhance these effects by preferentially directing the initial photoelectron wave toward these scatterers (cf. Fig. 3a). The final results of this
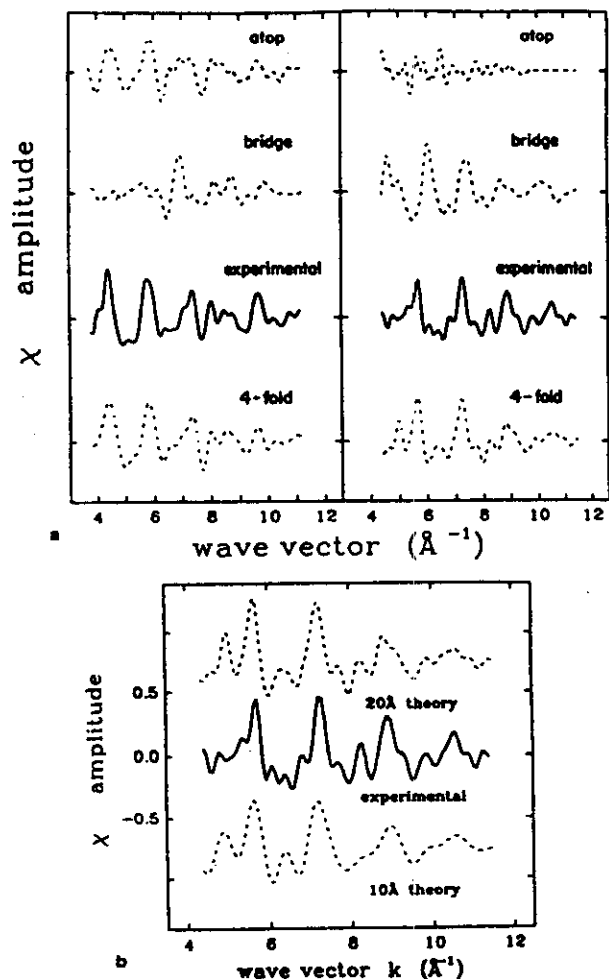
FIGURE 20. (a) Comparison of scanned-energy S 1s experimental data for emission from c(2 × 2) S on Cr (001) along the [001] direction (left panel) and [110] direction (right panel) with MSC-SW calculations for different adsorption sites of atop, bridge, and fourfold. (b) As in (a), but comparing the data obtained in the [011] azimuth to MSC-SW theory for the final optimized fourfold-hollow structure with different path-length cutoffs of 20 Å and 10 Å. (From Ref. 20.)

FIGURE 21. R-factor analysis of the scanned-energy results of Fig. 20, showing the geometry involved and the variation of the R factor with various S–Cr layer separations. (From Ref. 20.)

R-factor analysis show an 8% reduction of the mean separation of the first and second Cr layers (compare the 3% expansion in similar S/Ni results in Fig. 19) and further suggest a slight corrugation of the second layer and a slight expansion of the separation of the second and third layers, although the latter are not fully conclusive within the error limits of 0.02–0.03 Å estimated by the authors.
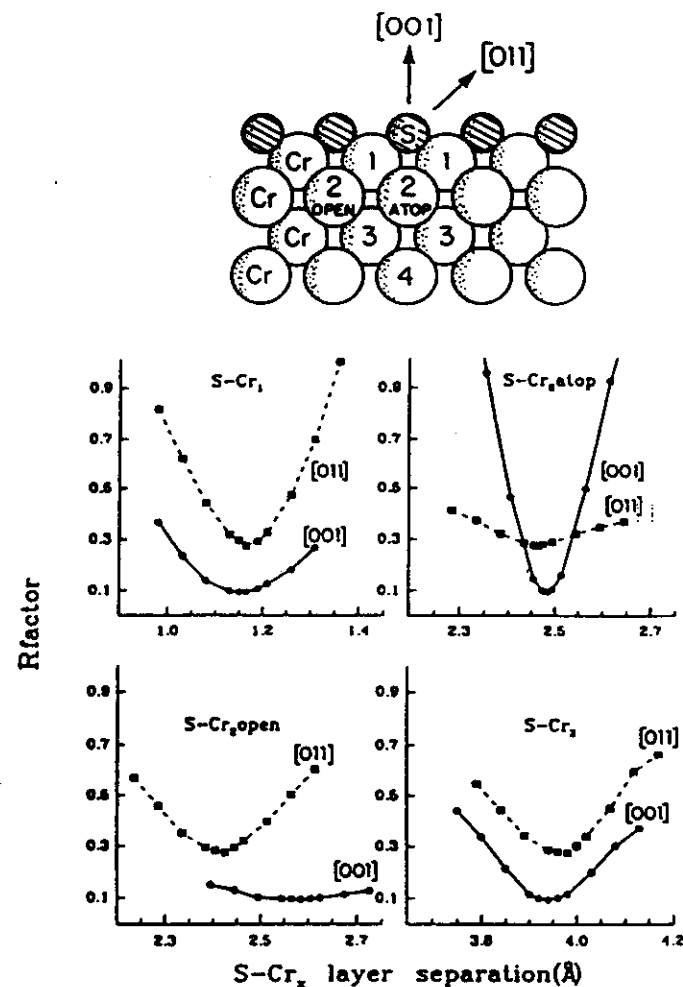
A further important point made in this work is that the $\chi(k)$ curves exhibit fine structure associated with path-length differences out to about 20 Å. Such fine structure in ARPEFS data and the need to use rather large clusters of up 50–100 atoms to adequately model S/Ni data have also been discussed previously (see Fig. 19 and Ref. 21). The work by Terminello et al. shows this explicitly by comparing experimental $\chi(k)$ curves for S/Cr with MSC-SW curves that have

been cut off at both 10 Å and 20 Å total scattering lengths; these results are presented in Fig. 20b, where it is clear that the fine structure in experiment is better modeled by the 20-Å curve, especially for wave vectors above about 7 Å^{-1}. This sensitivity permitted a final determination of Cr layer spacings down to that between the fourth and fifth layers, although the accuracy decreases from an estimated ±0.02–0.03 Å for the first three spacings to ±0.07 Å for the fourth spacing measured. It is, finally, worth noting that the approximately 20 Å limit noted here is in the same range as that found in the higher-energy scanned-angle O/Ni results presented in Fig. 16. Thus, both methods seem to have similar sensitivity to more-distant neighbors.

This work demonstrates the full power of the scanned-energy approach, provided that the initial intensities are measured carefully and that the final results are analyzed by means of a quantitative comparison of experimental $\chi(k)$ curves with calculations for a range of choices of geometrical parameters. A very similar analysis has been carried out for the system $c(2 \times 2)$ S/Fe (001) by Zhang et al.[102] Although much more time-consuming multiple-scattering calculations were used for all of the geometries tried in these cases, it should be possible in general to do a much more rapid search for promising geometries in single scattering, with only fine tuning of the parameters then being required in multiple scattering.

4.3. Epitaxial Oxide, Metal, and Semiconductor Overlayers

4.3.1. NiO/Ni (001)

Although the case of NiO grown on Ni (001) considered in the previous section does not represent perfect epitaxy, the degree of agreement between experiment at 1200 L and theory in Figs. 13a and 14 clearly shows that the predominant form of NiO present is of (001) orientation. Certain structural conclusions concerning the form of this oxide and its degree of long-range order before and after annealing have also been made (section 4.2.1 and Refs. 26b,c). An analysis of the LEED spot patterns (including a splitting of the NiO (001) spots and corresponding XPD data in fact suggests a two-dimensional super-lattice growth of NiO (001) with a lattice constant expanded by exactly ¼ with respect to the underlying Ni substrate (cf. Fig. 13b). Although LEED patterns for the unannealed oxide also exhibit a 12-spot ring throught to be due to NiO (111),[97] the XPD results of Figs. 13a and 14 indicate that it is at most a minority species of the total NiO present, since NiO (111) would produce 12-fold symmetric XPD patterns (bottom theory curves in Figs. 13a and 14) that are not seen experimentally. This example thus indicates a very useful sensitivity of high-energy XPD to the orientation of an epitaxial overlayer and its degree of short-range order under various conditions of annealing and deposition.

4.3.2. Cu/Ni (001) and Fe/Cu (001)

We now consider two very different limits of metal-on-metal epitaxial growth taken from some of the first experimental studies in this field, those by Egelhoff

and co-workers and Chambers and co-workers: pseudomorphic epitaxial growth of Cu on Ni[11,103] and island formation by Fe on Cu (001).[104]

Figure 22 illustrates high-energy AED for the first case of Cu on Ni (001). The different near-neighbor forward scattering events allowed as each new Cu layer is added are illustrated by the arrows in Fig. 22a. In Fig. 22b, experimental data from Egelhoff[11] are compared to theoretical SSC–PW curves from Bullock and Fadley.[71] In Fig. 22c, some of the same experimental data are compared to very recent multiple-scattering calculations by Xu and van Hove.[73]

In Fig. 22b, the relatively abrupt appearance at certain overlayer thicknesses of forward-scattering features such as those at $\theta = 45°$ and 90° (normal emission) can be used as a direct measure of the number of overlayers in the range of about 0–3 ML. Comparison with Fig. 22a also shows that the appearance of each of these two peaks corresponds to the onset of forward scattering by the two nearest neighbors encountered in this polar scan from [100] to [001]. The simple origin of these two peaks has also been directly verified by comparing SSC calculations with and without these important scatterers present.[71]

Thus, simple forward scattering peaks from nearest and next-nearest neighbors are very useful in studies of epitaxy, as we have also discussed for the oxide case in the last section. However, the interpretation of weaker features such as those at $\phi \approx 20°$ and 70° in Fig. 22b need not be so simple. Calculations with various atoms removed from the cluster show that these have more complex origins which require at least a full SSC calculation for their explanation.[71] For example, the peak near 70° is a superposition of simple forward scattering by atoms along [103] and [102] and, more importantly, first-order effects (cf. the inset of Fig. 8) from the atoms along [001] and [101]. Thus, for atoms that are further away than the first three or four spheres of neighbors, a mixed origin in forward scattering and higher-order interference effects is generally to be expected. This conclusion has also been confirmed in a recent analysis by Osterwalder et al.[46] of an extensive set of high-resolution Ni $2p_{3/2}$ data from bulk Ni (001) that we discuss further in section 5.1.

Figure 22a also makes it clear that, in pseudomorphic growth with the lateral lattice constants locked to those of Ni, the vertical spacing of the Cu layers will determine the θ position of the peak near 45°. A ±1° change in this peak position from 45° would correspond to a ±0.12-Å change in the vertical lattice parameter or a ±0.06-Å change in the interplanar spacing. This sensitivity has in fact recently been used by Chambers et al.[12a,b] to measure the degree of outward vertical relaxation in thin Cu overlayers on Ni (001). It should thus be possible to measure interlayer spacings with accuracies of better than 0.1 Å in this way[24,71,73] although doing some sort of theoretical modeling at least at the SSC–PW or SSC–SW level (as Chambers et al. have done[12]) is advisable to verify peak origins, shapes, and predicted shifts with relaxation. Using higher angular resolution also should be beneficial for such studies by making it possible to determine forward-scattering peak positions more precisely.

The main point of discrepancy between experiment and SSC–PW theory in Fig. 22b is that the peak for forward scattering along the nearest-neighbor [101] direction has a relative intensity too high for thicker overlayers by about a factor of about 2. As expected from the prior discussion of Fig. 5, using spherical-wave
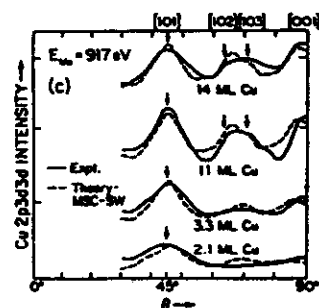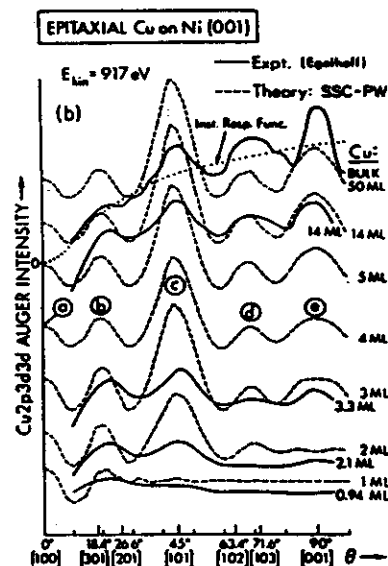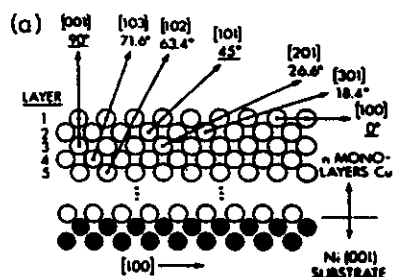
FIGURE 22. (a) Illustration of possible near-neighbor forward scattering events in the [001]-[100] plane for Cu grown in pseudomorphic epitaxy on Ni (001). Only those at 45° and 90° are fully explained by the simple one-event interpretation suggested here. (b) Experimental Cu Auger polar scans at 917 eV (from Ref. 11) are compared to SSC-PW calculations for successive layers of epitaxial growth of Cu on Ni (001) (from Ref. 71). Although the Cu LMM Auger intensity is monitored here, very similar results are obtained from the Cu 3p photoelectron intensity. (c) The same experimental data are compared to multiple-scattering cluster calculations. (From Ref. 73.)

scattering in the SSC model is found to significantly improve agreement for this relative intensity by reducing it to about $\frac{1}{3}$ of the magnitudes seen in Fig. 22b for thicknesses >3.0 ML[90b]; it is nonetheless still too high by 1.3–1.5 times in comparison with experiment. The remaining discrepancy is due to multiple scattering effects, and the calculations of Fig. 22c include the additional defocusing of intensity along the [101] direction. Much more quantitative agreement with experiment is obtained here. However, even though certain forward-scattering peaks may have their relative intensities decreased by multiple scattering, it should nonetheless still be possible to use the peaks along [001] and [101] in the simple way described in the preceding paragraphs to monitor overlayer thicknesses and determine interlayer relaxations.[71,73]

A more recent paper by Egelhoff[103] has also looked experimentally at a single pseudomorphic Cu (001) layer on Ni (001) buried under various numbers of Ni (001) overlayers. In this work, the attenuation and broadening of certain features with increasing layer thickness is interpreted as evidence of stronger multiple-scattering effects in emission from greater depths. Although the defocusing effects seen in the MS results of Fig. 6 make this a plausible conclusion, Herman et al.[105] have made SSC–SW predictions for the cases studied, and these are found to show very similar attenuation to the experimental data. As one example of this comparison of experiment and SSC–SW theory, Fig. 23 shows results for the 917 Auger peak; the experimental data have been corrected for the θ-dependent instrument response by dividing by the curve for a single Cu
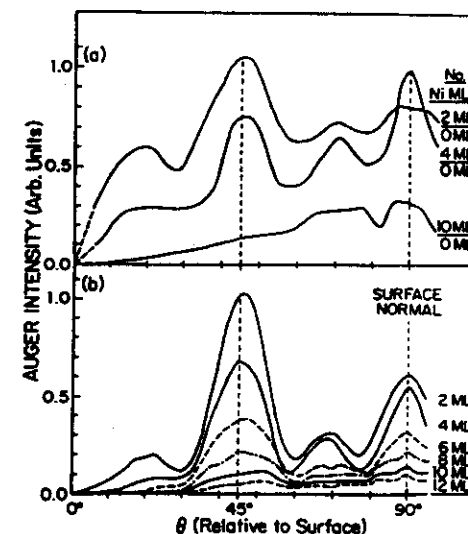

FIGURE 23. (a) Experimental data for Auger emission from a single pseudomorphic Cu (001) layer on top of Ni (001) buried underneath different numbers of layers of epitaxial Ni, also in (001) orientation. (From Ref. 103) (b) Theoretical calculations within the SSC-SW approximation of the results in (a), including curves for other overlayer thicknesses. (From Ref. 105.)
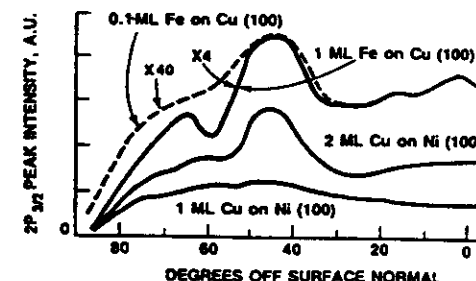
monolayer with no overlying Ni (shown as "0 ML"). Although the relative intensity of the peak at 45° compared to that at 90° is again predicted in theory to be too high, the trends in experiment as the Ni overlayer is increased in thickness are surprisingly well reproduced by the SSC calculations. In particular, the change in the absolute intensity of the peak at 45° with thickness is well reproduced by the calculations, and its final broadening out and diminution of importance in comparison to the peak at 90° is also correctly predicted. Discrepancies noted are that the broad, flat feature seen in experiment at about 70° is not fully developed in the single scattering theory and that an initial narrowing of the peak along 45° that may be due to multiple-scattering effects (cf. the discussion of Fig. 6 and Fig. 22c) is not seen. Experimental errors of as much as ±10–20% in measuring the number of monolayers (cf. calculated curves at other thicknesses), as well as the possible presence of defects in the growing Ni layer,[12a,b] could also affect the agreement between experiment and theory. More recent multiple-scattering calculations for this buried-monolayer system by Xu and van Hove[73] and by Kaduwela et al.[84] yield a more quantitative description of the decrease in intensity of the peak at θ = 45°, although the experimental overlayer thicknesses have to be decreased ·by from 0.6 to 1.5 ML in the calculations to yield optimum agreement. However, on going to thicker over-layers on the order of ten layers, there is still a stronger peak in MS theory than in experiment near θ = 70°.

Thus, although such a deeply imbedded emitter layer clearly represents an extreme case of the type shown in Fig. 3b–ii, for which multiple-scattering effects ought to be maximized, the case for these data definitely exhibiting such effects is not as strong as might be expected, and the SSC approach still yields at least a semiquantitative description of the data.

A final note of caution in connection with this study[103] concerns the idea that classical trajectories can be used to predict when and how multiple scattering will be important in AED or XPD. Although classical arguments can be didactically useful once the correct answer is known, taking them further seems to be very risky, particularly when the quite simple and wave-mechanical SSC model is already available for comparisons to experiment and to more-accurate calculations including higher-order multiple scattering.

We now turn to the second system: Fe/Cu (001) as studied by Chambers, Wagener, and Weaver[104a] and by Steigerwald and Egelhoff.[104b] Figure 24 shows a similar set of AED data from the latter study for the case of Fe deposited on Cu (001) at ambient temperature and compares it to results like those in Fig. 22b. It is striking here that coverages of one monolayer or less (even down to 0.1 ML) already exhibit the strong forward-scattering peak at 45° characteristic of fcc Fe in islands or clusters at least two layers thick, as well as the beginning of the peak along the surface normal associated with three-layer structures. In fact, the 1-ML Fe curve looks very similar to that for 3.3 ML of pseudomorphic Cu in Fig. 22b. These results[104b] and a more detailed set of polar and azimuthal data discussed by Chambers et al.[104a] thus show that at least the first one or two layers of Fe grown under these conditions have a strong tendency to agglomerate on Cu (001), a conclusion that has important implications for the magnetic properties of such overlayers.[104] This work nicely demonstrates the general usefulness of such

FIGURE 24. Experimental polar scan data for Fe $2p_{3/2}$ emission at 780 eV from Fe deposited at ambient temperature on Cu (001). Data for both 0.1 ML and 1 ML total cover-ages are compared to similar results for Auger emission from Cu depos-ited up to 1 ML and 2 ML on Ni (001); cf. Fig. 22(b). Note the pre-sence of strong forward scattering peaks at 45° in both Fe curves and the beginning of a peak along normal for the 1-ML Fe data. [From Ref. 104(b), with more detailed polar and azimuthal data appearing in Ref. 104(a).]

scanned-angle measurements for detecting the presence of island or cluster formation, as discussed further in section 4.5.

4.3.3. Fe/GaAs (001)

We now consider another example from the work of Chambers et al.[12a,b] in which Auger electron diffraction has been applied to the growth of epitaxial layers of Fe on GaAs (001). This system has been studied extensively because of its interesting magnetic anisotropies in the surface plane, as first discussed by Krebs, Jonker, and Prinz.[106] It is complicated by the fact that outward diffusion of As is thought to occur, even though at the same time the Fe atoms appear in LEED to be growing in (001) epitaxy. A polar scan in the [100] azimuth of the $L_3M_{4,5}M_{4,5}$ Fe Auger peak at approximately 710 eV kinetic energy provides further information on how this might be occurring, as illustrated in Fig. 25. Here, the experimental AED curve of Chambers et al. for a 10-ML Fe overlayer on GaAs is compared to an analogous experimental Fe $2p_{3/2}$ XPD curve for a clean bcc Fe (001) surface due to Herman et al.[107]; the XPD peak furthermore has a kinetic energy of about 780 eV, very close to that of the Auger peak, so that the two diffraction patterns would be expected to be very similar for a given crystal structure. In fact, the two experimental curves are very different, with the bcc Fe (001) showing a much lower intensity for the peak along [101] and different fine structure at polar angles of about 15–30° and 60–75°.

Also shown in Fig. 25 are SSC-PW theoretical curves for three overlayer crystal structures: bcc Fe with $a = 2.82$ Å [the bulk-lattice constant which also gives a very good match to the GaAs (001)], primitive cubic (pc) Fe with $a = 2.82$ Å, and fcc Fe with $a = 2.82$ Å. It is clear that the fcc calculation gives the best agreement with the Fe/GaAs experimental data as to both the relative intensity of the [101] peak and the fine structure. The calculations for the other two structures seriously underestimate the intensity of the peak along the {101} direction. The bcc calculation also agrees best with the XPD curve from clean Fe (001), particularly as to the relative intensities of the weaker features from θ = 15° to 75°, even if all of the fine structure is not correctly predicted. All
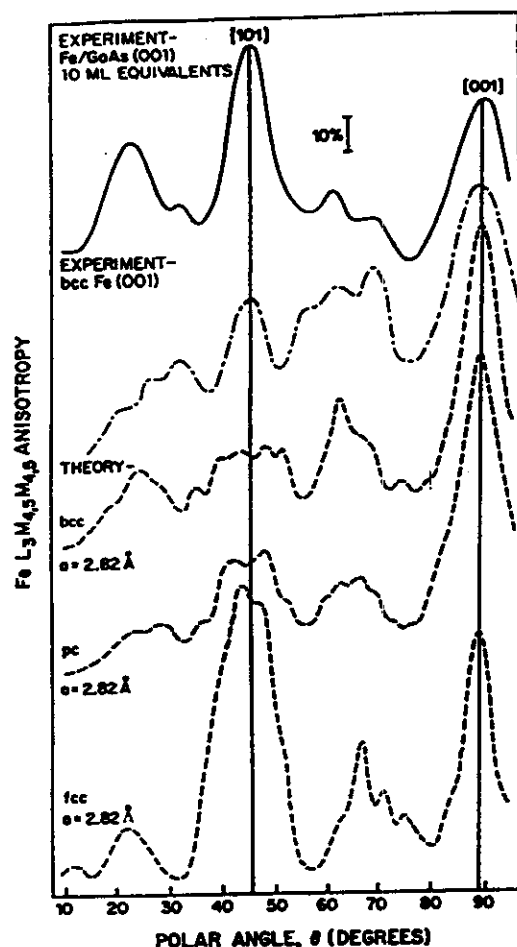
FIGURE 25. Experimental polar scan of the Fe LMM Auger intensity at 703 eV from 10 ML of Fe deposited on GaAs (001) (solid curve) is compared to theoretical calculations for various Fe lattices (dashed curves). (From Ref. 12(b).) The scans are in the [100] azimuth (ϕ = 0°), with the directions [101] and [001] indicated. The calculations are at the SSC-PW level, and they are shown for Fe in three crystal structures: bcc, pc (primitive cubic), and fcc (which is proposed to be bcc Fe with As atoms outwardly diffused into the fcc interstitial sites). Also shown for comparison is an experimental polar scan for bulk Fe (001) in the same azimuth (dot-dash curve) from a separate study. (From ref. 107.)

calculations predict a strong peak along the normal or [001] direction; this is due to forward scattering from atoms with a closest spacing of $1.000a$ for all three structures. Along the [101] direction, by contrast, the fcc structure has nearest-neighbor scatterers at a distance of $a/\sqrt{2} = 0.707a$ (cf. Fig. 22a) whereas, in the bcc and pc structures, the nearest scatterers are twice that distance away at $\sqrt{2}a = 1.414a$. This explains the stronger forward-scattering peak along [101] in the fcc theory.

The combined experimental and theoretical results in Fig. 25 thus suggest that the local structure in Fe/GaAs has scatterers that are at the fcc positions. These results have been explained by the interesting proposal[12a,b] that the outward-diffusing As atoms occupy the face-centered positions in a bcc Fe lattice so as to yield an overall AED pattern that is essentially fcc in nature. Although Fe and As are slightly separated in atomic number (26 and 33, respectively) so that the all-Fe calculations of Fig. 25 are not in that case strictly correct, the forward-scattering strength that is dominant at these energies is not a strong function of atomic number (but rather of atomic size, as noted in section 3.1.3), and thus these theoretical simulations should be reasonably accurate for the hypothesized structure as well.

This work thus illustrates another aspect of higher-energy AED and XPD that should be generally useful in studying the detailed structures of complex epitaxial overlayers that may have impurities present, such as atoms diffusing outward from the substrate or inward from the surface. An obvious complementary and useful type of data that could be derived for such a system would be to look at the AED or the XPD of the impurity. For the example of Fe/GaAs, if the hypothesized structure is correct, As also should show an fcc type of diffraction pattern, although perhaps weaker or with less fine structure if it is preferentially segregated to the surface of the Fe overlayer. Another recent example of this type is a combined AED/XPD study of dopant P and Sb atoms in Ge epitaxial layers on GaAs (001) by Chambers and Irwin;[12c] here P was found to occupy lattice sites, whereas Sb was segregated to the surface.

4.3.4. $Hg_{1-x}Cd_xTe$ (111)

As a final example of an epitaxial system, we consider a recent scanned-angle XPD study by Granozzi, Herman et al.[106] of $Hg_{1-x}Cd_xTe$ (111) grown by liquid-phase epitaxy. This sample underwent transport at atmospheric pressure before being studied and was minimally ion-bombarded so as to remove a thin oxide layer from the surface. It was not subjected to bakeout or annealing after ion bombardment, to avoid depleting Hg from the surface region. At the time of measurement, the value of x was approximately 0.4. In spite of the less-than-ideal surface expected to remain after such a treatment, XPD modulations of $\Delta I/I_{max} \approx 15–25\%$ were seen in all of the major photoelectron peaks observable ($Hg\,4f_{7/2}$ at a kinetic energy of 1383 eV, $Cd\,d_{5/2}$ at 1078 eV, and $Te\,3d_{5/2}$ at 910 eV). Qualitatively comparing Hg, Cd, and Te diffractions curves immediately indicated that the Hg and Cd atoms were occupying similar lattice sites, as expected.

As another more subtle structural problem resolvable from this data, the question of the nature of the termination of the surface also was addressed. That is, was the surface terminated preferentially with double layers having cationic Cd (or Hg) on top and anionic Te on the bottom (termed Model A) or with the reverse (termed Model B)? Comparing the azimuthal XPD patterns for Cd and Te obtained at several polar angles with SSC–SW calculations for both Models A and B permits determining the dominant type of termination, even for a surface that probably has a reasonable amount of damage on it. Some of this data is shown in Fig. 26, where Cd emission at $\theta = 19°$ and 35° (both chosen to pass through near-neighbor scattering directions) is considered. It is clear that, for both angles of emission, the agreement between experiment and theory as to both visual fit and R factor[26d] is much better for a Model A termination; peak relative intensities, positions, and fine structure are much better predicted. Similar conclusions can be drawn from analogous Te azimuthal scans.

As one further aspect of this study, we consider the forward scattering origin of the various major peaks observed in Fig. 26 with the aid of Fig. 27, which indicates the several near-neighbor forward-scattering events possible in a surface terminated as in Model A. For the data at $\theta = 19°$, the effects of the event labelled as $\theta = 19°$, $\phi = 0°$ are clear in both experiment and theory. For the data at $\theta = 35°$, the principal peaks are due to events of the types labelled $\theta = 35°$, $\phi = 60°$ and $\theta = 30°$, $\phi = 30°$, 90°.

The analogous Te curves at these polar angles are very different from those of Cd in both experiment and theory, with peak shifts and relative intensity
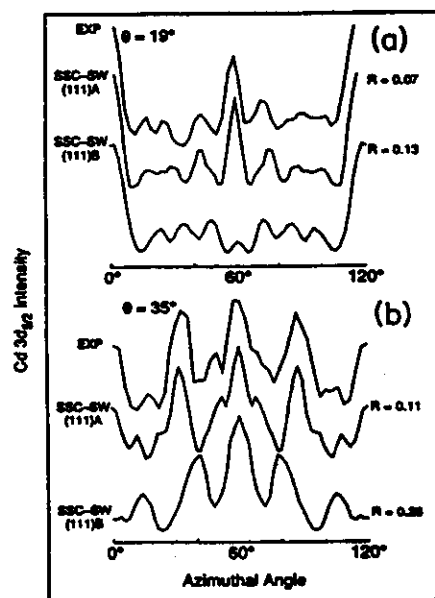

FIGURE 26. Al Kα-excited azimuthal scans of Cd 3d$_{5/2}$ intensities from Hg$_{1-x}$Cd$_x$Te(111) ($x = 0.4$) at polar angles of (a) 19° and (b) 35° passing through or very close to forward-scattering low-index directions shown in Fig. 27 as $\theta = 19°$, $\phi = 0°$, $\theta = 35°$, $\phi = 60°$, and $\theta = 30°$, $\phi = 30°$, 90°. Also shown are SSC–SW curves for the two possible surface terminations (Model A = Cd or Hg on top, Model B = Te on top), together with R factors comparing experiment and theory. (From Ref. 108.)
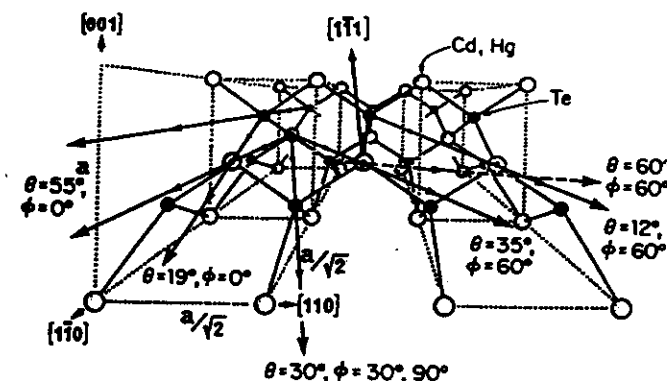
FIGURE 27. Perspective view of the unreconstructed (111) surface of Hg$_{1-x}$Cd$_x$Te(111) in the Model A surface termination of Fig. 26, with the θ, ϕ coordinates of various near-neighbor/low-index directions along which forward scattering might be expected to be strong. These directions would be the same for the unreconstructed (111) surfaces of any material with the zincblende or diamond structure, as will be used later in discussing Fig. 36.

changes. In particular, the peaks at $\theta = 35°$, $\phi = 30,°$ and 90° for Cd disappear in Te and are replaced by two weaker features at $\theta = 35°$, $\phi \sim 38°$ and 80°. This is easily explained, since Fig. 27 shows that, in an A-type termination, the peaks that disappear are only strong forward-scattering events in the first double layer for Cd emission; thus, they are not expected to be seen for Te.

Inspection of other azimuthal data of this type shows that most of the strong features can be assigned an origin in the various simple near-neighbor forward-scattering effects illustrated in Fig. 27, although it is again important to realize that higher-order interference effects can significantly influence the intensities due to forward scattering by atoms further from the emitter (cf. the discussion of Fig. 22 and, below, Figs. 37 and 38).

This study thus illustrates the further use of higher-energy XPD for epitaxial systems, for which bonding sites of substitutional atoms and the type of surface termination of a compound semiconductor can be determined.

4.3.5. Diffraction Effects in Quantitative Analysis and Photoelectron-detected EXAFS

We conclude this discussion of epitaxial systems with two notes of caution concerning the strong diffraction effects that are expected in either photoelectron or Auger emission from well-ordered lattices.

Diffraction Effects Must Be Carefully Allowed for in Any Attempt to Do Quantitative Analyses of Surface Composition. Methods of correcting for such effects have been considered by both Connelly et al., for simple adsorption on a metal,[109] and more recently for semiconductor surfaces by Alnot et al.[110] Not adequately allowing for such effects can lead to errors of as high as ±50% in

measured stoichiometries! Some of the methods for such corrections are averaging over diffraction curves obtained in more than one polar or azimuthal scan, taking advantage of the crystal-structure symmetry to find scans in which different constituents will have nearly identical diffraction patterns (e.g., this is possible in the zincblende structure[110]), or using theoretical calculations to try to determine directions in which diffraction effects can be neglected.

By contrast, a potentially useful aspect of diffraction effects for surface analysis is in monitoring intensities along different directions as a function of coverage during epitaxial growth, as suggested by Idzerda et al.[67] Model calculations of such curves in the SSC–PW model suggest that it should be possible to resolve the completion of the first few layers of growth.

The Use of Photoelectron Intensities to Monitor EXAFS-like *Oscillations Requires Sufficient Angular Averaging.* The idea of using photoelectron intensities to measure EXAFS oscillations for near-surface species has recently been proposed by Rothberg et al.[111] and applied to semiconductor systems by Choudhary et al.[112] It is clear from the strong oscillations of up to 70% seen in scanned-energy photoelectron diffraction and their dramatic dependence on emission direction (cf. Fig. 20) that an adequate averaging over direction must be undertaken to yield something related to the 4π-averaged EXAFS signal. Although this is automatic for disordered or polycrystalline systems,[111] it is problematic in single-crystal studies. Lee[41] has in fact questioned on theoretical grounds whether even the maximum 2π averaging possible in photoemission for such cases is sufficient to yield the EXAFS limit. Nonetheless, preliminary experimental results of this type[112] using the modest type of averaging inherent in the conical solid angle of a cylindrical mirror analyzer (CMA) appear to yield EXAFS-like data. However, it is the author's opinion that a single-geometry CMA measurement does not represent sufficient angular averaging to reliably yield the EXAFS limit and that the close similarity of these result to EXAFS data may have a fortuitous component. Perhaps measuring intensities for several different orientations of the specimen with respect to the analyzer would improve the reliability of this approach, but it is not clear that this has been done to date. The solid-angle averaging of a particular analyzer could also be checked by carrying out SSC calculations over the directions involved and summing these intensities, as was done recently by Idzerda et al. in another context.[67]

Overall, both XPD and AED thus have considerable potential for the study of the morphology of the first 1–5 layers of an epitaxial system. The strongest peaks are expected to be directly connected with simple forward scattering from the first few spheres of neighbors around a given emitter. Weaker features may involve a superposition of several types of scattering events. Thus, a quantitative analysis of the full intensity profile will require calculations at least at the SSC level. Predicting peak relative intensities correctly if emission along a dense row of atoms is involved may also require the inclusion of multiple scattering. However, much useful information about the surface structure, layer thickness, morphology, impurity-site type, and surface termination should be derivable from a consideration of the possible strong forward-scattering peaks due to the nearest
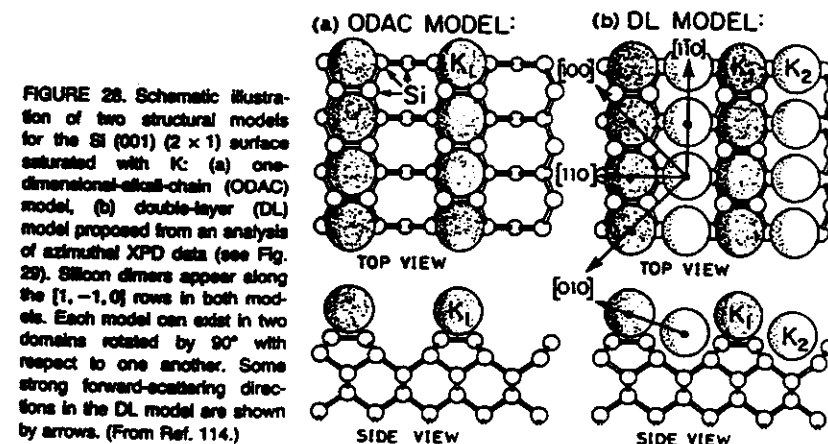
neighbors (cf. Figs. 22 and 27) combined with theoretical modeling at the single scattering level.

4.4. Metal–Semiconductor Interface Formation

We now consider two recent examples of the application of higher-energy XPD to the study of metal–semiconductor interface formation. This kind of XPD study was pioneered by Kono and co-workers, and more detailed discussions appear elsewhere, including work on other metal–semiconductor combinations.[49,113,114] The examples chosen here both involve the initial stage of metal reaction with Si surfaces and represent structures over which controversy still exists. The examples differ in the final structure proposed. The first case, K/Si (001), is a metal overlayer relatively far above the Si surface. The second case, Ag/Si (111), is a metal layer nearly coplanar with the first Si layer. This strongly affects the degree and manner in which forward scattering by Si or metal atoms influences the observed diffraction patterns.

4.4.1. K/Si (001)

In this study by Abukawa and Kono,[114] azimuthal K $2p$ XPD data have been obtained for the structure formed by depositing K to saturation onto the Si (001) (2 × 1) reconstructed surface. The substrate surface is thought from a number of previous studies to consist of rows of dimers, as shown by the small open circles in Fig. 28. The most-often-discussed model for the potassium structure on this surface is the so-called one-dimensional-alkali-chain (ODAC) model illustrated in Fig. 28a; it corresponds to a $\frac{1}{2}$ ML coverage, and leaves open grooves adjacent to each high-lying row. However, there is still considerable controversy surrounding the structure of K adsorbed on Si (001), and this geometry has not been directly determined.[115] There is also disagreement as to what constitutes the saturation coverage of K on the surface.[114,115b]

FIGURE 28. Schematic illustration of two structural models for the Si (001) (2 × 1) surface saturated with K: (a) one-dimensional-alkali-chain (ODAC) model, (b) double-layer (DL) model proposed from an analysis of azimuthal XPD data (see Fig. 29). Silicon dimers appear along the [1, −1, 0] rows in both models. Each model can exist in two domains rotated by 90° with respect to one another. Some strong forward-scattering directions in the DL model are shown by arrows. (From Ref. 114.)

Even before considering the actual XPD data, we note that, if only atoms of type K_1 in the ODAC structure are present, the diffraction patterns would be dominated by forward scattering from other K_1 atoms, and this would furthermore be strong only for very low θ and along the $\langle 1, -1, 0 \rangle$ rows for which the interatomic distances are shortest. The Si atoms should play only a minor role, perhaps producing fine structure in the azimuthal curves for very low takeoff angles.

A set of azimuthal experimental data for this system with emission angles relative to the surface of $14° - 22°$ is shown as the points in Fig. 29. The strongest peak is seen along $\langle 100 \rangle$ for a relatively high value of $\theta = 14°$, an observation which already seems at odds with the ODAC model. Considering also the experimental anisotropy $\Delta I / I_{max}$ (scale along left of figure), we see that it can be as high as about 30%, a value which is significantly above those expected in general for such higher-θ scattering from neighbor atoms that are either all in-plane or all below-plane relative to the emitter (cf. Fig. 15 for $c(2 \times 2)$ O/Ni (001) as a typical example).

These results suggest trying in addition to the ODAC model another structure in which there are scatterers well above some K emitters. One such model is the obvious one of putting rows of atoms of type K_2 in all of the grooves to yield a 1-ML coverage, as illustrated in Fig. 28b. For this double-layer (DL) model, strong forward scattering can occur for higher takeoff angles, as indicated by the arrows along both $\langle 110 \rangle$ and $\langle 100 \rangle$ directions. For very low takeoff angles approaching zero, either model is expected to show strong forward scattering for emission along the K rows parallel to $\langle 1, -1, 0 \rangle$. The presence of two equivalent domains of either structure rotated by 90° with respect to one another also implies
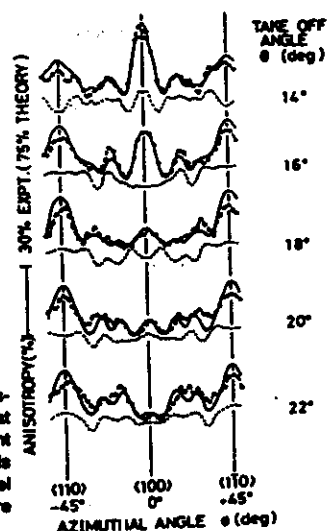
FIGURE 29. Azimuthal data for Al $K\alpha$-excited K $2p$ emission from the Si(001) (2×1) surface saturated with K at polar angles from 14° to 22° above the surface. Experiment is compared with SSC-PW calculations for the two models shown in Fig. 28: ODAC = dashed curves and DL model = best fitting data = solid curves. Very similar curves were also obtained with SSC-SW calculations. (From Ref. 114.)

summing two diffraction patterns in the analysis and overall C_{4v} symmetry in both the observed and calculated patterns.

Comparing these experimental data to SSC-PW (or very similar SSC-SW) calculations for the two models[114] is now found to yield clearly superior agreement for the DL model (solid curves in Fig. 29). The strong peak at $\phi = 0°$ which grows in for θ approaching 14° can be explained as being due to emission from K_2 atoms and scattering by their second-nearest K_1 neighbors along $\langle 100 \rangle$. The peaks along $\langle 110 \rangle$ and $\langle 1, -1, 0 \rangle$ are due to K_2 emission again, but now involve scattering from nearest-neighbor K_1 atoms (and a sum over domains 90° apart). Additional azimuthal data for θ as low as $4°$[114] show strong peaks for $\phi = \pm 45°$ that can be ascribed to the expected forward scattering along $\langle 1, -1, 0 \rangle$ directions within either K_1 or K_2 rows. Not surprisingly, these latter peaks are also present for very low θ in the theoretical curves for both models, and they are the most significant features in calculations for the ODAC model. Comparing experiment and theory for these lower-θ data also is found to support the DL model. By testing various vertical placements of the two K row types, the authors were able to determine a 1.1 Å vertical separation between the two K rows, and less accurately to determine that the bottom K row was not lower than about 0.5 Å above the first Si layer. For such a 1.1-Å separation, the K_1–K_2 distance is 3.99 Å and slightly larger than the K–K distance of 3.84 Å along either the K_1 or K_2 rows. It is also interesting that, for this structure, the $K_2 \rightarrow K_1$ forward scattering peaks should occur at $\theta \approx 16°$ along [110] and $\theta \approx 11°$ along [100]; this explains the strong peaks seen in the data over this range of polar angles. The registry of the DL along $\langle 1, -1, 0 \rangle$ with respect to the underlying Si surface was not determined, but the six-coordinate site shown in Fig. 28b for atoms of type K_1 is that predicted by theory to be the lowest energy.[115a,d]

In a more recent theoretical study of this system by Ramirez,[115d] it is found that adsorption in groove sites (including type K_2 in Fig. 28b) is significantly lower in energy than the six-coordinate site shown for K_1 atoms. Thus, adsorption in the grooves is supported by theory as well. However, the 1-ML structure proposed in this study is different from Fig. 28b in that the atoms of type K_2 are shifted along the $\langle 1, -1, 0 \rangle$ direction so as to be directly opposite the Si dimers. The K_2 atoms in this model are also predicted to be approximately in-plane with respect to the Si dimers. However, it is doubtful that this structure would yield the strong forward scattering peak seen in XPD along $\phi = 0°$ for relatively high theta values of 12–16°. Thus, even though these calculations[115d] indicate that a double layer with such shifted K_2 atoms is lower in energy than the structure shown in Fig. 28b, the latter structure still represents a better choice based upon the XPD data.

Overall, these XPD results thus provide important new insights into the bonding of K on Si (001) and illustrate several aspects of the use of this technique for metal-semiconductor studies.

4.4.2. Ag/Si (111)

The Ag/Si (111) system has been studied by almost every modern surface-science technique and is known to exhibit, among other things, a well-ordered

($\sqrt{3} \times \sqrt{3}$) Ag structure and the formation of fcc Ag clusters or islands with (111) orientation for exposures that go above the 0.7–1.0 ML needed just to form the ($\sqrt{3} \times \sqrt{3}$) structure.[49,50,116,117] In the following section, we consider the use of XPD in studying such clusters; here, we concentrate on a recent XPD study by Bullock et al. of the ($\sqrt{3} \times \sqrt{3}$) structure.[50a,b]

In this study, polar and azimuthal Ag $3d_{5/2}$ XPD data were obtained for a well-ordered and very stable ($\sqrt{3} \times \sqrt{3}$)Ag structure, and these experimental results are summarized in Figs. 30a and 31. The smooth and structureless nature of the polar scans in Fig. 30a indicates an absence of strong forward scattering effects, except perhaps at very low takeoff angles of $\theta \approx 4$–$8°$ where a four-peak structure is seen in Fig. 31. A simple geometric calculation then permits the conclusion that the Ag cannot be more than approximately 0.5 Å below the surface Si layer. This is also consistent with the lower anisotropy values of no more than 21% that are found for the azimuthal scans of Fig. 31. It can thus be concluded that there are no strong forward scatterers above the Ag. The azimuthal data are also fully consistent with an earlier XPD study of this system by Kono et al.,[49] but they are more detailed in involving full 360° ϕ scans and more θ values.

It is beyond the scope of this review to discuss the many models that have been and are being proposed for this structure, but all known structures have been tested against this azimuthal data by Bullock et al., using R factors[264] as the final quantitative measure of goodness of fit. The calculations were carried out at the SSC–SW level, and in final optimizations also with the full final-state interference of $3d$ emission into p and f channels. (This latter correction was not found to alter the structural conclusions, a result which is expected to be true in general for higher-energy XPD, but certainly not for work at less than a few hundred eV, as discussed in section 3.1.2).
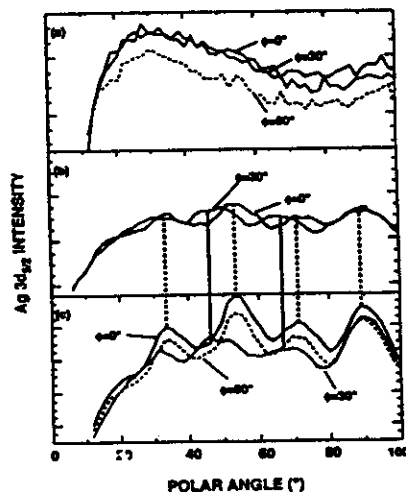

FIGURE 30. Polar XPD scans of Ag $3d_{5/2}$ intensity at 1120 eV from: (a) the ($\sqrt{3} \times \sqrt{3}$) Ag structure on Si (111) formed after annealing an ~1.3-ML Ag overlayer to 550°C; (b) a Ag overlayer of approximately 2 ML average thickness at 450°C; and (c) a thick Ag overlayer of approximately 6 ML thickness at ambient temperature. (From Ref. 50.)
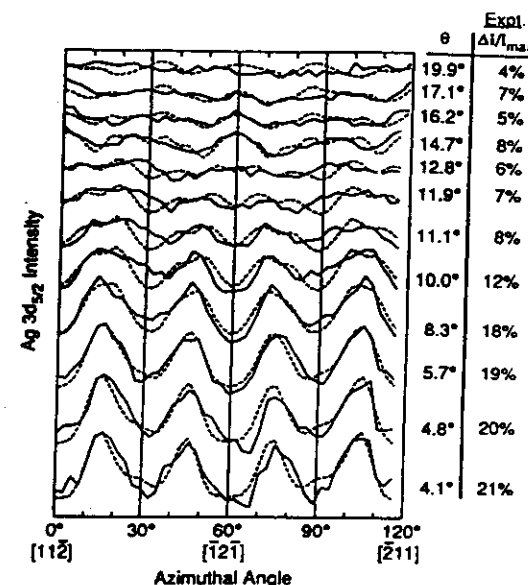
POLAR ANGLE (°)

FIGURE 31. Azimuthal XPD scans of Ag $3d_{5/2}$ intensity from ($\sqrt{3} \times \sqrt{3}$) Ag/Si (111) at polar angles from 4° to 20° (solid lines) are compared to SSC-SW calculations for the optimized two-domain model of Fig. 32 (broken lines), for which $s_1 = s_2 = 0.86$ Å; $z_1 = -0.10$ Å, $z_2 = -0.30$ Å, and a 50:50 mixture of the two domains. Full final-state interference in the d- to $-p + f$ emission process has been included. This comparison yields an R factor of 0.14 (cf. values in Figs. 21 and 26). (From Ref. 50.)

The final model proposed on the basis of this work is for two nearly equivalent domains of Ag in a honeycomb array on a Si surface that has had the top layer of the first Si double layer removed. This two-domain missing-top-layer (MTL) model is illustrated in top view in Fig. 32. The optimized structural parameters are a contraction of the Si trimers toward one another in both domains of $s_1 = s_2 = 0.86$ Å, vertical distances of the Ag relative to the Si layer of $z_1 = -0.1$ Å for Domain 1 and $z_2 = -0.3$ Å for Domain 2 (that is, the Ag is very nearly coplanar with the Si in both domains, but just slightly below it), and a mixture of the two domain types that is between 50:50 and 40:60, with Domain 2 perhaps being slightly more predominant. The fits between experiment and theory for this fully optimized structure are shown in Fig. 31. All other models that have been tried yield significantly worse agreement as judged both visually and by R factors. This two-domain model is also closely related to one derived in a prior XPD study by Kono et al.: a single-domain MTL Ag honeycomb structure of type 1 with $s = 0.66$ Å and a vertical distance of -0.15 Å. The presence of Domain 2 is suggested to explain the four-peak structure at low θ values in Fig. 31, as illustrated by the nearest-neighbor forward-scattering peaks for the two domains shown at the bottom of Fig. 32. For
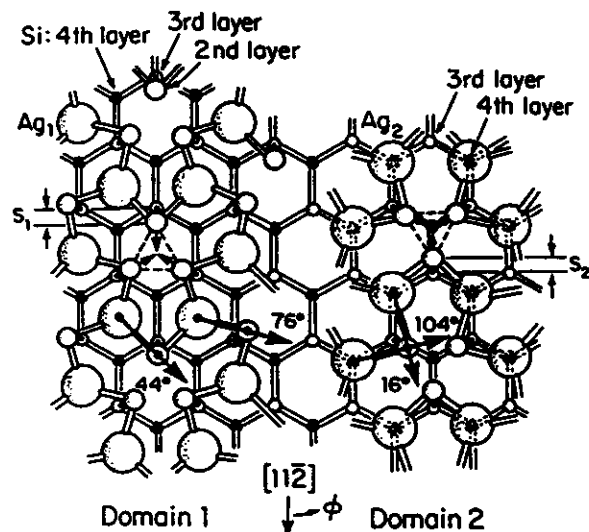
FIGURE 32. The two-domain missing-top-layer (MTL) honeycomb model proposed for ($\sqrt{3} \times \sqrt{3}$) Ag/Si (111). The parameters characterizing it are: vertical positions $z_1 = -0.1$ Å and $z_2 = -0.3$ Å. Si trimer contractions of $s_1 = s_2 = 0.86$ Å, and a 50:50 mixture of Domains 1 and 2. The lower half of the figure shows the two sets of nearest-neighbor Si forward-scattering peaks that produce the four-peak structure seen at low θ values in Fig. 31. (From Ref. 50.)

the lowest θ values near 4°, an additional correction of possible importance is the reduction of nearest-neighbor Si forward-scattering strengths due to multiple scattering effects along the nearly linear rows of atoms that can be labelled Ag emitter → Si first-neighbor scatterer → Si second-neighbor scatterer (cf. Figs. 32, 3b, and 6); very recent MS calculations by Herman et al.[50c] show that this reduces the absolute peak intensities for $\theta = 4°$ and $\phi = 16°$, 44°, 76°, and 104° by about 30%, thus improving the agreement of theoretical and experimental anisotropies.

A further interesting point in connection with this structure is that a recent LEED study of the clean Si (111) surface by Fan et al.[117] concludes that a little-studied ($\sqrt{3} \times \sqrt{3}$) Si reconstruction has very nearly the same geometry as Domain 1 in Fig. 32 if Ag adatoms are replaced by Si adatoms. Although these authors do not consider the possibility of a second domain of type 2 for ($\sqrt{3} \times \sqrt{3}$) Si, it might be expected to have approximately the same energy (due to weak fourth-layer interactions) and thus also to exist on the clean surface. This work thus lends support to the two-domain model for ($\sqrt{3} \times \sqrt{3}$) Ag, since one can imagine its growth simply by replacing the Si adatoms with Ag atoms.

This structure is still very controversial, and these results thus cannot be called conclusive, but they further illustrate the way XPD can be used for such metal–semiconductor studies. This study is also state-of-the-art for XPD in that it

involves a large azimuthal data set, SSC–SW calculations with correct final-state interference, and the use of R factors[264] to judge goodness of fit. As one qualitative figure of merit in connection with this study, the minimum R factors of 0.14 found are about $\frac{1}{4}$ of those found in recent LEED studies of the same system.[117,118]

4.5. Supported Clusters

In this section, we briefly consider two examples of how higher-energy XPD has been used to study the formation of three-dimensional clusters on surfaces. (A third example has already been considered in the data for Fe deposited on Cu (001) shown in Fig. 24, where agglomeration effects are visible even for very low coverages.)

4.5.1. Ag/Si (111)

We have noted in the last section that Ag readily forms islands and three-dimensional clusters on the Si (111) surface if the coverage exceeds the 0.7–1.0 ML needed for the ($\sqrt{3} \times \sqrt{3}$) Ag structure. If these clusters are more than one atomic layer in thickness, then strong forward-scattering effects are expected for emitters in the lower layer(s) of the cluster. Such effects are illustrated in Fig. 30b,c, where polar scans of Ag $3d_{5/2}$ intensity have been measured first in Fig. 30c for a thick Ag reference layer of approximately 6 ML thickness, and then after heating to 450 °C so as to desorb all but an average coverage of about 2 ML. In Fig. 30c, a LEED pattern characteristic of the epitaxial Ag (111) that is known to grow on Si (111) is seen, and strong diffraction peaks due to buried-atom emission from this thick overlayer are found. In Fig. 30b, the Ag (111) LEED pattern is weakly present and there are still clear remnants of the photoelectron-diffraction features seen in the thick overlayer. Thus, such XPD patterns are very sensitive to the presence of three-dimensional islands.

The previous discussion of Figs. 22 and 23 also suggests that it might be possible to estimate the average thickness of such clusters up to about 5 ML, where the XPD features begin to converge to the bulk pattern. An additional type of information that could be very useful for some systems is the orientation of the cluster crystal axes with respect to the surface normal. In fact, even if clusters grow in a textured way (that is, without preferred azimuthal orientation), polar scans of the type shown here should permit determining whether there is any preferred vertical axis. Bullock and Fadley[50b,119] have also recently pointed out that, even for two-dimensional islands, it should be possible to use low-θ azimuthal scans to determine the island orientation and, for smaller islands, the average number of atoms present.

4.5.2. Pt/TiO$_2$

As a second example of cluster studies using XPD, Tamura et al.[120] have considered the interaction of Pt with three low-index faces of TiO$_2$, a system of interest in catalysis and for which the so-called strong metal-support interaction

(SMSI) can occur. In this study, Pt was deposited at room temperature to a mean thickness of about 10 ML onto the (110), (100), and (001) surfaces of TiO_2, and azimuthal XPD measurements were made at different polar angles for the Ti $2p$ and O $1s$ photoelectron peaks before deposition and for the Pt $4f$ peaks after deposition. Similar Pt $4f$ measurements were made after annealing the samples up to 800 K.

Some of these results are shown in Fig. 33a for the (110) surface at $\theta = 40°$ and Fig. 33b for (100) at $\theta = 45°$. Considering first Fig. 33a, we see that curves (i) and (ii) show weak diffraction features for both Ti $2p$ (clean) and Pt $4f$ (just after the deposition). The nonconstant background under these curves, particularly for (ii), is thought to be due to a nonuniform deposition over the region of the sample seen by the electron analyzer; thus, with changes in ϕ, a slightly different area and average Pt thickness might be seen. After the high-temperature anneal, the Pt $4f$ features in (iii) are strongly enhanced, with a concomitant increase in the anisotropy $\Delta I/I_{max}$ from 16% to 29%. This is consistent with the growth of thicker or larger clusters upon annealing, although (ii) indicates that some sort of ordering must be present even without annealing. Finally, (iv) shows a theoretical calculation based upon PW-cluster calculations with the effects of double scattering included. (The possible risk of including only double-scattering events has been mentioned already in section 3.2). The Pt clusters assumed had (111) orientation and contained 13 atoms in three planes; two symmetry-equivalent orientations with respect to the substrate 180° apart were considered. The resulting curve in (iv) is found to agree rather well with the annealed Pt $4f$ experimental results, suggesting that the clusters are growing with preferred (111) orientation.

A similar set of data for the (100) surface are shown in Fig. 33b. Here, (i) and (ii) exhibit strong diffraction from the O $1s$ and Ti $2p$ peaks of the substrate. Curve (iii) shows the strong diffraction of Pt $4f$ after the anneal. (A more uniform deposition of Pt has here made the background levels very flat.) Finally, curve (iv) is calculated for the same type of two-domain, three-layer Pt cluster [but with different assumed registry with the (100) surface], and it again shows good agreement with experiment, suggesting (111) orientation for the clusters on this surface as well.

For the third (001) surface studied, it is interesting that the Pt $4f$ oscillations were weak both before and after annealing, indicating a different kind of overlayer growth and/or a lower degree of cluster formation.

Together the three studies related to clusters that have been considered up to this point illustrate the utility of both polar and azimuthal XPD or AED data for studying the amount of cluster formation present and the average orientation and morphology of the aggregates formed. Two possible limitations of this kind of study are that XPD and AED average over all of the clusters present and so cannot easily be used to estimate the cluster-size distribution. In certain cases, it might even be difficult to detect the difference between, for example, a full 4-ML epitaxial overlayer and a collection of independent clusters with an average thickness of 4 ML, even if the crystallographic orientation could be easily determined. Although with careful measurements of both substrate and deposited-atom intensities before and after deposition and/or heat treatment, the
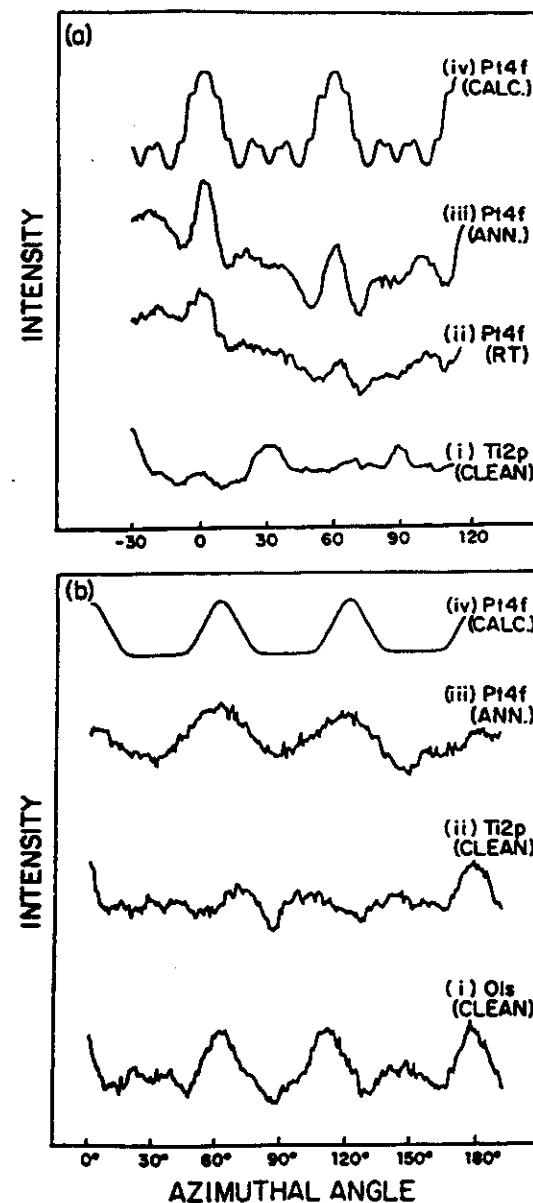
FIGURE 33. (a) Azimuthal XPD data for Pt $4f$ and Ti $2p$ emission from Pt on TiO_2 (110) at $\theta = 40°$ are compared to PW cluster calculations including double scattering for Pt emission from a (111)-oriented metal cluster of about 15 Å diameter. Al $K\alpha$ radiation was used for excitation. (b) As in (a) but for Pt $4f$, Ti $2p$, and O $1s$ emission from Pt on TiO_2 (100) at $\theta = 45°$. (From Ref. 120.)

implicit effects of "patching" in cluster growth should be evident in deposited-atom–substrate relative intensities. Simple formulas for analyzing such patched-overlayer relative intensities appear elsewhere.[9] It is also clear that combining XPD or higher-energy AED with scanning tunneling microscopy (STM) would yield a particularly powerful set of data for cluster and epitaxial growth studies. This is because STM can be used to measure directly both the cluster size distribution and the step and defect densities that are averaged over in XPD/AED. But it may be difficult or impossible with STM to see into a cluster or overlayer so as to determine its crystallographic orientation or thickness. This is because STM cannot probe below the surface density of states and also is not atom-specific.

4.6. Core Level Surface Shifts and Chemical Shifts

A further type of problem that has been studied by low-energy photoelectron diffraction using synchrotron radiation for excitation is metal core level surface shifts.[18,53,80,121,122] In particular, Sebilleau, Treglia et al.[18,53,80] have tuned the photoelectron energy to low values to achieve high surface sensitivity and have looked with high energy resolution at photoelectron diffraction from such surface-shifted core levels.

Some of their results for tungsten $4f$ emission from W (100) are illustrated in Fig. 34, where both the surface and bulk peaks are shown, together with their individual azimuthal diffraction patterns and corresponding SSC–PW theoretical curves. The two types of peaks clearly exhibit very different diffraction patterns, and both of these are rather well predicted by the SSC model, even at this quite low photoelectron energy of approximately 30 eV. It is remarkable that a single-scattering approach is so quantitative at such a low energy, and this may to some degree be fortuitous. However, later work by Treglia et al.[18c,53,80] has reached similar conclusions, with the only qualification being that it is necessary at such energies to use the correct final-state angular momenta, as expected from the discussion of Fig. 4 in section 3.1.2. For the low energy of this case, the $4f$-to-εd channel is assumed to be dominant.

This work thus illustrates the added ability of photoelectron diffraction to carry out independent structure determinations of physically or chemically different species of the same atom through core level shifts. These shifts are not limited to the clean-surface type considered above, but may also involve the well-known chemical shifts commonly seen when different chemical bonding or oxidation states are present. Such state-specific structure studies should be a very powerful probe of surface reactions, overlayer growth, and interface formation. They will, however, require very high energy resolutions of 0.3 eV or better to be fully effective in resolving small shifts.

As an obvious example for future work, it should also be possible to do state-specific diffraction studies on semiconductor surfaces, since both clean surfaces[123a,b] and chemically reacted surfaces[123c] exhibit shifted core levels characteristic of the different bonding sites and/or oxidation states.

One technologically important example of a semiconductor system for which more structural information concerning different chemical species would be useful
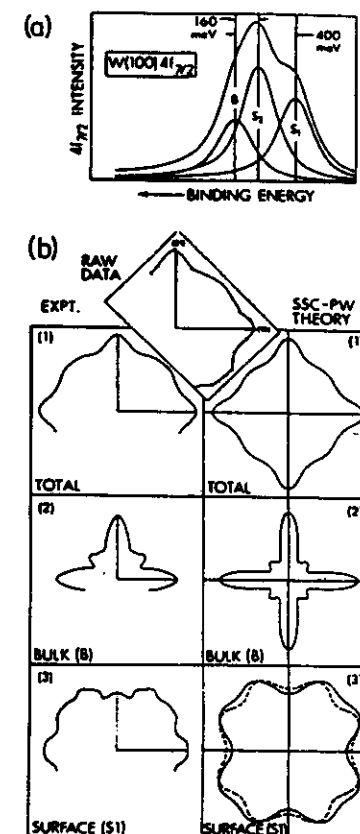
FIGURE 34. (a) A W $4f_{7/2}$ spectrum from W (001) at a kinetic energy of ~30 eV, showing two surface-shifted core levels (S_1 and S_2) as well as a bulk peak (B). (b) The azimuthal dependences of these intensities at a polar angle of 60° above the surface: (1) represents the total $4f_{7/2}$ intensity, (2) the bulk intensity (B), and (3) the surface intensity (S_1). SSC–PW calculations of these intensities are shown in (1'), (2'), and (3'), respectively. The inset represents raw data for the total intensity. (From Ref. 18(a).)

is the formation of the interface between SiO_2 and Si. Figure 35 shows high-resolution Si $2p_{3/2}$ core spectra obtained by Himpsel et al.[123c] from Si (100) and Si (111) surfaces that were thermally oxidized in UHV conditions (2.5 Torr O_2, 750° C, 20 sec) so as to produce a very thin 5-Å oxide film. The overall resolution here was 0.3 eV, and it is striking that all of the oxidation states of Si are clearly seen, from the elemental substrate to the 4+ dioxide. The different nature of the oxidizing surface for Si (111) is further found to lead to a suppression of the Si^{2+} state. These intermediate oxidation states are thought to be associated with the interface, and, from quantitative estimates of the different depth distributions of these states, it is concluded that an extended rather than abrupt interface is involved. Models of such an extended interface have been proposed by Himpsel et al., but these cannot be tested in detail without additional data. It seems clear that separately measuring the scanned-angle photoelectron diffraction patterns of the different oxidation states would provide some very useful information in this
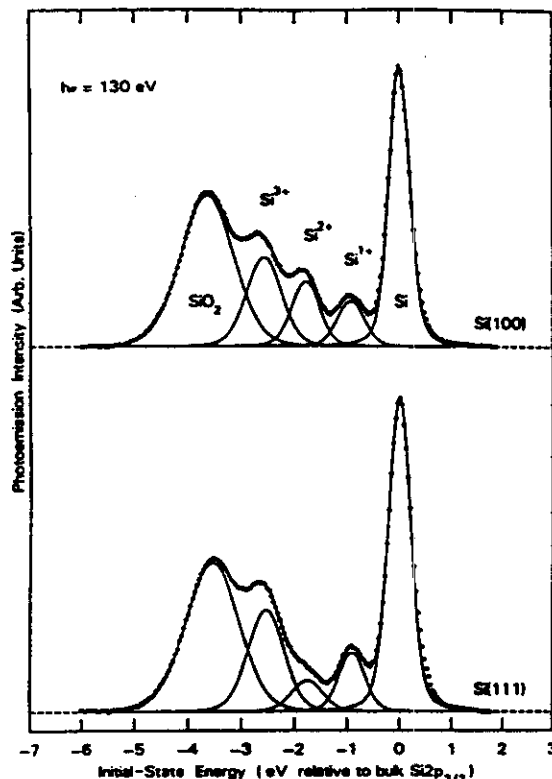
FIGURE 35. The Si $2p_{3/2}$ components of Si $2p$ spectra from thin oxide films of approximately 5 Å thickness thermally grown on Si (100) and Si (111) surfaces. Note the reduced intensity of Si^{2+} for Si (111), assumed to be due to structural differences in the interface. [From Ref. 123(c).]

direction, since each state is hypothesized to occupy one or at most a few distinct site types relative to the substrate lattice.

Although these are difficult experiments at present, the detailed state-by-state information derivable should help in unraveling the microscopic structures of many surface and interface systems. Being able to tune photon energy so as to vary surface sensitivity or to move on or off of resonant photoemission conditions would also be an advantage, as noted in prior studies.[123] Going to higher photon energy not only permits looking deeper into the material and assessing the relative depth distributions of the different species, but should also lead to more simply interpretable forward-scattering peaks for emission from interface-associated atoms. A disadvantage of higher energies is that the substrate signal tends to dominate the spectrum, but with high enough resolution and suitable reference spectra for subtracting the substrate signal, such high-energy measure-

ments should be possible. Synchrotron radiation will thus be necessary to fully exploit this potential for studying interface growth by state-specific photoelectron diffraction.

4.7. Surface Phase Transitions

We conclude this discussion of applications of photoelectron diffraction and Auger electron diffraction by considering briefly their possible use in studying various types of surface phase transitions such as surface premelting, roughening, or disordering at a temperature below the bulk melting temperature,[124] as well as surface reconstructions that are temperature-dependent.[123a,b] The short-range order and directional sensitivity of both PD and AED suggest that they should be useful probes of such surface phase transitions, which may involve changes in near-neighbor atom positions and/or the introduction of considerably more disorder in these positions. The number of such studies is still very small, but the most recent are quite promising.

An unsuccessful attempt at observing surface premelting for Cu (001) in grazing-emission XPD was made some time ago by Trehan and Fadley.[63a] For this surface, roughening and possibly faceting was observed before any evidence was seen in the XPD anisotropies of the extra disorder associated with surface melting. However, much more recently, evidence for surface phase transitions involving surface disordering and perhaps premelting has been seen in XPD from two separate systems: Pb (110) by Breuer, Knauff, and Bonzel[125] and Ge (111) by Friedman, Tran, and Fadley.[126]

For the case of Ge (111), prior LEED studies and theoretical modeling by McRae and co-workers[127] indicate that there is a reversible surface order–disorder transition at a temperature of 1060 K that is 0.88 times the bulk melting temperature. Is this transition visible in XPD? In Fig. 36, we show such XPD data in which the Ge $3d$ azimuthal anisotropy was monitored as a function of temperature. The polar angle of 19° chosen here causes the emission direction to sweep through nearest-neighbor forward-scattering directions in the unre-constructed surface, as shown in Fig. 27. This relatively low θ value also leads to higher surface sensitivity.

Figure 36a shows four azimuthal scans taken at temperatures from ambient to about 50 K above the transition. (Note the expected similarity of the azimuthal scan at ambient temperature to that for $Hg_{1-x}Cd_xTe$ (111) in Fig. 26a.) As the temperature is increased, the azimuthal curves gradually lose much of their fine structure, and upon passing above the transition point, only two main peaks remain in the azimuths $[1,1,-2]$ ($\phi = 0°$) and $[-1,2,-1]$ ($\phi = 60°$). In Fig. 36b, the intensity of the $[1,1,-2]$ peak corresponding to nearest-neighbor scattering is plotted against temperature, and it is clear that an abrupt drop occurs over the interval 850–1050 K. This drop furthermore cannot be explained by simple Debye–Waller modeling.

McRae et al.[127a] have measured the intensities of several LEED beams for the same system as a function of temperature, and their data is similar to Fig. 36b in that the intensities drop sharply toward 1060 K and level off thereafter. Some of the LEED intensities drop more rapidly than the curve of Fig. 36b near 1060 K;
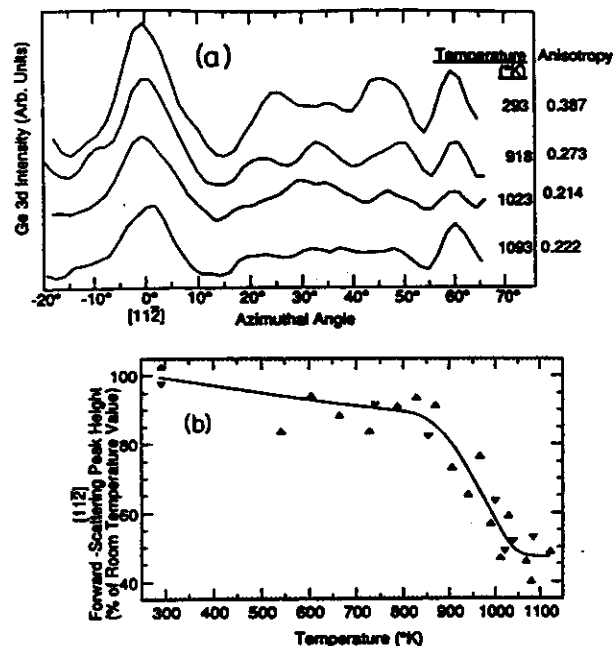
FIGURE 36. Temperature-dependent azimuthal XPD data for Ge 3d emission at 1458 eV from Ge (111) at low takeoff angle of $\theta = 19°$. This θ value corresponds to scanning through nearest-neighbor scattering directions for $\phi = 0°$, as shown in Fig. 27. (a) Four azimuthal scans at temperatures from ambient to above the order-disorder transition. (b) The detailed temperature dependence of the height of the peak along $\phi = 0°$. 1060 K is where a prior LEED study (Ref. 127(a)) has seen evidence for a surface-disordering transition. Upright triangles represent increasing temperature; inverted triangles, decreasing temperature. (From Ref. 126.)

some have a form very similar to this curve. Thus, it can be concluded that the same transition is observed in both sets of data, even though the LEED measurement is expected to be sensitive to longer-range order on a scale of approximately 100 Å, whereas XPD should probe distances on the order of 10–20 Å.

Although these XPD results have not as yet been analyzed in detail so as to derive additional structural information, it is clear that obtaining both polar and azimuthal data at temperatures below and above the transition temperature and comparing the diffraction structures seen with calculations for different types of disorder models should yield a better understanding of this and other surface phase transitions.

Similar abrupt changes in polar-scan diffraction anisotropies have also been seen by Breuer et al.[125] for the surface disordering of Pb (110), which has been observed previously with Rutherford backscattering and low-energy electron diffraction.[128]

As one interesting future direction for such work, the study of surface phase transitions should also benefit greatly from doing separate diffraction measurements on the various core peaks observed. For example, the Ge (111) surface exhibits one bulk peak and two surface peaks[123a,b] that could all be studied separately. However, the small shifts of only about 0.3–0.7 eV involved here would require very-high-resolution data and the use of curve-deconvolution procedures.

5. FUTURE DIRECTIONS

5.1. Measurements with High Angular Resolution and Bragg-like Reflections

As noted previously, most prior PD and AED measurements have been carried out with resolutions of at best a few degrees in half angle. In many systems, the acceptance solid angle is also not a simple cone, but may have different dimensions along two perpendicular axes.[29] For future work, the question thus arises as to what additional information might be gained by going to much better conic resolutions of, for example, $\pm 1.0°$.

As discussed in section 2, various methods exist for limiting angular spreads upon entry into the analyzer, but one which has the advantages of being very certain in its limits and operationally very convenient is the insertion of externally selectable angle-defining tube or channel arrays between sample and analyzer entry. The use of such channel arrays has been discussed by White et al.,[33] and they have been used to precisely limit angles to $\pm 1.5°$ or better (that is, $<\frac{1}{4}$ of typical prior solid angles).

We have already discussed two examples of this kind of data: for NiO grown on Ni (001) in Fig. 14 and for $c(2 \times 2)$ S on Ni (001) in Fig. 17. For these cases, we have pointed out the greater sensitivity to the degree of short-range order and the adsorbate position, respectively.

As a final example of the dramatic effects seen in going to high angular resolution, we compare in Figs. 37a and b low- and high-resolution XPD data obtained by Osterwalder, Stewart et al.[46] for Ni $2p_{3/2}$ emission from a clean Ni (001) surface at $\theta = 47°$. A great deal more fine structure is seen in the data with $\pm 1.5°$ resolution, and the form of the fine structure for $\phi = 25°$–$65°$ is in fact completely changed due to a lower degree of angular averaging over such structures. Very narrow features of only a few degrees at FWHM are also seen in the results at high resolution.

Figure 37c summarizes a more complete set of such high-resolution azimuthal data for Ni $2p_{3/2}$ that represents the most detailed investigation of XPD fine structure to date. Here, the polar angle of emission was varied in 1° steps from $\theta = 40°$ to $50°$, passing through the high-symmetry value of $\theta = 45°$ which contains the $\langle 110 \rangle$ directions of nearest-neighbor scattering in its ϕ scan. Full 360° scans were used to generate each curve, and fourfold averages of this data into one quadrant shown elsewhere[10,46] agree excellently with the single-quadrant results presented here. This three-dimensional plot makes it clear that high-energy electron diffraction features can change extremely rapidly with either θ or
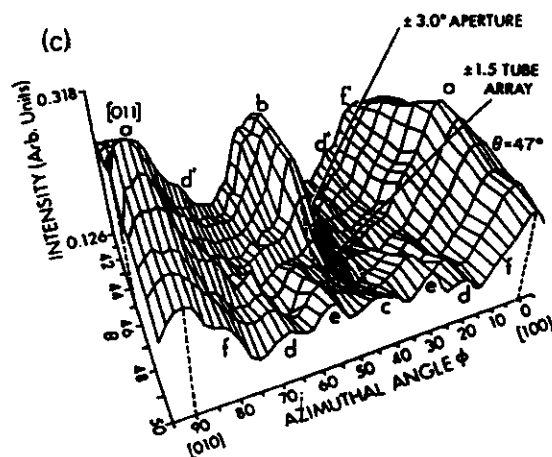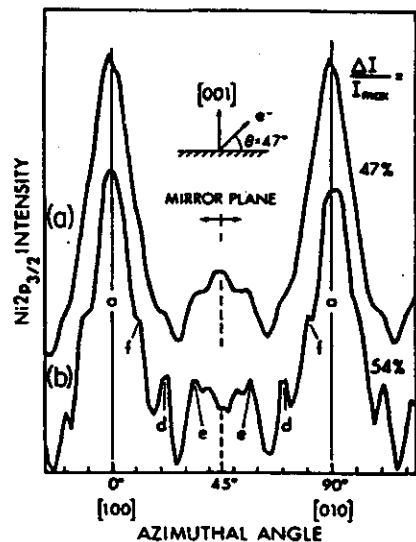
FIGURE 37. Effect of increasing angular resolution on Ni $2p_{3/2}$ azimuthal XPD data from a clean Ni (001) surface at 632 eV. (a) and (b) show single scans at $\theta = 47°$ with resolutions defined by a single aperture of nominal ±3.0° acceptance and a tube array yielding ±1.5° or less, respectively. (c) a three-dimensional summary of a series of single-quadrant high-resolution Ni $2p_{3/2}$ scans with a ϕ step of only 1°. The regions averaged over with the two different angle-defining devices in (a) and (b) are shown as shaded. (From Ref. 48.)
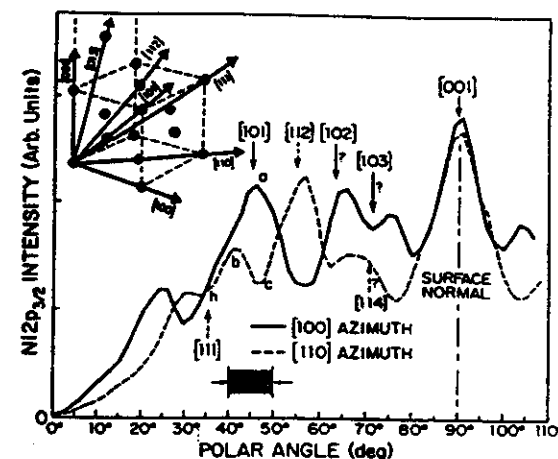

FIGURE 38. High-resolution Al Kα polar scans of Ni $2p_{3/2}$ intensity above Ni (001) in two different azimuths, with certain low-index directions and special points noted [cf. lower-case letter labeling in Fig. 37(c)]. The region covered by Fig. 37(c) is shaded. The inset shows the near-neighbor/low-index directions within an fcc unit cell. (From Ref. 48.)

ϕ. These results also qualitatively explain how the approximately ±3.0° averaging in Fig. 37a yields features for $\phi \approx 25°$–65° that are so different from those for the high-angular-resolution curve in Fig. 37b. That is, Fig. 37a represents an average over all of the curves in Fig. 37c from $\theta = 44°$ to $\theta = 50°$, as bounded by the lighter-shaded elliptical area, and the steeply rising ridge toward $\theta = 44°$ thus accounts for the peak seen at $\phi = 45°$ with lower resolution. The results in Fig. 37b, by contrast, represent an average over only the darker-shaded area in Fig. 37c, and so retain a minimum at $\phi = 45°$.

Figure 38 shows two high-resolution polar scans from the same study of Ni (001). The unit cell of the metal and various near-neighbor scatterers along low-index directions is also indicated to permit judging how well various strong features correlate with them (cf. also Fig. 22a). These polar scans also show considerable extra fine structure, for example, as compared to the same sort of [100] polar scan for higher-energy Auger emission from bulk Cu (001) shown in Fig. 22b. These high-resolution data are found to exhibit peaks for emission along some, but not all, of the near-neighbor directions shown. Peaks are found at positions corresponding closely to the nearest neighbors (and fourth-nearest neighbors) along [101], the second neighbors along [001], and the third neighbors along [112]. However, minima and/or significant peak shifts are seen for the fifth neighbors along [103] and the sixth neighbors along [111]. Neighbors even further away along [102] and [114] are also found to show significant shifts compared with the observed peaks. In particular, the [111] direction corresponds to a local minimum (indicated as point h), with enhanced intensity on either side of the minimum; a ϕ scan through [111] at $\theta = 35°$ shows the same sort of profile. As noted previously in the discussion of Fig. 22, this is due to the influence of higher orders of interference[71] and perhaps multiple scattering effects.[73] Thus, we conclude that the first 3–4 spheres of neighbors in any lattice will probably produce strong and simply interpretable forward scattering peaks. Beyond these spheres, more-complex origins will require modelling at least at the SSC–PW level for interpretation.

Three-dimensional data of the type shown in Fig. 37c have also been obtained at lower angular resolution by Baird, Fadley and Wagner for XPD from

Au (001)[129] and by Li and Tonner for high-energy AED from Cu (001).[29] These two data sets span a high fraction of the 2π solid angle above these two surfaces, and they exhibit very similar intensity contours, as expected since they both represent high-energy emission from the same fcc crystal structure. The more recent data of Li and Tonner serves as a more accurate reference for the overall features of such fcc XPD/AED patterns at lower angular resolution. These studies also agree with the preceding paragraph and the discussion of section 4.3.2 in seeing simple correlations of peaks with near-neighbor forward-scattering directions out only to the fourth shell, with directions such as [111], [114], [102], and [103] showing more complex behavior.

The Ni data discussed here and the other high-resolution results discussed previously thus make it clear that, at least in higher-energy XPD and AED, using resolutions that are much worse than ±1.0° will blur out some features and lead to a loss of structural information. Such sharp features are generally the result of superpositions of several scattering events, since the relevant scattering factor by itself exhibits nothing narrower than the forward scattering peak of some 20–25° FWHM. These features also tend to involve scatterers further away from the emitter and thus to be associated with the degree of short-range order around the emitter. (This is nicely illustrated by the NiO/Ni (001) results of Fig. 14.) Thus, there is little doubt that XPD or AED with high resolution will contain more fine details of the structure under study.

At lower energies, by contrast, one expects generally wider features due to the broader, more diffuse scattering factors involved (cf. Fig. 2) and the larger de Broglie wavelengths that spread out different orders of interference (cf. the curves in Figs. 4 and 5). However, even for such energies, it is possible for superpositions of multiple events to produce rather narrow features, and high resolution might also be a benefit in this case.

The most obvious disadvantage of working at high angular resolution is the longer data-acquisition times, which may be 10–30 times those of typical low-resolution operation.[33] A second disadvantage is that it is likely that the effects of multiple scattering will tend to be averaged out somewhat in lower-resolution data because of cancellations of phases in the many events involved.[21] Conversely, in high-resolution data, such MS effects may be more important, even though the information content is inherently greater.

A further aspect of the relationship of such high-resolution data to more complex interference effects and more distant neighbors is the influence of Bragg-like diffraction effects from planes in multilayer substrate emission. In the presence of the strong inelastic damping characteristic of both PD and AED, such Bragg-like events lead to what has been termed a Kikuchi-band model of these phenomena.[2,3,63b,129,130] Although a fully quantitative Kikuchi-band theory of higher-energy PD or AED based upon the superposition of many Bragg-like scattered waves is lacking, simple model calculations have been carried out by Baird et al.,[129] by Goldberg et al.,[130] and more recently also by Trehan et al.,[63b] and they are found to semiquantitatively reproduce the results of XPD measurements on both Au (001) and Cu (001). In particular, the superposition of several Kikuchi bands along low-index directions yields the forward-scattering peaks seen in both experiment and SSC calculations.

More interestingly, there are features in experimental data at high angular resolution that appear to be associated with specific Bragg events from low-index planes (such as features d and f in Fig. 37b here and as discussed in connection with Fig. 31 of Ref. 9). This suggestion has been given more quantitative support in a recent high-resolution study of Ni (001) by Osterwalder et al.[48a] Furthermore, calculations with the SSC model exhibit these same Bragg-like features if the cluster size is permitted to be large enough and/or the inelastic damping is sufficiently reduced,[48a,63b] thus verifying that a cluster-based theory can be used for problems varying from short-range order to long-range order.

This formal equivalence of the SSC model and the Kikuchi-band picture for describing bulk-like multilayer emission was first pointed out some time ago,[9,42,130] but additional clarification seems appropriate in view of misleading statements concerning the role of the Kikuchi model in the interpretation of XPD and AED that have nonetheless appeared in the more recent literature.[11] From an experimental point of view, the essentially identical intensity profiles for LMM Auger electron diffraction and backscattered LEED "Kikuchi patterns" from Ni (001) at 850 eV observed by Hilferink et al.[70a] provide a particularly clear verification of this equivalence. From a theoretical point of view, the relationship of the two approaches, if both are carried to comparable quantitative accuracy, is analogous to the equivalence of the so-called short-range-order and long-range-order theories of EXAFS, as discussed elsewhere.[63b,131] It is clear, however, that the SSC and MSC approaches are of greater generality in that they can be applied to both surface- and bulk- emission and to problems of differing degrees of order. The Kikuchi-band picture is, by contrast, formulated on a basis of inelastically attenuated Bloch states that reflect long-range translational order. Thus, the cluster-based theories are inherently more rapidly convergent and are more appropriate ways to look at near-surface diffraction from adsorbates and thin overlayers, as noted previously.[42,130] But it is absolutely incorrect to say that the ability of the cluster approach to explain forward-scattering features makes the Kikuchi-band model invalid for describing substrate emission.[11]

In summary, the use of high angular resolutions on the order of ±1.0° should permit even more precise structural conclusions to be derivable from both photoelectron diffraction and Auger electron diffraction, especially at energies of >500 eV. Such data should contain information on neighbors further away from the emitter, including features related to Bragg-like scattering events. It is also clear that the use of resolutions of ±3.0° or worse may conceal a great deal of fine structure inherent in the experimental curves.

5.2. Spin-Polarized Photoelectron and Auger Electron Diffraction

Beyond increasing both the energy resolution and the angular resolution in PD and AED as means of deriving more detailed structural information, we can also ask what is to be gained if the last property of the electron, its spin, is also somehow resolved in the experiment. This prospect has so far been considered quantitatively and observed experimentally only in the case of photoelectron diffraction, but we return at the end of this section to comment on how it might also be possible in Auger electron diffraction.

In the first attempts at what has been termed spin-polarized photoelectron diffraction (SPPD), the fundamental idea has been to use core-level multiplet splittings to produce internally referenced spin-polarized sources of photoelectrons that can subsequently scatter from arrays of ordered magnetic moments in magnetic materials. Figure 39a illustrates how such a splitting can give rise to spin-polarized photoelectrons for $3s$ emission from high-spin Mn^{2+}. The splitting is intra-atomic in origin and arises from the simple LS terms of ^5S and ^7S in the final ionic state of Mn^{+3} with a $3s$ hole.[132] The net effect is to cause the peaks in the doublet to be very highly spin-polarized, with ^5S predicted to be 100% spin-up and ^7S to be 71% spin-down relative to the net $3d$ spin of the emitting atom.[133,134] The relatively large exchange interaction between the highly overlapping $3s$ and $3d$ electrons is responsible for the easily resolvable splitting of 6.7 eV between the ^5S and ^7S final states of the photoemission process.

The basic experiment in SPPD thus involves looking for spin-dependent scattering effects that make two such peaks behave slightly differently in the presence of a magnetically ordered set of scatterers. Such effects were first discussed theoretically by Sinkovic and Fadley,[134a] and they have several special properties:[135,136]

* There is no need for any kind of external spin detector beyond an electron spectrometer capable of resolving the two peaks in energy.
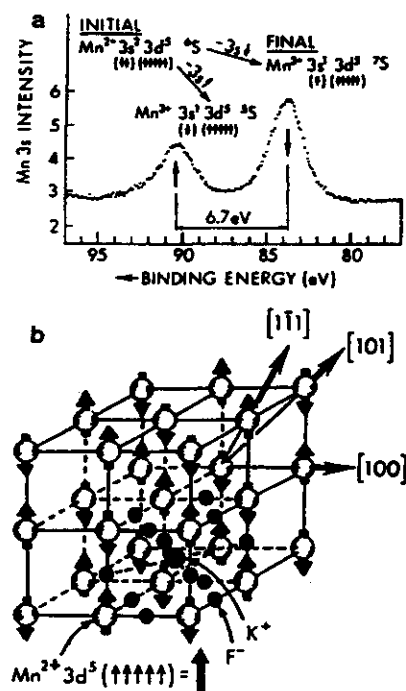
FIGURE 39. (a) The Al $K\alpha$-excited Mn $3s$ spectrum of KMnF₃, with the initial and final states leading to the multiplet splitting indicated, together with the predominant photoelectron spin expected in each peak. (b) The crystal structure of KMnF₃, with the antiferromagnetic ordering of the Mn²⁺ spins also indicated. [From Ref. 134(a).]

* The fact that the photoelectron spins are referenced to that of the emitting atom or ion means that SPPD should be capable of sensing magnetically ordered scatterers even when the specimen has no net magnetization. Thus, studies of both ferromagnetic and antiferromagnetic materials should be possible, and meaningful measurements should also be feasible above the relevant macroscopic transition temperatures (Curie or Neel temperatures, respectively). For the latter case, the photoelectrons in each peak would be unpolarized with respect to any external axis of measurement but still polarized relative to the emitting atom.

* The photoelectron emission process is also very fast, with a time scale of only about 10^{-16} to 10^{-17} seconds; thus, such measurements should provide an instantaneous picture of the spin configuration around each emitter, with no averaging due to spin–flip processes, which are much slower at roughly 10^{-12} seconds.

* Finally, the previously discussed strong sensitivity of any form of photoelectron diffraction to the first few spheres of neighboring atoms means that SPPD should be a probe of short-range magnetic order (SRMO) in the first 10–20 Å around a given emitter. Thus, provided that a sufficiently well-characterized and resolved multiplet exists for a given material, this technique has considerable potential as a rather unique probe of SRMO for a broad variety of materials and temperatures.

Before discussing the first observations of such spin-dependent scattering and diffraction effects, it is appropriate to ask to what degree final-state effects such as core-hole screening may alter or obscure these multiplets. We note first that the cases of principal interest in SPPD are outer core holes, which are more diffuse spatially than inner core holes and for which the interaction with the surrounding valence electrons is thus not as strongly polarizing as for inner core holes (which can often be very well described in the equivalent-core approximation). Nonetheless, it has been suggested by Veal and Paulikas[137] that both screened and unscreened multiplets corresponding to $3d^{n+1}$ and $3d^n$ configurations, respectively, are present in the $3s$ spectra of even highly ionic compounds such as MnF_2.

As such effects would make the carrying out of SPPD measurements more difficult (although still certainly not impossible) due to the potential overlap of peaks of different spin polarization, Hermsmeier et al.[138] have explored this problem in a study of Mn $3s$ and $3p$ multiplets for which the experimental spectra from several reasonably ionic solid compounds have been directly compared to the analogous spectra from gaseous Mn, a simple free-atom system in which no extra-atomic screening can occur. In Fig. 40, we show their compilation of $3s$ spectra for the diluted magnetic semiconductor $Cd_{0.3}Mn_{0.7}Te$ (a), single-crystal MnO with (001) orientation (b), polycrystalline MnF_2 as obtained some time ago by Kowalczyk et al.[139] (c), gaseous atomic Mn (d), and a free-ion theoretical calculation of these multiplets by Bagus et al. including configuration interaction, but totally neglecting extra-atomic screening (e).[140] From a consideration of the experimental data only, it is striking that for both $3s$ multiplets and $3p$ multiplets (not shown here, but discussed in Ref. 138) the solid-state spectra are very similar to the gas-phase spectra, with the only differences being some extra broadening in the solid state and some small changes in peak positions that are not at all surprising. Thus, even without resorting to theory, it seems clear that these
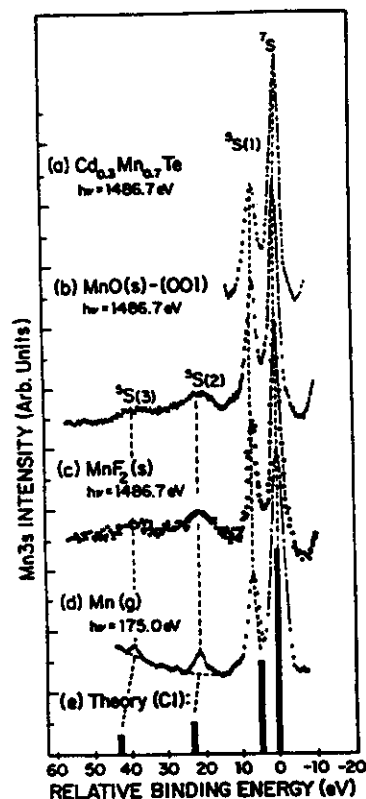
FIGURE 40. Experimental Mn 3s spectra for (a) the diluted magnetic semiconductor $Cd_{0.3}Mn_{0.7}Te$, (b) MnO (001), (c) polycrystalline MnF_2 (Ref. 139), and (d) gaseous atomic Mn are compared to (e) theoretical calculations for emission from a free Mn^{2+} ion including final-state configuration interaction (Ref. 140). (From Ref. 138.)

spectra are very free-atom–free-ion like, and that a simple multiplet interpretation such as that in Fig. 39a should rather accurately describe the spin polarizations of the photoelectrons involved.

If we consider now the best available free-ion theoretical prediction for the 3s spectra, this conclusion becomes even more convincing. In Fig. 40e, the results of a calculation by Bagus, Freeman, and Sasaki[140] for Mn^{3+} with a 3s hole and limited configuration interaction (CI) are shown. There is excellent agreement with experiment not only for the two dominant members of the multiplet that would be most useful in SPPD, but also for the two much weaker satellites that directly result from including CI. Similar conclusions are reached in a comparison of experiment and theory for analogous 3p spectra.[138] We thus conclude that extra-atomic screening does not cause a major perturbation of these multiplet splittings and thus also that outer core holes such as 3s and 3p should exhibit relatively free-atom–free-ion like multiplets for a variety of high-spin systems. Such multiplets in turn should be useful as spin-resolved sources in SPPD.

Direct experimental evidence of spin polarization in core spectra also exists. A recent measurement with an external spin detector of the spin polarization over the 3p peak from ferromagnetic Fe by Kisker and Carbone[141] yields significant spin-up polarization at lower kinetic energy and spin-down polarization at higher kinetic energy that are in the same sense as those expected for a simple 3p multiplet.[138] These results thus suggest that SPPD should be possible with ferromagnetic metals as well, particularly on the simpler and more widely split 3s peaks.

Returning now to a consideration of the SPPD experiments carried out to date, we have shown in Fig. 39b the crystal structure of the first material for which such effects were observed: a (110)-oriented sample of the simple antiferromagnet $KMnF_3$. It is clear from this that the relative spins of the emitter and the first scatterer encountered can be different for different directions of emission, as for example, between [100] and [101]. Spin-dependent scattering effects were first observed for this system by Sinkovic, Hermsmeier, and Fadley[142] as small changes of up to about 15% in the ratios of the $^5S(1)$ (spin-up) and ^7S (spin-down) peaks in the dominant doublet shown in Fig. 39a. For this study, a lower energy of excitation of 192.6 eV (Mo Mζ radiation) was used in order to yield lower-energy photoelectrons at approximately 100 eV, which are expected to exhibit significant spin-dependent effects in scattering.[134a] This requirement of low kinetic energies thus makes SPPD inherently well suited to synchrotron radiation with its tunable energy.

The $^5S(1):{^7S} = I(\uparrow)/I(\downarrow)$ intensity ratio was found to be sensitive to both direction of emission (as qualitatively expected from Fig. 39a) and temperature. Its variation with temperature is furthermore found to exhibit a surprisingly sharp transition at a point considerably above the Neel temperature (T_N), as shown in Fig. 41a. Here, we plot a normalized intensity ratio or "spin asymmetry" S_{expt} that is measured relative to the value of $I(\uparrow)/I(\downarrow)$ at a limiting high-temperature (HT) paramagnetic limit. This asymmetry is defined in the inset of Fig. 41a; it goes to zero at high temperature.

The abrupt high-temperature change observed in S_{expt} has been suggested to be due to the final destruction of the short-range magnetic order that is expected to dominate in producing such spin-polarized photoelectron diffraction effects. Note also that the short-range-order transition temperature T_{SR} at which this occurs is approximately $2.7 T_N$.

In an important confirmation and extension of this earlier work, very similar SPPD effects have also more recently been observed by Hermsmeier et al. for (100)-oriented MnO,[143] and two of their curves for the temperature dependence of the spin asymmetry are shown in Fig. 41b. As for $KMnF_3$, there is a relatively sharp change in the $^5S(1):{^7S}$ ratio at a temperature that is again well above the long-range-order transition temperature at $T_{SR} = 4.5 T_N$. For both $KMnF_3$ and MnO, it is also interesting that the form of the short-range order transition is very sensitive to emission direction, being steepest for the nearest-neighbor scattering direction in Fig. 41a and changing sign with only a 15° shift of emission direction in Fig. 41b. This sensitivity to direction is qualitatively consistent with single-scattering calculations of the spin-dependent exchange-scattering processes that may be involved.[134,143,144]
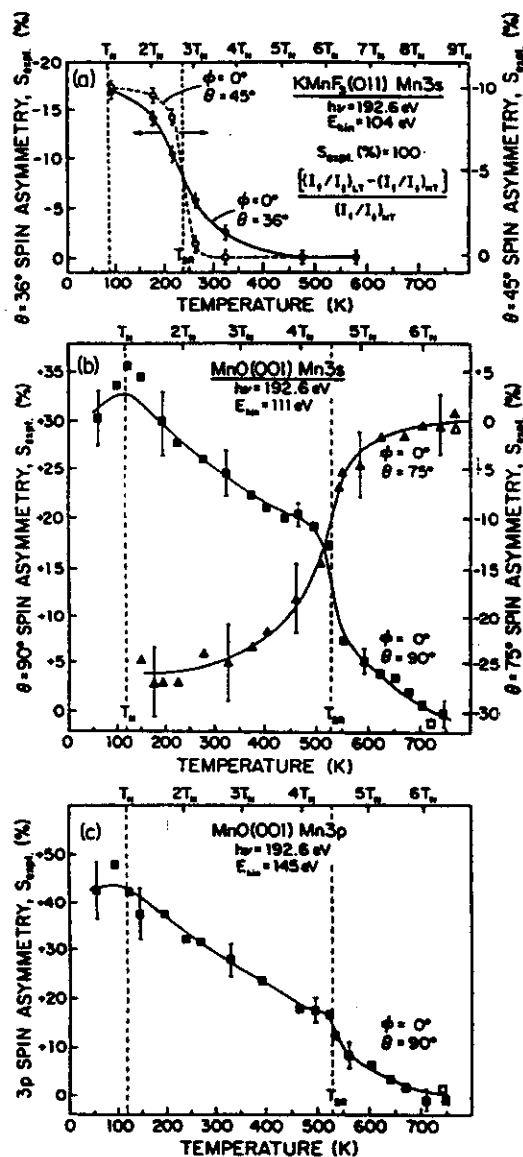
FIGURE 41. Spin-polarized photoelectron diffraction data indicating the presence of a high-temperature transition in antiferromagnetic short-range order. (a) Experimental spin asymmetries for the Mn 3s doublet from KMnF$_3$ with (110) orientation, as a function of temperature. Mo Mζ radiation at 192.6 eV was used for excitation to photoelectron energies of approximately 100 eV. The spin asymmetry is defined in the inset, where $I(\uparrow)/I(\downarrow)$ is the ratio of spin-up (^5S) to spin-down (^7S) intensities. HT refers to the highest temperature of measurement. Data are shown for two emission directions, one of which is along the [100] nearest-neighbor direction and the other 9° away from this. (From Ref. 142.) (b) As in (a), but for Mn 3s emission from MnO with (001) orientation. Note the different signs of the spin asymmetries for this case. (From Ref. 143.) (c) As in (b), but for Mn 3p emission from MnO with (001) orientation and treating the spin-up (^6P) and spin-down (^7P) peaks. (From Ref. 143.)

Although we have discussed only 3s emission thus far, the more complex 3p multiplets also should be spin polarized.[138,143] And in fact, a very similar transition has also been seen for MnO in the more widely split $^5P(1):^7P = I(\uparrow)/I(\downarrow)$ doublet at the same temperature T_{SR},[143] as shown in Fig. 41c. The fact that the same sort of transition is seen for these two peaks in spite of the fact that they are different from $^5S(1):^7S$ in both energy separation and mean kinetic energy provides strong support for the conclusion that this is a new type of magnetic transition.

It is also interesting that the T_{SR} values are, for both cases, approximately equal to the Curie–Weiss temperatures of the two materials, a connection which may be associated with the fact that this constant is proportional in mean-field theory to the sum of the short-range magnetic interactions.[145]

A final observation concerning this data is that the results for MnO in Figs. 41b and c show a possible indication of sensitivity to the long-range-order transition at T_N, as both curves possess a weak peak at T_N which is just outside of the estimated-error bar of the ratio measurement. If this is true, it is perhaps not surprising in view of the longer-range sensitivity of PD to neighbors that may be 20 Å from the emitter, as discussed in connection with both Figs. 16 and 20b.

A number of questions are thus raised by these results concerning the nature of short-range order above the long-range-order transition temperature and the way in which such effects can be incorporated in a spin-polarized variant of photoelectron diffraction theory. Although a quantitative theory of all aspects of the short-range-order transition and its inclusion in a spin-dependent modeling of the diffraction process does not yet exist, results in qualitative or semiquantitative agreement with experiment have been obtained in a few previous studies.[134,136,143,144]

The observation that Auger spectra from ferromagnetic materials exhibit strong spin polarization from one part of the manifold of features to another by Landolt and co-workers[146] also suggests that spin-polarized Auger electron diffraction (SPAED) should be possible. The more complex nature of Auger spectra in general will make the a priori prediction of the type of spin polarization more difficult, but for ferromagnets with net magnetization, an external spin detector could be used to first calibrate the spectrum for polarization.[146] Then, measurements of spin-up–spin-down ratios as functions of direction and/or temperature could be taken in the same way as for the spin-split core multiplets in SPPD. Even in antiferromagnetic systems with equal numbers of up and down 3d moments so that external calibration is impossible, any transition involving the polarized 3d valence electrons might be expected to show a net polarization that would again be internally referenced to the emitter.

A final aspect of such spin-polarized studies is to make use of left or right circularly polarized radiation, in conjunction with spin–orbit interaction in the energy levels involved, to preferentially excite one or the other spin polarization, as discussed recently by both Schuetz and co-workers[147] and Schoenhense and co-workers.[148] The use of such radiation already has produced very interesting spin-polarized NEXAFS and EXAFS structure from ferromagnets and ferrimagnets[147] and circular dichroism angular distributions (CDAD) from nonmagnetic surfaces and adsorbates.[148] In CDAD for light elements with negligible spin–orbit effects,

no net spin polarization of the photoelectron flux is involved, but such measurements provide the interesting possibility of measuring the contributions of individual m_l components to photoemission and photoelectron diffraction.[148] The CDAD studies require lifting the degeneracy of the m_l sublevels, and so have been carried out on valence levels; however, with very high energy resolution, it might be possible to do similar measurements on outer core levels with, for example, small crystal-field and/or spin–orbit splittings present.

With the availability of higher-intensity sources of circularly polarized radiation from next-generation insertion devices, it should be possible to greatly expand both of these kinds of study so as to look in more detail at both the angle and the energy dependence of the photoelectron intensities. For example, spin-polarized EXAFS requires measuring very accurately the differences in absorption for right and left polarizations, because the overall effects may be as small as a few times 10^{-4} in K-shell absorption.[147] However, studying L_2- and L_3-absorption for heavier elements with $Z \gtrsim 60$ leads to considerably larger effects, that can be on the order of 10^{-3}–10^{-2}. Extending this to do SPPD would thus imply measuring similarly accurate ratios or differences of photoelectron intensities. In this case, the magnitudes of the photoelectron spin polarizations are only on the order of 1% for K-shell emission, but for heavier elements, they can be up to 40–50% in L_2 emission and 20–25% in L_3 emission.[147] The latter two cases are thus about $\frac{1}{3}$–$\frac{1}{2}$ as highly polarized sources as a high-spin multiplet such as that in Fig. 39a. One advantage of such an approach would be to expand such studies to cases for which a suitable high-spin multiplet is not available. A disadvantage is that an external axis of polarization is involved, so that only ferro- or ferrimagnetic specimens could be studied. However, in CDAD experiments, this last restriction is not present.[148]

SPPD is thus a very new area of photoelectron diffraction, but it has considerable potential for providing information on the short-range spin order and spin–spin correlation functions around a given type of emitter site in the near-surface region of magnetic materials. Other antiferromagnetic and also ferromagnetic materials are currently being studied in order to better establish the systematics of the short-range-order transition and the range of utility of this method. Spin-polarized Auger electron diffraction and other measurements making use of circularly polarized radiation for excitation also should be possible.

5.3. Synchrotron Radiation–Based Experiments

Looking ahead to the much more intense and/or much brighter synchrotron radiation sources in the VUV/soft X-ray region that are currently either coming into operation or being conceived as next-generation devices based upon undulators or wigglers, one can see much-expanded possibilities for all of the types of photoelectron diffraction measurements discussed up to this point.

Measurements with both high-energy resolution (to distinguish different surface layers or chemical states as shown in Figs. 34 and 35, respectively) and high angular resolution (to enhance fine structure and thus structural sensitivity) should be possible. For some types of experiments (e.g., with maximum surface sensitivity and/or with spin-polarized diffraction in mind), lower photoelectron

energies of approximately 50–100 eV may be necessary, but for much structural work, energies of 1000 eV or even higher will be beneficial in yielding strongly peaked forward scattering and more nearly single-scattering phenomena. Being able to go to much higher photoelectron energies of up to 5000–10,000 eV may also be of interest in yielding even narrower forward-scattering peaks (as considered from a theoretical viewpoint by Thompson and Fadley[149]), more true bulk sensitivity via the longer electron attenuation lengths, and simpler theoretical interpretation. Being able to tune energy is also essential for the scanned-energy or ARPEFS experiments; it should be possible to carry these out much more rapidly and over a broader energy range above threshold. The polarization vector can also be oriented in either scanned-angle or scanned-energy measurements so as to enhance the contributions of various important scatterers (cf. Figs. 3a and 18). And we have already considered in the last section the possibility of using circularly polarized radiation. Finally, photoelectron *microscopy* with resolutions on the order of 500 Å or less is currently being developed,[150] and the additional dimension of using simultaneous photoelectron diffraction to probe the local atomic structure in such a small spot is quite exciting.

Auger electron diffraction may not benefit as much from synchrotron radiation, because excitation can be achieved with either photons or electrons and because the spectral form is not dependent on the excitation utilized if the initial hole is formed well above threshold. However, even for this case, synchrotron radiation could provide a more intense and less destructive excitation source than, for example, an electron beam or a standard X-ray tube. Also, it would be interesting to look at the diffraction process as the excitation energy is swept through threshold, so as to yield a purer one-hole initial state.

5.4. Combined Methods and Novel Data-Analysis Procedures: Photoelectron Holography?

It is clear from the foregoing examples that both scanned-angle and scanned-energy photoelectron diffraction measurements can provide useful information concerning surface structures, but that scanned-angle measurements are simpler in general to perform. Going to higher energies leads to easily interpretable forward-scattering features for many systems, but at the same time provides little information on the atoms that are below or behind the emitting atom as viewed from the detection direction. Thus, there are clear advantages to using lower energies as well, even if these lead to a potentially greater influence of multiple scattering. In the scanned-energy ARPEFS work discussed in sections 4.2.2 and 4.2.3, a major reason why interlayer spacings down into the bulk were derivable is that these lower energies exhibit the strongest backscattering effects and provide the largest oscillations in the $\chi(k)$ curves (cf. Fig. 20).

It is thus easy to suggest that the ideal photoelectron diffraction experiment based upon present methodology would consist of carrying out both high-energy measurements at kinetic energies greater than approximately 500 eV and low-energy measurements at approximately 50–100 eV. Being able to scan $h\nu$ would also be desirable, but not essential. A typical structure could then be analyzed by first making scanned-angle measurements at high energy and using the real-space

aspects of any forward-scattering effects to narrow down the range of possible structures (cf., for example the discussion of Figs. 29 and 30). Combining scanned-angle measurements at high and low energies then should permit determining structures in detail, including atomic positions both below and above the emitter in the sense mentioned above. Or scanned-energy measurements could be performed as a second step as well, leading to the utility of Fourier transform methods for narrowing down the number of structures. Using an electron spectrometer that can simultaneously analyze and detect electrons over a range of emission directions[35-38] would also clearly speed up such studies, with the only likely drawback being that angular resolution is often lower in such systems, particularly when working at higher energies. In all of these methods, the final precise structural determination would require comparison of experimental diffraction curves or χ functions with calculated curves for a number of geometries, with the most quantitative method of comparison being via some sort of R factor.[20,26d] This is thus exactly the same methodology employed in LEED, except that in photoelectron diffraction, a single scattering approach should already provide useful information for many cases and there is additional readily available structural information concerning the type of local bonding site that can assist in ruling out structures.

As a final new direction in the analysis of scanned-angle data, we consider the recent interesting proposal by Barton,[151] based on an earlier suggestion by Szoeke,[152] that it should be possible to directly determine atomic positions via photoelectron holography. According to this idea, the photoelectron leaving the emitter is treated in first approximation as a spherical outgoing wave that, by virtue of the scattering and diffraction from its neighbors, produces an intensity modulation outside of the surface that can be considered a hologram. This hologram is then simply the intensity distribution of a given peak over a two-dimensional range in θ, ϕ (or, equivalently, some two-dimensional range in k_x, k_y). This intensity distribution can then be described by a formula of exactly the same type as Eq. (10), but with some important generalizations. These generalizations are that the scattering amplitude $|f_j|$ and phase shift ψ_j, together with the factors for the excitation matrix element and attenuation due to spherical wave, inelastic, and vibrational effects, must be replaced by an overall wave amplitude $|F_j|$ and phase ψ_j for each scatterer that sums over all single- and multiple-scattering events which terminate in atom j as the last scatterer before the detector. It can then be shown[151] that inverting this two-dimensional hologram mathematically to produce a real image is equivalent to a double Fourier integral in k_x and k_y, in which the desired z plane of the image is a variable parameter within the integral. Thus, two dimensional x–y cross sections at different z positions are in principle possible with this method.

Barton has carried out a theoretical simulation of this new method using MSC–SW intensity distributions in θ, ϕ for the $c(2 \times 2)$ S/Ni (001) system at a kinetic energy of 548 eV and with a width of angular detection in both the k_x and k_y directions of ±40°. The inversion of this hologram is found to have maxima that can be directly related to different near-neighbor Ni atoms, with an estimated resolution in x and y of 0.5 Å and in z of a much higher 2.3 Å. The x and y resolutions are ultimately limited by the Rayleigh criterion for a lens

(hologram) of a given opening angle. For the maximum reasonable detection-angle ranges in a spectrometer of ±40° to ±60°, this in turn yields resolution limits Δx and Δy that are very close to the de Broglie wavelength of the electron (i.e., 0.52 Å at 548 eV). This is a likely reason why a rather high kinetic energy in the typical XPS range was used for this simulation.

As noted by Barton, some limitations and/or problems that need to be addressed in the further development of this technique are the relatively low position-resolution obtainable, particularly in z; the presence of twin images at ±z for each atom (a universal effect in holography), which could cause serious overlap problems for bonding geometries involving atoms that are below-plane; the fact that multiple scattering effects on the F_j may cause deviations of the image positions from the actual sites, thus requiring an iterative correction via theoretical calculations of these generalized scattering amplitudes for an assumed geometry; the fact that several images at different energies, or even an additional Fourier transform of energy-dependent data at each θ, ϕ, may be necessary to effect this correction; and the added experimental difficulty in requiring some sort of high-speed multichannel electron analyzer that can obtain such large data sets in a reasonable amount of time.[35]

Another limitation not mentioned in connection with this theoretical simulation is that the high energy used implies relatively weak backscattering effects of only 15% or so compared to forward scattering (cf. Fig. 2); thus, the actual degree of modulation in intensity observed may be quite small, making the measurements rather difficult. Going to higher energies to improve resolution via shorter de Broglie wavelengths will make this problem worse due to even weaker backscattering. Thus, for an adsorbate or surface atom that has not significantly penetrated a surface, there will always be a tradeoff between resolution and ease of measurement in photoelectron holography. Of course, if the emitter is found below the surface, then strong forward scattering of the type discussed previously here can take place, and the resulting hologram should then show larger intensity modulations; however, forward scattering effects by themselves contain bond direction information, but not bond length information, so that the weaker modulations due to higher-order features would still need to be accurately measured in order for the inversion of the hologram to yield the full structure.

As a potentially more convenient experimental alternative for holography, a suitable Auger peak involving three filled levels might be useful as a source of a more nearly spherical wave as assumed in the image reconstruction, although the poorly understood mixing in of other l components could complicate a precise theoretical analysis of the effective amplitudes $|F_j|$ and phases ψ_j. Also, using Auger peaks that are too broad in energy would reduce the degree of monochromaticity (i.e., coherence) required in the source.[21b]

No matter how these problems are dealt with, even low-resolution three-dimensional images from such holography could be useful in ruling out certain bonding geometries in a semiquantitative way, much as Fourier transforms in ARPEFS can be useful through the approximate path-length differences they provide. It will be interesting to see what the first inversion of an experimental photoelectron hologram brings. (Please see the added note on holographic methods at the end of this chapter.)

6. COMPARISONS TO OTHER TECHNIQUES AND CONCLUDING REMARKS

We begin this concluding section by comparing photoelectron and Auger electron diffraction to several other current probes of surface structure in order to assess their relative strengths and weaknesses. As a first overall comment, it is clear from any perusal of the current literature (e.g., Ref. 1) that no one surface-structure probe directly and unambiguously provides all of the desired information on atomic identities, relative numbers, chemical states, positions, bond distances and bond directions in the first 3–5 layers of the surface. The very small number of surface structures for which there is a general consensus in spite of several decades of careful study of some of them testifies to the need for using complementary information from several methods.

To provide some idea of this complementarity of approaches, we show in Table 1 several techniques assessed according to a number of characteristics: photoelectron diffraction (PD) in both scanned-angle and scanned-energy forms, Auger electron diffraction (AED), surface extended X-ray absorption fine structure (SEXAFS),[16] near-edge X-ray absorption fine structure NEXAFS,[95,153,154] low-energy electron diffraction (LEED),[61] surface-sensitive grazing incidence X-ray scattering (GIXS),[27] scanning tunneling microscopy (STM),[155] and Rutherford backscattering (RBS) or medium-energy ion scattering (MEIS).[156] This is not intended to be a complete list of modern structure probes, but it roughly represents the group most used at present.

These techniques are rated, first, according to whether they directly provide information on atomic identity (a positive feature of all techniques except for LEED, GIXS, and STM) and chemical state (possible only with PD, AED, and NEXAFS). Atom identification is possible in GIXS only if use is made of anomalous dispersion near a certain absorption edge. State-specific information is not derivable in typical SEXAFS measurements because of the overlap of different oscillatory absorption structures above a given edge.

Also, we assess whether other subsidiary types of structural and bonding information can be obtained in a straightforward manner. Of course, once a structure has been determined and optimized to fit the data of any one of these methods, it has implicit in it bond directions, bond distances, site symmetries, and coordination numbers, but the table entries have been chosen to reflect the directness with which these can be extracted from the raw data with a minimum of data analysis. The types of information considered are valence electronic levels or excitations (directly accessible only in NEXAFS and STM), bond directions (particularly easy to determine in high-energy PD/AED with forward scattering—as discussed in comparison to other techniques in section 4.1.4—and in RBS/MEIS with shadowing and blocking), bond distances (very direct in SEXAFS, Fourier transforms), local bonding-site symmetries (easiest to determine with PD, Fourier transforms), and coordination numbers (derivable directly AED, SEXAFS, and RBS/MEIS), and coordination numbers (derivable directly from high-energy PD and AED and less directly from the amplitudes of SEXAFS oscillations). STM can also directly image surface atoms and thus provide coordination numbers, but it is limited to looking at only the outermost surface density of states, and so does not probe the bonding below this level in a direct

way. Distinguishing between structures that are related to atomic positions and protrusions in the density of states can also be a problem in STM. It has been suggested that NEXAFS resonance energies can be used to measure bond distances,[153] but this approach may be limited to well-calibrated series of homologous molecules, and has been called into question.[154]

The estimated accuracies of finally determining atomic positions with the current state of these techniques is also indicated. Numbers smaller or larger than these will be found for some cases in the literature, but it is the author's opinion that the numbers in the table are a better representation of the true absolute accuracies if all of the various uncertainties in both experimental parameters and the modelling or treatment of the data are taken into account. Surface X-ray diffraction is the most accurate, but its principal sensitivity is to horizontal positions, with vertical positions being derivable only via the more difficult method of measuring rod profiles normal to the surface. PD in any of its forms and AED should be inherently as accurate as SEXAFS, if not more so, particularly if the latter has been analyzed only with transform and back-transform methods without any final theoretical modeling. PD should also ultimately be as accurate as LEED,[73] particularly for a given amount of input to the theoretical analysis.

The degree to which these techniques probe short-range order in the first 10–20 Å around a given site versus longer-range order over 100 Å or more is also considered. Except for LEED and X-ray diffraction, all of the techniques are primarily sensitive to short-range order, although we have also pointed out that PD and AED actually have sensitivity extending over a region of diameter as large as 40 Å. Although inherently larger-scale probes, LEED and X-ray diffraction can with spot profile analysis be used to study the breakdown of long-range order in such phenomena as surface phase transitions.

Next, several characteristics relating to the ease of obtaining data and analyzing it theoretically are indicated: the overall percentage change in intensity as one measure of the ease of determining the signal (which is particularly large for PD, AED, and LEED); the possibility of using a simple, usually kinematical, theory to analyze the results; and the feasibility of using Fourier transform methods to more directly derive structural parameters. The overall figures for percentage effect should be assessed carefully, however, since the inelastic background under some photoelectron and Auger spectra can be high, thus making even a 50% modulation of the peak intensity difficult to measure. By contrast, for some applications of SEXAFS, background effects can be much reduced by using X-ray fluorescence detection,[157] although surface specificity is then lost. Problematic background effects can also arise in SEXAFS scans such as then lost. Problematic background effects can also arise in SEXAFS scans such as Auger-photoelectron interferences if either type of peak is being used to monitor the absorption and sharp spikes or glitches of intensity due to Bragg reflection of X-rays from very well-ordered crystals such as semiconductors. Auger-photoelectron interferences can also make the use of scanned-energy photoelectron diffraction more difficult if there are any Auger peaks from the sample that lie in the kinetic-energy range from about 100 eV to 400 eV. Standard Auger tabulations show that this could yield difficult background subtraction problems for the atomic number ranges 4–7, 14–22, and 37 upward. As examples of this, sulfur at 16 involves such an interference, as noted previously in sections 4.2.2 and 4.2.3,

TABLE 1. Comparison of Several Surface-Structure Techniques by Different Criteria ("yes" and "no" responses based on deriving a given type of information with minimal data analysis)

	Scanned-angle PD	Scanned-energy PD	AED	SEXAFS	NEXAFS	LEED	GIXS	STM	RBS/MEIS
Atom specific?	Yes	Yes	Yes	Yes	Yes	No	No^a	No	Yes
Chemical-state specific?	Yes^b	Yes^b	Yes^b?	No	Yes	No	No	No	No
Bond directions?	Yes^c	Yes^c	Yes^c	Yes^c	Yes^c	No	No	Yes^d	Yes^f
Bond distances?	Yes	Yes^c	Yes	Yes^c	No^g	No	No	Yes^d	Yes^f
Adsorption site symmetries?	Yes^c	Yes?	Yes^c	Yes^c?	No	No	No	Yes^d	Yes
Coordination numbers?	Yes^c	Yes	Yes^c	Yes	No	No	No	Yes^d	Yes
Position accuracies?	~0.02–0.05 Å	~0.02–0.05 Å	≤0.05 Å	~0.02–0.05 Å	?^{g}	~0.01–0.05 Å	~0.001 Å (Horizontal)^i ? (Vertical)	~0.3 Å (Horizontal) ~0.05 Å (Vertical)	~0.01 Å
Valence-electron states?	No	No	No	No	Yes	No	No	Yes	No
Short-range order (~10–20 Å)?	Yes	Yes	Yes	Yes	Yes	No	No	Yes^d	Yes
Long-range order (>100 Å)?	No	No	No	No	No	Yes	Yes	Yes^d	No
Overall %	20–70%	20–70%	20–70%	~5%	Variable	70–90% in I–V	Weaker surface peaks	Large	~10%^{f}
Kinematical theory?	Yes^j	Yes^j	Yes^j	Yes^j	No	No	Yes^j	No	Yes
Fourier transform analysis?	No^k	Yes^e	No	Yes^e	No	No	Yes	No	No
Requires synchrotron radiation?	No	Yes	No	Yes	Yes	No	Yes	Yes^l	No

^{a} GIXS only atom-specific if anomalous dispersion used.

^{b} If core shifts/line structure can be resolved in PD/AED, but more difficult in Auger spectra.

^{c} Forward scattering in high-energy PD and AED yields ~3 times better resolution for bond directions than in polarization-dependent NEXAFS and SEXAFS. Also directly gives coordination numbers for neighbors between emitter and detector.

^{d} STM senses only surface density of state contours, so that structural parameters are for outermost atoms only.

^{e} Fourier transforms to yield path-length differences in scanned-energy PD may be complicated by overlap of close-lying differences; SEXAFS Fourier transforms are simpler in this respect.

^{f} Via shadowing and blocking in RBS/MEIS.

^{g} Only via correlation of bond length with NEXAFS resonance energies that may be limited in application (see Refs. 153 and 154).

^{h} May be very direct than interatomic PD or AED data.

^{i} Vertical position information in GIXS less accurate and available only by measuring vertical rod profiles.

^{j} Some multiple scattering effects may have to be considered in all of PD, AED, and SEXAFS (see Refs. 57 and 85), and dynamical effects also may have to be included in the analysis of GIXS data in some scattering geometries (see Ref. 27).

^{k} Only if holographic imaging is possible.

^{l} Fourier transforms of STM images are useful for detecting lateral symmetries present.

and the Ag/Si system considered in section 4.4.2 was found in a recent scanned-energy experiment[50(c)]to exhibit extensive interferences over the full 90-350 eV range due to the various peaks in both the Si *KLL* and the Ag *MNN* spectra.

As a last and important criterion for the present volume, we indicate whether a given technique requires synchrotron radiation, as about half of them do.

The ideal structural probe would have "yes" for all of the nonquantitative characteristics in this table except the last one, which for reasons of broadest utility would be "no." It is clear that each method has positive features, but none constitutes this ideal probe. Thus, complementary information from several methods is in general desirable for fully resolving any structure. PD and AED are positive on sufficient points to be attractive additions to this list. AED is easier to excite (e.g., with photons or electrons), but the more complex nature of Auger spectra will prevent doing state-specific diffraction measurements for many cases, and an accurate theory, especially for lower energies, will be more difficult. Not being able to use radiation polarization to selectively excite towards a given scatterer is also a disadvantage of AED. As one disadvantage of scanned-angle PD and AED, we note the present lack of being able to use Fourier transform methods to determine structure directly (although photoelectron holography is a proposal to do this); thus it may be necessary to carry out a number of calculations for various structures, a procedure analogous to that used in LEED. However, some aspects of the data (e.g., forward scattering peaks at high energy) provide structural information very directly, and a good deal of any analysis should be possible within the framework of a simple single scattering picture. And in any case, the final test of any structural model derived in PD, AED, or SEXAFS should be to compare experiment to a diffraction calculation on a cluster of atoms of sufficient size to adequately include all significant scatterers.

Thus, although photoelectron diffraction and its close relative Auger electron diffraction are relatively new additions to the array of tools for studying surface structures, they have already proven to be useful for a broad variety of systems. Even at the present stage of development of both techniques with, for example, standard X-ray tubes or electron guns as excitation sources, and theory at the single-scattering-cluster–spherical-wave level, structurally useful and unique information can be derived for a range of problems including adsorption, molecular orientation, oxidation, epitaxial growth, metal–semiconductor interface formation, cluster growth, surface phase transitions, and short-range magnetic order. The use of higher angular resolutions promises to provide more precise structural information, particularly concerning longer-range order. The wider availability of synchrotron radiation, especially from the next generation of high-brightness insertion devices, will enormously increase the speed of both scanned-angle and scanned-energy measurements, thus permitting more studies of surface dynamics. The accurate-intensity ratio measurements at low kinetic energy required in spin-polarized photoelectron diffraction will also become easier. Some degree of lateral-resolution photoelectron microscopy-plus-diffraction should also become possible. And with focused electron beams, Auger electron microscopy-plus-diffraction is also feasible. Also, high-brightness radiation sources should permit increased energy resolutions of the order of 0.3 eV even at the higher photon

energies of 1.0–2.0 keV that are optimum for taking advantage of forward scattering and a single-scattering approach. Separate diffraction patterns will be obtainable for the various peaks in a given spectral region that are produced by chemical shifts, multiplet splittings, or more complex final-state effects. Using both linearly and circularly polarized radiation will also permit the selection of specific scatterers and spin-polarized final states, respectively. State-specific structural parameters should thus be derivable in a way that is not possible with other methods.

NOTE ON HOLOGRAPHIC METHODS

Since the original writing of this review, the use of holographically motivated Fourier-transform inversion methods for deriving surface structural information from both photoelectron- and Auger electron-diffraction data (cf. discussion in section 5.4) has advanced considerably. Some of these developments are discussed below.

The first experimental data have successfully been inverted to yield direct images of atomic positions near Cu surfaces by Tonner et al.[158] More recently, the same types of images have been observed for the semiconductors Si and Ge by Herman et al.[159] and for the simple adsorbate system c(2 × 2) S/Ni (001) by Saiki et al.[100] In general, these images are accurate to within about ±0.2–0.3 Å in planes parallel to the surface and more or less perpendicular to strong forward scattering directions, but only to within about ±0.5–1.0 Å in planes perpendicular to the surface or containing forward scattering directions.

Methods have been proposed for eliminating the observed distortions in atomic images due to both the anisotropic nature of the electron–atom scattering and the phase shift associated with the scattering by Saldin et al.,[160] Tong et al.,[161] and Thevuthasan et al.[162] Preliminary tests of these methods are encouraging, but more applications to experimental data are needed to assess them fully. Further image distortions due to anisotropies in the electron emission process have been discussed,[160,161] and corrections for these also appear to be useful. Additional spurious features that may arise in images due to the strength of the electron–atom scattering and resultant self-interference effects have been pointed out by Thevuthasan et al.[162] By contrast, the multiple scattering defocusing illustrated in Figs. 3b–ii and 6 has been shown to reduce the image distortions for the special case of buried emitters that are separated by several atoms from the detector.[162]

Finally, Barton[163] has shown in theoretical simulations that the simultaneous analysis of photoelectron holographic data obtained at several different photon energies, involving in effect an additional Fourier sum on energy, should act to reduce the influence of both twin images and multiple scattering on atomic images.

Thus, the holographic analysis of both photoelectron and Auger electron data is in an intense period of evaluation, with several indications already that it may ultimately provide reasonably good starting-point structures which can then be refined by the more classic trial-and-error methods discussed previously in this review, but in much reduced time.

ACKNOWLEDGMENTS

REFERENCES

1. Excellent summaries of the current status of most of these techniques can be found in the proceedings of three International Conferences on the Structure of Surfaces: (a) *The Structure of Surfaces* (M. A. Van Hove and S. Y. Tong, eds.), Springer Verlag, Berlin (1985); (b) *The Structure of Surfaces II* (J. F. van der Veen and M. A. van Hove, eds.), Springer-Verlag, Berlin (1988); (c) *The Structure of Surfaces III* (S. Y. Tong, M. A. Van Hove, K. Takayanagi, and X. D. Xie, eds.), Springer-Verlag, Berlin (1991).
2. K. Siegbahn, U. Gelius, H. Siegbahn, and E. Olsen, *Phys. Lett.* 32A, 221 (1970).
3. C. S. Fadley and S. A. L. Bergstrom, *Phys. Lett.* 35A, 375 (1971).
4. A. Liebsch, *Phys. Rev. Lett.* 32, 1203 (1974); *Phys. Rev.* B13, 544 (1976).
5. S. Kono, C. S. Fadley, N. F. T. Hall, and Z. Hussain, *Phys. Rev. Lett.* 41, 117 (1978); S. Kono, S. M. Goldberg, N. F. T. Hall, and C. S. Fadley, *Phys. Rev. Lett.* 41, 1831 (1978).
6. D. P. Woodruff, D. Norman, B. W. Holland, N. V. Smith, H. H. Farrell, and M. M. Traum, *Phys. Rev. Lett.* 41, 1130 (1978).
7. S. D. Kevan, D. H. Rosenblatt, D. Denley, B.-C. Lu, and D. A. Shirley, *Phys. Rev. Lett.* 41, 1565 (1978).
8. J. J. Barton, C. C. Bahr, Z. Hussain, S. W. Robey, J. G. Tobin, L. E. Klebanoff, and D. A. Shirley, *Phys. Rev. Lett.* 51, 272 (1983); J. J. Barton, C. C. Bahr, Z. Hussain, S. W. Robey, L. E. Klebanoff, and D. A. Shirley, *J. Vac. Sci. Technol.* A2, 847 (1984); J. J. Barton, S. W. Robey, C. C. Bahr, and D. A. Shirley in *The Structure of Surfaces* (M. A. van Hove and S. Y. Tong, eds.), Springer Verlag, Berlin (1985) p. 191.
9. C. S. Fadley, *Prog. in Surf. Sci.* 16, 275 (1984).
10. C. S. Fadley, *Phys. Scr.* T17, 39 (1987) and earlier references therein.
11. (a) W. F. Egelhoff, *Phys. Rev.* B30, 1052 (1984); (b) R. A. Armstrong and W. F. Egelhoff, *Surf. Sci.* 154, L225 (1985); (c) W. F. Egelhoff, *Phys. Rev. Lett.* 59, 559 (1987).
12. (a) S. A. Chambers, H. W. Chen, I. M. Vitomirov, S. B. Anderson, and J. H. Weaver, *Phys. Rev.* B33, 8810 (1986); (b) S. A. Chambers, I. M. Vitomirov, S. B. Anderson, H. W. Chen, T. J. Wagener, and J. H. Weaver, *Superlattices and Microstructures* 3, 563 (1987); (c) S. A. Chambers and T. J. Irwin, *Phys. Rev.* B38, 7858 (1988); and earlier references therein.
13. C. S. Fadley, in *Core-Level Spectroscopy in Condensed Systems* (J. Kanamori and A. Kotani, eds.), Springer Verlag, Berlin (1988), p. 236.
14. Z. Hussain, D. A. Shirley, C. H. Li, and S. Y. Tong, *Proc. Natl. Acad. Sci. USA.* 78, 5293 (1981). The use of Fourier transforms was here first thought to yield interlayer distances but later shown to provide path-length difference information, as discussed in Refs. 15 and 21.
15. P. J. Orders and C. S. Fadley, *Phys. Rev.* B27, 781 (1983).
16. (a) P. Citrin, in *Springer Series on Surface Science*, Vol. II, Springer Verlag, Berlin (1985), p. 49; (b) D. Norman, *J. Phys.* C19, 3273 (1986); (c) J. Stohr, in *X-Ray Absorption: Principles, Applications, Techniques of EXAFS, SEXAFS, and XANES* (R. Prins and D. Konigsberger, eds.), Wiley, New York (1987).
17. N. V. Smith, H. H. Farrell, M. M. Traum, D. P. Woodruff, D. Norman, M. S. Woolfson, and B. W. Holland, *Phys. Rev.* B21, 3119 (1980); H. H. Farrell, M. M. Traum, N. V. Smith, W. A. Royer, D. P. Woodruff, and P. D. Johnson, *Surf. Sci.* 102, 527 (1981).
18. (a) D. Sebilleau, M. C. Desjonqueres, D. Chauveau, C. Guillot, J. Lecante, G. Treglia, and D. Spanjaard, *Surf. Sci. Lett.* 185, L527 (1987); (b) M. C. Desjonqueres, D. Sebilleau, G. Treglia, D. Spanjaard, C. Guillot, D. Chauveau, and J. Lecante, *Scanning Electron Microsc.* 1 1557 (1987); (c) D. Sebilleau, G. Treglia, M. C. Desjonqueres, D. Spanjaard, C. Guillot, D. Chauveau, and J. Lecante, *J. Phys. (Paris)* 49, 227 (1988).
19. (a) B. Sinkovic, P. J. Orders, C. S. Fadley, R. Trehan, Z. Hussain, and J. Lecante, *Phys. Rev.* B30, 1833 (1984); (b) P. J. Orders, B. Sinkovic, C. S. Fadley, Z. Hussain, and J. Lecante, *Phys. Rev.* B30, 1838 (1984).
20. L. J. Terminello, X. S. Zhang, Z. Q. Huang, S. Kim, A. E. Schach von Wittenau, K. T. Leung, and D. A. Shirley, *Phys. Rev.* B38, 3879 (1988).
21. (a) M. Sagurton, E. L. Bullock, and C. S. Fadley, *Phys. Rev.* B30, 7332 (1984); and (b) *Surf. Sci.* 182, 287 (1987).
22. D. P. Woodruff, *Surf. Sci.* 166, 377 (1986).
23. L. G. Peterson, S. Kono, N. F. T. Hall, C. S. Fadley, and J. B. Pendry, *Phys. Rev. Lett.* 42, 1545 (1979).
24. H. C. Poon and S. Y. Tong, *Phys. Rev.* B30, 6211 (1984); S. Y. Tong, H. C. Poon, and D. R. Snider, *Phys. Rev.* B32, 2096 (1985).
25. J. J. Barton and D. A. Shirley, (a) *Phys. Rev.* B32, 1892 (1985) and (b) *Phys. Rev.* B32, 1906 (1985); (c) J. J. Barton, Ph.D. Thesis, U. Cal., Berkeley (1985); J. J. Barton, S. W. Robey, and D. A. Shirley, *Phys. Rev.* B34, 778 (1986).
26. (a) R. S. Saiki, A. P. Kaduwela, J. Osterwalder, M. Sagurton, C. S. Fadley, and C. R. Brundle, *J. Vac. Sci. Technol.* A5, 932 (1987); (b) R. S. Saiki, A. P. Kaduwela, J. Osterwalder, C. S. Fadley, and C. R. Brundle, *Phys. Rev.* B40, 1586 (1989); (c) R. S. Saiki, A. P. Kaduwela, J. Osterwalder, C. S. Fadley, and C. R. Brundle, to be published; (d) The R factors used in this study are generally the R1 defined in M. A. van Hove, S. Y. Tong, and M. H. Elconin, *Surf. Sci.* 64, 85 (1977), although final checks have also been made with the other possibilities R2–R5 discussed there.
27. Chapter 8 in this volume by P. H. Fuoss, K. S. Liang, and P. Eisenberger.
28. Chapter 3 of Vol. 2 of this set by J. Haase and A. M. Bradshaw.
29. H. Li and B. P. Tonner, *Phys. Rev.* B37, 3959 (1988).
30. S. A. Chambers, H. W. Chen, S. B. Anderson, and J. H. Weaver, *Phys. Rev.* B34, 3055 (1986).
31. S. D. Kevan, *Rev. Sci. Instrum.* 54, 1441 (1983).
32. S. D. Kevan, Ph.D. thesis, U. Cal., Berkeley (1980).
33. R. C. White, C. S. Fadley, and R. Trehan, *J. Electron Spectros. Relat. Phenom.* 41, 95 (1986).
34. J. Osterwalder, M. Sagurton, P. J. Orders, C. S. Fadley, B. D. Hermsmeier, and D. J. Friedman, *J. Electron. Spectros. Relat. Phenom.* 48, 55 (1989).
35. D. E. Eastman, J. J. Donelon, N. C. Hien, and F. J. Himpsel, *Nucl. Instrum Methods* 172, 327 (1980).
36. R. C. G. Leckey and J. D. Riley, *Appl. Surf. Sci.* 22/23, 196 (1985).
37. H. A. Engelhardt, W. Back, and D. Menzel, *Rev. Sci. Instrum.* 52, 835 (1981); H. A. Engelhardt, A. Zartner, and D. Menzel, *Rev. Sci. Instrum.* 52, 1161 (1981).
38. M. G. White, R. A. Rosenberg, G. Gabor, E. D. Poliakoff, G. Thornton, S. H. Southworth, and D. A. Shirley, *Rev. Sci. Instrum.* 50, 1268 (1979); Z. Hussain and D. A. Shirley, private communication.
39. R. C. G. Leckey, *J. Electron Spectros. Relat. Phenom.* 43, 183 (1987).
40. L. McDonnell, D. P. Woodruff, and B. W. Holland, *Surf. Sci.* 51, 249 (1975).
41. P. A. Lee, *Phys. Rev.* B13, 5261 (1976).
42. S. Kono, S. M. Goldberg, N. F. T. Hall, and C. S. Fadley, *Phys. Rev. Lett.* 41, 1831 (1978); *Phys. Rev.* B22, 6085 (1980).

43. T. Fujikawa, *J. Phys. Soc. Jpn.* **50**, 1321 (1981); **51**, 251 (1982); **54**, 2747 (1985); *J. Electron. Spectros. Relat. Phenom.* **26**, 79 (1982).

44. H. Daimon, H. Ito, S. Shin, and Y. Murata, *J. Phys. Soc. Jpn.* **54**, 3488 (1984).

45. J. J. Rehr, R. Albers, C. Natoli, and E. A. Stern, *Phys. Rev.* **B34**, 4350 (1986); J. J. Rehr, J. Mustre de Leon, C. R. Natoli, and C. S. Fadley, *J. Phys. (Paris)* **C8**, Suppl. 12, 213 (1986); J. J. Rehr, J. Mustre de Leon, C. R. Natoli, C. S. Fadley, and J. Osterwalder, *Phys. Rev.* **B39**, 5632 (1989).

46. D. E. Parry, *J. Electron. Spectros. Relat. Phenom.* **49**, 23 (1989).

47. D. J. Friedman and C. S. Fadley, *J. Electron Spectrosc.* **51**, 689 (1990).

48. (a) J. Osterwalder, E. A. Stewart, D. Cyr, C. S. Fadley, J. Mustre de Leon, and J. J. Rehr, *Phys. Rev.* **B35**, 9859 (1987); (b) J. Osterwalder, A. Stuck, D. J. Friedman, A. P. Kaduwela, C. S. Fadley, J. Mustre de Leon, and J. J. Rehr, *Phys. Scr.* **41**, 990 (1990); (c) J. Osterwalder, E. A. Stewart, D. J. Friedman, A. P. Kaduwela, C. S. Fadley, J. Mustre de Leon, and J. J. Rehr, unpublished results.

49. S. Kono, K. Higashiyama, and T. Sagawa, *Surf. Sci.* **165**, 21 (1986) and references to prior structure studies therein.

50. (a) E. L. Bullock, G. S. Herman, M. Yamada, D. J. Friedman, and C. S. Fadley, *Phys. Rev. B*, **41**, 1703 (1990); (b) E. L. Bullock, Ph.D. thesis, U. Hawaii (1988); (c) A. P. Kaduwela, D. J. Friedman, M. Yamada, E. L. Bullock, C. S. Fadley, Th. Lindner, D. Ricker, A. W. Robinson, and A. M. Bradshaw in *Structure of Surfaces III* (S. Y. Tong, M. A. Van Hove, K. Takayanagi, and X. D. Xie, eds.), Springer-Verlag, Berlin (1991), p. 600; and to be published.

51. M. Owari, M. Kudo, Y. Nibei, and H. Kamada, *J. Electron. Spectros. Relat. Phenom.* **21**, 131 (1981).

52. D. H. Rosenblatt, S. D. Kevan, J. G. Tobin, R. F. Davis, M. G. Mason, D. A. Shirley, J. C. Tang, and S. Y. Tong, *Phys. Rev.* **B26**, 3181 (1982).

53. G. Treglia, in *Core-Level Spectroscopy in Condensed Systems* (J. Kanamori and A. Kotani, eds.), Springer Verlag, Berlin (1988), p. 281.

54. J. J. Rehr and E. A. Albers, *Phys. Rev.* **B41**, 8139 (1990).

55. S. T. Manson, *Adv. Electron. Electron. Phys.* **41**, 73 (1976).

56. M. Sagurton, private communication.

57. P. A. Lee and J. B. Pendry, *Phys. Rev.* **B11**, 2795 (1975).

58. M. Sagurton, E. L. Bullock, R. Saiki, A. P. Kaduwela, C. R. Brundle, C. S. Fadley, and J. J. Rehr, *Phys. Rev.* **B33**, 2207 (1986).

59. H. C. Poon, D. Snider, and S. Y. Tong, *Phys. Rev.* **B33**, 2198 (1986).

60. M. Fink and A. C. Yates, *At. Data Nucl. Data Tables* **1**, 385 (1970); M. Fink and J. Ingram, *At. Data Nucl. Data Tables* **4**, 129 (1972); D. Gregory and M. Fink, *At. Data Nucl. Data Tables* **14**, 39 (1974).

61. J. B. Pendry, *Low Energy Electron Diffraction*, Academic Press, London (1974); M. A. van Hove and S. Y. Tong, *Surface Crystallography by LEED*, Springer-Verlag, New York (1979).

62. E. A. Stern, B. A. Bunker, and S. M. Heald, *Phys. Rev.* **B21**, 5521 (1980).

63. (a) R. Trehan and C. S. Fadley, *Phys. Rev.* **B34**, 6784 (1986); (b) R. Trehan, J. Osterwalder, and C. S. Fadley, *J. Electron. Spectros. Relat. Phenom.* **42**, 187 (1987).

64. M. P. Seah and W. A. Dench, *SIA, Surf. Interface Anal.* **1**, 2 (1979); C. J. Powell, *Scanning Electron Micros.* **4**, 1649 (1984); S. Tanuma, C. J. Powell, and D. R. Penn, *SIA Surf. Interface Anal.* **11**, 577 (1988).

65. P. M. Cadman and G. M. Gossedge, *J. Electron. Spectros. Relat. Phenom.* **18**, 161 (1980); C. M. Schneider, J. J. de Miguel, P. Bressler, J. Garbe, S. Ferrer, R. Miranda, and J. Kirscher, *J. Phys. (Paris)* C, Suppl. 12, 49, 1657 (1988).

66. O. A. Baschenko and V. I. Nefedov, *J. Electron. Spectros. Relat. Phenom.* **21**, 153 (1980) and **27**, 109 (1982) and earlier references therein.

67. Y. U. Idzerda, D. M. Lind, and G. A. Prinz, *J. Vac. Sci. Technol.* **A7**, 1341 (1989).

68. N. E. Erickson and C. J. Powell, *Phys. Rev.* **B40**, 7284 (1989).

69. P. J. Orders, S. Kono, C. S. Fadley, R. Trehan, and J. T. Lloyd, *Surf. Sci.* **119**, 371 (1981).

70. (a) H. Helferink, E. Lang, and K. Heinz, *Surf. Sci.* **93**, 398 (1980); (b) P. J. Orders, R. E. Connelly, N. F. T. Hall, and C. S. Fadley, *Phys. Rev.* **B24**, 6161 (1981).

71. E. L. Bullock and C. S. Fadley, *Phys. Rev.* **B31**, 1212 (1985).

72. R. O. Weissman and K. Muller, *Surf. Sci. Rep.* **1**, 251 (1981).

73. M. L. Xu and M. A. van Hove, *Surf. Sci.* **207**, 215 (1989).

74. G. Breit and H. Bethe, *Phys. Rev.* **94**, 888 (1954).

75. L.-Q. Wang, A. E. Schach von Wittenau, Z. G. Ji, L. S. Wang, Z. Q. Huang, and D. A. Shirley, *Phys. Rev.* **B44**, 1292 (1991); and unpublished results.

76. D. A. Wesner, F. P. Coenen, and H. P. Bonzel, *Surf. Sci.* **199**, L419 (1988).

77. S. Y. Tong and H. C. Poon, *Phys. Rev.* **B37**, 2884 (1988).

78. S. Tougaard, *SIA, Surf. Interface Anal.* **11**, 453 (1988) and earlier references therein.

79. (a) J. B. Pendry and B. S. Ing, *J. Phys.* **C8**, 1087 (1975); (b) B. K. Teo and P. Lee, *J. Am. Chem. Soc.* **1979**, 101 (1979).

80. (a) G. Treglia, M. C. Desjonqueres, D. Spanjaard, D. Sebilleau, C. Guillot, D. Chauveau, and J. Lecante, *J. Phys. (Paris)* **1**, 1879 (1989); (b) D. G. Frank, N. Batina, T. Golden, F. Lu, and A. T. Hubbard, *Science* **247**, 182 (1990) and references therein.

81. L. I. Schiff, *Quantum Mechanics*, 3rd ed., McGraw-Hill, New York (1968), p. 136.

82. J. J. Barton, M.-L. Xu, and M. A. van Hove, *Phys. Rev.* **B37**, 10475 (1988).

83. (a) M.-L. Xu, J. J. Barton, and M. A. van Hove, *J. Vac. Sci. Technol.* **A6**, 2093 (1988) and (b) *Phys. Rev.* **B39**, 8275 (1989).

84. A. P. Kaduwela, G. S. Herman, D. J. Friedman, C. S. Fadley, and J. J. Rehr, *Phys. Scr.* **41**, 948 (1990); A. P. Kaduwela, G. S. Herman, D. J. Friedman, and C. S. Fadley, *J. Electron. Spectrosc. Relat. Phenom.* **57**, 223 (1991).

85. (a) R. C. Albers and J. J. Rehr, to be published; (b) K. Baberschke, in *The Structure of Surfaces II* (J. F. van der Veen and M. A. van Hove, eds.), Springer-Verlag, Berlin (1988), p. 174; (c) P. Rennert and N. V. Hung, *Phys. Status Solid* **148**, 49 (1988).

86. R. S. Saiki, G. S. Herman, M. Yamada, J. Osterwalder, and C. S. Fadley, *Phys. Rev. Lett.* **63**, 283 (1989).

87. (a) D. W. Moon, S. L. Bernasek, D. J. Dwyer, and J. L. Gland, *J. Am. Chem. Soc.* **107**, 4363 (1985); (b) C. Benndorf, B. Kruger, and F. Thieme, *Surf. Sci.* **163**, L675 (1985); (c) D. W. Moon, S. Cameron, F. Zaera, W. Eberhardt, R. Carr, S. L. Bernasek, J. L. Gland, and D. J. Dwyer, *Surf. Sci.* **180**, L123 (1987).

88. (a) D. A. Wesner, F. P. Coenen, and H. P. Bonzel, *Phys. Rev. Lett.* **60**, 1045 (1988); (b) *Phys. Rev.* **B39**, 10770 (1989).

89. H. Kuhlenbeck, M. Neumann, and H.-J. Freund, *Surf. Sci.* **173**, 194 (1986).

90. K. C. Prince, E. Holub-Krappe, K. Horn, and D. P. Woodruff, *Phys. Rev.* **B32**, 4249 (1985); E. Holub-Krabbe, K. C. Prince, K. Horn, and D. P. Woodruff, *Surf. Sci.* **173**, 176 (1986).

91. D. R. Wesner, F. P. Coenen, and H. P. Bonzel, *Phys. Rev.* **B33**, 8837 (1986).

92. K. A. Thompson and C. S. Fadley, *Surf. Sci.* **146**, 281 (1984).

93. H. Ibach and D. L. Mills, *Electron Energy Loss Spectroscopy*, Academic Press, New York (1982).

94. T. E. Madey, David E. Ramaker, and R. Stockbauer, *Ann. Rev. Phys. Chem.* **35**, 215 (1984).

95. J. Stohr and R. Jaeger, *Phys. Rev.* **B26**, 4111 (1982); A. L. Johnson, E. L. Muetterties, J. Stohr, and F. Sette, *J. Phys. Chem.* **89**, 4071 (1985); J. Stohr and D. A. Outka, *Phys. Rev.* **B36**, 7891 (1987).

96. See discussion and references in I. P. Batra and J. A. Barker, *Phys. Rev.* **B29**, 5286 (1984) and R. L. Strong and J. L. Erskine, *Phys. Rev.* **B31**, 6305 (1985).

97. An excellent review of the O/Ni (001) system is by C. R. Brundle and J. Q. Broughton in *The Chemical Physics of Solid Surfaces and Heterogeneous Catalysis* (D. A. King and D. P. Woodruff, eds.), Elsevier, Amsterdam (1991), Vol. 3a.

98. J. E. Demuth, N. J. DiNardo, and C. S. Cargill, *Phys. Rev. Lett.* **50**, 1373 (1983).

99. J. J. Barton, C. C. Bahr, Z. Hussain, S. W. Robey, J. G. Tobin, L. E. Klebanoff, and D. A. Shirley, *Phys. Rev. Lett.* **51**, 272 (1983) and earlier references therein.

100. R. S. Saiki, A. P. Kaduwela, Y. J. Kim, D. J. Friedman, J. Osterwalder, S. Thevuthasan, E. Tober, R. Ynzunza and C. S. Fadley, to be published.

101. M. Sagurton, B. Sinkovic, and C. S. Fadley, unpublished results.

102. X. S. Zhang, L. J. Terminello, S. Kim, Z. Q. Huang, A. E. Schach von Wittenau, and D. A. Shirley, *J. Chem. Phys.* **89**, 6583 (1988).

103. W. F. Egelhoff, *Phys. Rev. Lett.* **59**, 559 (1987).

104. (a) S. A. Chambers, T. J. Wagener, and J. H. Weaver, *Phys. Rev.* B36, 8992 (1987); (b) D. A. Steigerwald and W. F. Egelhoff, *Phys. Rev. Lett.* 60, 2558 (1988).
105. G. Herman, J. Osterwalder, and C. S. Fadley, unpublished results.
106. J. J. Krebs, B. T. Jonker, and G. A. Prinz, *J. Appl. Phys.* 61, 2596 (1987).
107. G. S. Herman, T. Lindner, R. S. Saiki, and C. S. Fadley, unpublished results.
108. G. Granozzi, A. Rizzi, G. S. Herman, D. J. Friedman, C. S. Fadley, J. Osterwalder, and S. Bernardi, *Phys. Scr.*, 41, 913 (1990); G. S. Herman, D. J. Friedman, C. S. Fadley, G. Granozzi, G. A. Rizzi, J. Osterwalder, and S. Bernardi, *J. Vac. Sci. Technol.* B9, 1870 (1991).
109. R. E. Connelly, C. S. Fadley, and P. J. Orders, *J. Vac. Sci. Technol.* A2, 1333 (1984).
110. P. Alnot, J. Olivier, F. Wyczisk, and C. S. Fadley, *J. Electron. Spectros. Relat. Phenom.* 43, 263 (1987); P. Alnot, J. Olivier, and C. S. Fadley, *J. Electron. Spectros. Relat. Phenom.* 49, 159 (1989).
111. G. M. Rothberg, K. M. Choudhary, M. L. denBoer, G. P. Williams, M. H. Hecht, and I. Lindau, *Phys. Rev. Lett.* 53, 1183 (1984).
112. K. M. Choudhary, P. S. Mangat, A. E. Miller, D. Kilday, A. Filipponi, and G. Margaritondo, *Phys. Rev.* B38, 1566 (1988).
113. S. Kono in *Core-Level Spectroscopy in Condensed Systems* (J. Kanamori and A. Kotani, eds.), Springer-Verlag, Berlin (1988), p. 253.
114. T. Abukawa and S. Kono, *Phys. Rev.* B37, 9097 (1988).
115. (a) S. Ciraci and I. P. Batra, *Phys. Rev. Lett.* 56, 877 (1986); (b) E. M. Oellig and R. Miranda, *Surf. Sci.* 177, L947 (1986); (c) T. Kendelewicz, P. Soukassian, R. S. List, J. C. Woicik, P. Pianetta, I. Lindau, and W. E. Spicer, *Phys. Rev.* B37, 7115 (1988); (d) R. Ramirez, *Phys. Rev.* B40, 3962 (1989).
116. E. J. van Loenen, J. E. Demuth, R. M. Tromp, and R. J. Hamers, *Phys. Rev. Lett.* 58, 373 (1987); R. J. Wilson and S. Chiang, *Phys. Rev. Lett.* 59, 2329 (1987) and *J. Vac. Sci. Technol.* A6, 800 (1988); T. L. Porter, C. S. Chang, and I. S. T. Tsong, *Phys. Rev. Lett.* 60, 1739 (1988); and earlier references therein.
117. W. C. Fan, A. Ignatiev, H. Huang, and S. Y. Tong, *Phys. Rev. Lett.* 62, 1516 (1989).
118. S. Y. Tong, H. Huang, C. M. Wei, W. E. Packard, F. K. Men, G. Glander, and M. B. Webb, *J. Vac. Sci. Technol.* A6, 615 (1988).
119. E. L. Bullock and C. S. Fadley, unpublished results.
120. K. Tamura, U. Bardi, M. Owari, and Y. Nihei, in *The Structure of Surfaces II* (J. F. van der Veen and M. A. van Hove, eds.), Springer-Verlag, Berlin (1988), p. 404.
121. D. Spanjaard, C. Guillot, M. C. Desjonqueres, G. Treglia, and J. Lecante, *Surf. Sci. Rep.* 5, 1 (1985).
122. Y. Jugnet, N. S. Prakash, L. Porte, T. M. Duc, T. T. A. Nyugen, R. Cinti, H. C. Poon, and G. Grenet, *Phys. Rev.* B37, 8066 (1988).
123. (a) T. Miller, T. C. Hsieh, and T.-C. Chiang, *Phys. Rev.* B33, 6983 (1986); (b) J. Aarts, A.-J. Hoeven, and P. K. Larsen, *Phys. Rev.* B38, 3925 (1988); (c) F. J. Himpsel, F. R. McFeely, A. Taleb-Ibrahimi, J. A. Yarmoff, and G. Hollinger, *Phys. Rev.* B38, 6084 (1988).
124. E. Tosatti, in *The Structure of Surfaces II* (J. F. van der Veen and M. A. van Hove, eds.), Springer-Verlag, Berlin (1988), p. 535.
125. U. Breuer, O. Knauff, and H. P. Bonzel, *J. Vac. Sci. Tech.*, A8, 2489 (1990).
126. T. Tran, D. J. Friedman, Y. J. Kim, G. A. Rizzi, and C. S. Fadley, *Structure of Surfaces III* (S. Y. Tong, M. A. Van Hove, K. Takayanagi, and X. D. Xie, eds.) Springer-Verlag (1991), p. 522; T. Tran, S. Thevuthasan, Y. J. Kim, G. S. Herman, D. J. Friedman and C. S. Fadley, to be published.
127. (a) E. G. McRae and R. A. Malic, *Phys. Rev. Lett.* 58, 1437 (1987) and *Phys. Rev.* B38, 13183 (1988); (b) E. G. McRae, J. M. Landwehr, J. E. McRae, G. H. Gilmer, and M. H. Grabow, *Phys. Rev.* B38, 13178 (1988).
128. J. W. M. Frenken, J. P. Toennies, Ch. Woell, B. Pluis, A. W. Denier van der Gon, and J. F. van der Veen, in *The Structure of Surfaces II* (J. F. van der Veen and M. A. van Hove, eds.), Springer-Verlag, Berlin (1988), p. 547.
129. R. J. Baird, C. S. Fadley, and L. F. Wagner, *Phys. Rev.* B15, 666 (1977).
130. S. M. Goldberg, R. J. Baird, S. Kono, N. F. T. Hall, and C. S. Fadley, *J. Electron. Spectros. Relat. Phenom.* 21, 1 (1980).

131. W. Schaich, *Phys. Rev.* B8, 4078 (1973); E. A. Stern, *Phys. Rev.* B10, 3027 (1974).
132. See, for example, discussion of multiplets by C. S. Fadley in *Electron Spectroscopy: Theory, Techniques, and Applications* (C. R. Brundle and A. D. Baker, eds.), Vol. 2, Academic Press, London (1978), Ch. 1.
133. G. M. Rothberg, *J. Magn. Magn. Mater.* 15–18, 323 (1980).
134. (a) B. Sinkovic and C. S. Fadley, *Phys. Rev.* B31, 4665 (1985); (b) B. Sinkovic, Ph.D. thesis, U. Hawaii (1988); (c) B. Sinkovic, D. J. Friedman, and C. S. Fadley, *J. Magn. Magn. Mater.* 92, 301 (1991).
135. B. Hermsmeier, B. Sinkovic, J. Osterwalder, and C. S. Fadley, *J. Vac. Sci. Technol.* A5, 1082 (1987).
136. C. S. Fadley in (*Magnetic Properties of Low-Dimensional Systems II: New Developments* (L. R. Falicov, F. Meija-Lira, and J.-L. Moran-Lopez, eds.), Springer-Verlag, Berlin (1990), p. 36; See especially calculations by J. M. Sanchez and J.-L. Moran-Lopez for a frustrated antiferromagnetic system discussed therein.
137. B. W. Veal and A. P. Paulikas, *Phys. Rev. Lett.* 51, 1995 (1983).
138. B. Hermsmeier, C. S. Fadley, B. Sinkovic, M. O. Krause, J. Jiminez-Mier, P. Gerard, and S. T. Manson, *Phys. Rev. Lett.* 61, 2592 (1988).
139. S. P. Kowalczyk, L. Ley, R. A. Pollak, F. R. McFeely, and D. A. Shirley, *Phys. Rev.* B7, 4009 (1973).
140. P. S. Bagus, A. J. Freeman, and F. Sasaki, *Phys. Rev. Lett.* 30, 850 (1973).
141. E. Kisker and C. Carbone, *Solid State Commun.* 65, 1107 (1988).
142. B. Sinkovic, B. Hermsmeier, and C. S. Fadley, *Phys. Rev. Lett.* 55, 1227 (1985).
143. B. Hermsmeier, J. Osterwalder, D. J. Friedman, and C. S. Fadley, *Phys. Rev. Lett.* 62, 478 (1989); B. D. Hermsmeier, Ph.D. thesis, U. Hawaii (1989); B. Hermsmeier, J. Osterwalder, D. J. Friedman, B. Sinkovic, T. Tran, and C. S. Fadley, *Phys. Rev.* B42, 11895 (1990).
144. D. J. Friedman, B. Sinkovic, C. S. Fadley, *Phys. Scr.* 41, 909 (1990).
145. J. E. Smart, *Effective Field Theories of Magnetism*, Saunders, New York (1966), Ch. 4.
146. M. Landolt and D. Mauri, *Phys. Rev. Lett.* 49, 1783 (1982); D. Mauri, R. Allenspach, and M. Landolt, *Phys. Rev. Lett.* 52, 152 (1984); M. Taborelli, R. Allenspach, and M. Landolt, *Phys. Rev.* B34, 6112 (1996); R. Allenspach, D. Mauri, M. Taborelli, and M. Landolt, *Phys. Rev.* B35, 4801 (1987).
147. G. Schuetz, W. Wagner, W. Wilhelm, P. Keinle, R. Zeller, R. Frahm, and G. Materlik, *Phys. Rev. Lett.* 58, 737 (1987); G. Schuetz, R. Frahm, P. Mautner, R. Wienke, W. Wagner, W. Wilhelm, and P. Kienle, *Phys. Rev. Lett.* 62, 2620 (1989); G. Schuetz, *Phys. Scr.* T29, 172 (1989); G. Schuetz and R. Wienke, *Hyperfine Interactions* 50, 457 (1989).
148. G. Schoenhense, *Appl. Phys.* A41, 39 (1986); C. Westphal, J. Bansmann, M. Getzlaff, and G. Schoenhense, *Phys. Rev. Lett.* 63, 151 (1989); G. Schoenhense, *Phys. Scr.*, T31, 255 (1990).
149. K. A. Thompson and C. S. Fadley, *J. Electron, Spectros. Relat. Phenom.* 33, 29 (1984).
150. P. L. King, A. Borg, P. Pianetta, I. Lindau, G. Knapp, and M. Keenlyside, *Phys. Scr.* 41, 413 (1990); B. P. Tonner, *Phys. Scr.* T31, (1990); W. Ng, A. K. Ray-Chaudhuri, R. K. Cole, S. Crossley, D. Crossley, C. Gong, M. Green, J. Guo, R. W. C. Hansen, F. Cerrina, G. Margaritondo, J. H. Underwood, J. Kortright, and R. C. C. Perera, *Phys. Scr.* 41, (1990); H. Ade, J. Kirz, S. L. Hulbert, E. D. Johnson, E. Anderson, and D. Kern, *Appl. Phys. Lett.* 56, 1841 (1990).
151. J. J. Barton, *Phys. Rev. Lett.* 61, 1356 (1988) and private communication.
152. A. Szoeke, in *Short Wavelength Coherent Radiation: Generation and Applications* (D. T. Attwood and J. Bokor, eds.), AIP Conf. Proc. No. 147, American Institute of Physics, New York (1986).
153. J. Stohr, J. L. Gland, W. Eberhardt, D. A. Outka, R. J. Madix, F. Sette, R. J. Koestner, and U. Doebler, *Phys. Rev. Lett.* 51, 2414 (1983); J. Stohr, F. Sette, and A. L. Johnson, *Phys. Rev. Lett.* 53, 1684 (1984); A. P. Hitchcock and J. Stohr, *J. Chem. Phys.* 87, 3253 (1986).
154. M. N. Piancastelli, D. W. Lindle, T. A. Ferrett, and D. A. Shirley, *J. Chem. Phys.* 86, 2765 (1987) and 87, 3255 (1987).
155. P. K. Hansma and J. Tersoff, *J. Appl. Phys.* 61, R1 (1987); J. Tersoff, in *The Structure of Surfaces II* (J. F. van der Veen and M. A. van Hove, eds.) Springer-Verlag, Berlin (1988), p. 4; and references therein.

156. T. Gustafsson, M. Copel, and P. Fenter, in *The Structure of Surfaces II* (J. F. van der Veen and M. A. van Hove, eds.) Springer-Verlag, Berlin (1988), p. 110; and references therein.

157. F. Sette, S. J. Pearton, J. M. Poate, J. E. Rowe, and J. Stohr, *Phys. Rev. Lett.* **56**, 2637 (1986).

158. G. R. Harp, D. K. Saldin, and B. P. Tonner, *Phys. Rev. Lett.* **65**, 1012 (1990), and *Phys. Rev.* **B42**, 9199 (1990).

159. G. S. Herman, S. Thevuthasan, T. T. Tran, Y. J. Kim, and C. S. Fadley, *Phys. Rev. Lett.* 3 Feb., 1991.

160. D. K. Saldin, G. R. Harp, B. L. Chen, and B. P. Tonner, *Phys. Rev.* **B44**, 2480 (1991) and earlier references therein.

161. S. Y. Tong, C. M. Wei, T. C. Zhao, H. Huang, and H. Li, *Phys. Rev. Lett.* **66**, 60 (1991); S. Y. Tong, H. Li, and H. Huang, *Phys. Rev. Lett.* **67**, 3102 (1991).

162. S. Thevuthasan, G. S. Herman, A. P. Kaduwela, R. S. Saiki, Y. J. Kim, W. Niemczura, M. Burger, and C. S. Fadley, *Phys. Rev. Lett.* **67**, 469 (1991).

163. J. J. Barton, *Phys. Rev. Lett.* **67**, 3406 (1991).